AI–7979

SECOND ANNUAL TECHNICAL SUMMARY REPORT FOR BASIC RESEARCH IN THERMIONIC ENERGY CONVERSION

(1 November 1961 to 31 October 1962)

Contract NONR–3192(00)

By

C. WARNER, III, L. K. HANSEN, H. HORI, R. L. McKISSON

Prepared for

Office of Naval Research
Power Branch
Department of the Navy
Washington 25, D. C.

Approved by Robert C Allen
R. C. Allen
Director,
Thermionics and Thermoelectrics

Atomics International Division of North American Aviation, Inc., 8900 DeSoto Avenue, Canoga Park, California

DISCLAIMER

This report was prepared as an account of work sponsored by an agency of the United States Government. Neither the United States Government nor any agency Thereof, nor any of their employees, makes any warranty, express or implied, or assumes any legal liability or responsibility for the accuracy, completeness, or usefulness of any information, apparatus, product, or process disclosed, or represents that its use would not infringe privately owned rights. Reference herein to any specific commercial product, process, or service by trade name, trademark, manufacturer, or otherwise does not necessarily constitute or imply its endorsement, recommendation, or favoring by the United States Government or any agency thereof. The views and opinions of authors expressed herein do not necessarily state or reflect those of the United States Government or any agency thereof.

DISCLAIMER

Portions of this document may be illegible in electronic image products. Images are produced from the best available original document.

ACKNOWLEDGMENT

This report has been prepared under Contract Nonr-3192(00), Office of Naval Research. The work performed under this contract has been under the technical supervision of Cmdr. J.J. Connelly, Jr.; his encouragement, interest and guidance are gratefully acknowledged.

The authors wish to acknowledge the assistance of several other individuals: K.W. Medeiros performed many of the calculations of Sections IV and V. H.G. Barrus constructed the diode used for Section VI. In addition, helpful discussions with C.C. Weeks and M.N. Huberman are gratefully acknowledged.

ABSTRACT

This report presents the results of the past year's work in a continuing program to investigate basic processes in thermionic energy conversion important to a thermionic nuclear power plant for naval applications. The previous work was reported in AI-6799, "First Summary Report of Basic Research in Thermionic Conversion Processes." The subjects discussed in the present report are:

Statistical Mechanics of Cesium Adsorption

Space Charge Analysis for Low Pressure Thermionic Diodes

Emission Requirements for Removal of Space Charge Barriers

Unignited Mode of Thermionic Converters

Interpretation of Volt-Ampere Characteristics

Vaporization and Deposition at Cesium Covered Surfaces

Cesium Purification

TABLE OF CONTENTS

Section		Page
	Abstract	iii
I	Introduction	1
II	Summary of Results	3
III	Statistical Mechanics of Cesium Adsorption (Warner)	8
	Introduction	8
	Development of General Expressions for Departure Rates	8
	Bragg-Williams Approximation	16
	Calculation of $\Delta\phi(\theta,T)$	19
	Summary	25
	References	27
IV	Space Charge Analysis for Low Pressure Thermionic Diodes (Warner)	28
	Introduction	28
	The Basic Equations	28
	Solutions for Infinite Spacing	33
	Solutions for Finite Spacing	39
	References	43
V	Emission Requirements for Removal of Space Charge Barriers (Hansen and Warner)	44
	Introduction	44
	Vacuum Diode	44
	Generalization to Include Ion Emission	47
	References	57

Section		Page
VI	Unignited Mode of Thermionic Converters (Hansen and Hori)	58
	Introduction	58
	Apparatus	58
	Volt-Ampere Characteristics	61
	Visual Appearances	75
	Interpretation	75
	Reference	75
VII	Interpretation of Volt-Ampere Characteristics (Warner and Hansen)	76
	Introduction	76
	Review of Related Phenomena in Gaseous Discharges	77
	Interpretation of the Unignited Mode	80
	Ignited Mode	107
	References	108
VIII	Vaporization and Deposition at Cesium Covered Surfaces (Hansen)	110
	Introduction	110
	Kinetics of Vaporization and Deposition	111
	Experiment	114
	Conclusion	118
	References	119
IX	Cesium Purification (McKisson)	121
	Introduction	121
	Cesium Analysis	121
	Nomenclature	125

LIST OF TABLES

		Page
Section III		
I	Adion Coverage θ_i Vs. Total Coverage θ for Zero Adatom Polarizability	20
II	Adion Coverage θ_i Vs. Total Coverage θ for Equal Adatom and Adion Polarizabilities	24
Section VII		
I	Diode Parameters for $\beta = \frac{1}{100}$, $\frac{3L}{4\lambda_e} = 100$, $\lambda_e/\lambda_p = 2$	102
Section IX		
I	Typical Cesium Metal Analyses	123
II	Atomics International Cesium Analyses	124

LIST OF ILLUSTRATIONS

		Page
Section III		
1	Cesium-[Metal]Systems at Constant T and P	9
2	Energy Curves for Cesium Atoms and Ions	11
3	Breakup of Energy of Ionic Adsorption Corresponding to Three Steps, S_1, S_2, S_3	11
4	Potential Distribution for Finite Assembly of N'_{si} Dipoles	11
Section IV		
1	Separation of η_m, η_{min} Space into Regions According to the Shape of the Potential Distribution	29

		Page
2	Some Typical Potential Distributions for Infinite Spacing	30
3	Oscillatory Potential Distribution Exhibiting Potential Maxima, η_m and η_{max}, and Potential Minimum η_{min}	32
4	Sequence of Potential Distributions for $0.786<\beta<1.000$	38
5	Non-oscillatory Potential Distributions for Finite Spacing	40
6	Some Potential Distributions for $\beta=0.1$	41
7	Volt-Ampere Curves Showing Bi-stability	41
Section V		
1	Regions of Vacuum Diode Operation	46
2	Definition of Symbols	46
3	Magnitude of Space Charge Barriers	38
4	Plot of ξ/x Vs. Electron Current $\dot{i}$ for Various Temperatures	48
5	β Emission Requirements for Removal of Space Charge Barriers	50,51
6	Potential Distributions with Zero Collector of Zero Emitter Field	53
7	Asymptotic β Values	53
8	Magnitude of Space Charge Barriers	55
Section VI		
1	Variable-Spacing Converter	59
2	Exploded View of Variable-Spacing Converter	60
3	Circuit for Obtaining Converter Volt-Ampere Characteristics	60
4	Unignited Mode for Spacing L=5 mils	62,63
5	Unignited Mode for Spacing L=10 mils	64,65

		Page
6	Unignited Mode for Spacing L=15 mils	66,67
7	Unignited Mode for Spacing L=25 mils	68,69
8	Unignited Mode for Spacing L=50 mils	70,71
9	Unignited Mode for Spacing L=92 mils	72,73
10	A Typical Volt-Ampere Characteristic	74
Section VII		
1	Volt-Ampere Characteristics for a "Cold" Electrode Discharge	78
2	Work Function, Emitted Current, and Debye Length for Cesium-Covered Molybdenum	82
3	Emission Ratio for Cesium-Covered Molybdenum and Mean Free Path for Electrons in Cesium	83
4	Volt-Ampere Characteristics for Position 7H of Figure 2	85
5	Comparison of Converter Volt-Ampere Characteristics for Position 7G in Figure 2 with Some Vacuum Diode Characteristics for the Same Emitter Temperature and Saturation Current	87
6	Potential Distribution for Ion-Rich Emission and an Accelerating Collector Sheath	90
7	Diode Current, Γ_e/ν_e, Vs. the Parameter $\gamma(1+R)^2$	92
8	Current Ratio Coefficient, R, Vs. the Collector Sheath Potential for Ion-Rich Emission	92
9	Random Current, Γ_r, at the Emitter Sheath Edge Vs. the Current Ratio Coefficient, R	93
10	Potential Drop in the Plasma Vs. the Current Ratio Coefficient, R	93

		Page
11	Potential Distribution for Ion-Rich Emission and a Retarding Collector Sheath	94
12	Volt-Ampere Characteristic for Ion-Rich Emission According to Plasma Model	98
13	Potential Distribution for Ion-Rich Emission at a Patchy Emitter	99
14	Volt-Ampere Characteristic for Electron-Rich Emission According to Plasma Model	102
15	Volt-Ampere Characteristics for Position 1F of Figure 2	104
16	Saturation Current, I_{sat}, Vs. the Reciprocal Spacing, L^{-1}	104
Section VIII		
1	Kossel's Idealized Model of a Low-Index Plane	111
2	Vacuum Chamber Cover Assembly	116

I. INTRODUCTION

This research program is directed toward development of an understanding of the fundamental processes occurring in thermionic converters and correlation of these processes to develop an understanding of overall converter performance.

The previous phases of the program were mostly concerned with emission processes; these results were reported in AI-6799, "First Summary Report of Basic Research in Thermionic Conversion Processes," issued in November 1961. In that report the ideal converter performance was determined and the details of the fundamental emission processes were analyzed and related to the requirements for ideal converter operation. This thereby provided an extensive analysis of emission-limited converter operation.

The continuation of the program, the results of which are included in the present report, extends some of the theories of the emission processes, but emphasizes the processes occurring in the interelectrode space and the relation and importance of the emission characteristics on the transport effects. The work of this year, therefore, represents a logical extension of the earlier work in that the knowledge of the emission processes is coupled with studies of the transport processes in order to effect a more complete understanding of thermionic energy conversion. The results are summarized in the following section. The remainder of the report consists of detailed articles on problems investigated during the past year.

Predominantly, the conventions used in this report are those proposed for the 1962 Colorado Springs Symposium on Thermionic Power Conversion. When the discussion is directly related to gaseous discharges or vacuum electronics, however, and when extensive reference is made to published

works in those fields, the terminology and conventions of those fields are retained to enable the reader to relate conveniently the present and previous work. For example, in Sections IV and V the power quadrant is plotted to the left while in Sections VI and VII it is plotted to the right. Also, the terms cathode and anode are used instead of emitter and collector when discussing previous literature which use the former terms. The terms emitter and collector are used whenever thermionic converters are discussed. When subscripts to symbols are to indicate an electrode, upper case letters are used; when subscripts or superscripts are to indicate a particle species, lower case letters are used.

II. SUMMARY OF RESULTS

Some of the work of the past year has been a continuation of the study of emission phenomena and the emission-limited thermionic converter. The results of this study are discussed in Section III. Results of the studies of the transport processes and the interaction of emission and transport effects are discussed in Sections IV, V, VI and VII. Two other experiments were performed during this year. One of the experiments involved vaporization and deposition at cesium-covered surfaces; the other concerned chemical analyses of commercially available cesium. The results of these two experiments are reported in Sections VIII and IX. Summaries of these Sections are as follows:

STATISTICAL MECHANICS OF CESIUM ADSORPTION

A statistical mechanical formalism is developed for the adsorption of cesium on metals. The adsorbed cesium is assumed to exist in both ionic and atomic states. This formalism describes more accurately the approach used in the first ONR report, AI-6799. The earlier treatment assumed that adsorption took place only as ions. The present treatment yields general expressions for the atom, ion and electron evaporation rates (ν_a, ν_i and ν_e) with both adions and adatoms present. Previously, ν_e, but not ν_a or ν_i, was derived under the same assumptions; only adions were assumed and the derivation of ν_a and ν_i lay partly outside the statistical mechanical formalism.

The inclusion of the effects of adatoms has shown that a major effect in explaining the maximum in the work function change may be due to the polarizability of the adatoms. Furthermore, at large coverages where this theory is inadequate, the lateral bonding of the cesium and possible accom-

panying effects such as changes in polarizability may also be extremely important.

SPACE CHARGE ANALYSIS FOR LOW PRESSURE THERMIONIC DIODES

A space charge analysis of a collisionless, plane electrode thermionic converter has been performed. With both ions and electrons emitted, the potential distributions can assume a variety of forms. This report completely systematizes these solutions. The space charge problem is first considered for infinite spacing, and the potential distributions are characterized by the collector potential and the potential at which the electric field first vanishes. For a given emitted ion-to-electron ratio, the diode ion and electron currents are easily extracted as a function of collector potential, and thus the volt-ampere curve can be plotted. The resulting volt-ampere characteristics extend continuously from minus infinity to plus infinity, so that the load line always yields an operating point. The present analysis concludes with a discussion of the solutions for finite spacing. They are compared with the infinite spacing solutions and numerical results are given. An example of bi-stability is shown, and the origin of oscillations briefly considered.

EMISSION REQUIREMENTS FOR REMOVAL OF SPACE CHARGE BARRIERS

Potential distributions in low-pressure converters have been analyzed theoretically to determine under what conditions they will be operating in retarding-field, space-charge-limited or saturated-emission modes. The necessary calculations have been made so that the particular mode can be determined from a graph when the voltage, emitter temperature, spacing and emission β of the converter are given. The same data allow one to determine the β required for saturated diode current for given diode voltage, emitter temperature and spacing. One simple result of the calculations is that for

$\beta > 1.27$ a space charge limitation cannot exist in a diode for any current, spacing or voltage. Another result is that for small applied voltages ($eV > 2kt$) an emission $\beta \approx 0.5$ insures that no space charge limitations will occur for any value of electron emission current.

UNIGNITED MODE OF THERMIONIC CONVERTERS

The volt-ampere characteristics of thermionic converters in the unignited mode are sensitive to changes in emitter temperature, cesium pressure and spacing. The dependence of the characteristics on these parameters has been measured so that some of the basic processes occurring in converters could be studied under conditions not complicated by the additional mechanisms in the ignited mode. Several features were observed electrically and visually which related to previous work with externally heated hot cathode discharges. Examples are the "anode glow" and "ball of fire" modes studied by Malter, Johnson and Webster. The first ignited mode studied by Daly and Emelens, and Pengelly and Wright was also observed in thermionic converters. Patch effects were also noted as evidenced by variations in the glow in the interelectrode spacing and in the dependence of the low pressure characteristics on voltage and spacing. This work provides the experimental basis for the theoretical analyses of Section V.

INTERPRETATION OF VOLT-AMPERE CHARACTERISTICS

The set of volt-ampere curves in Section VI have been interpreted in terms of surface ionization modes, sheath ionization modes and volume ionization modes. The emphasis in the present paper has been on the first two modes. In the unignited, surface ionization mode two limiting modes are studied, a space charge mode and a plasma mode. The space charge mode is treated by space charge theory and the plasma mode by transport theory. The space charge mode occurs predominantly for spacing which is small com-

pared to the mean free path and vice-versa for the plasma mode. The close spacing volt-ampere curves were interpreted by the space charge analysis developed by Langmuir. A patch effect appears to be indicated. A transport theory is developed for the plasma mode and the importance of diffusion as a current-limiting mechanism is experimentally observed in the dependence of the saturation current on spacing. This observation means that theories of the unignited mode which assume a uniform plasma and thus no density gradient are incorrect. The development of a collector sheath sufficiently large to provide sheath ionization is observed in the departure from the apparent saturation current to increased currents as more ions are provided. A theory with sheath ionization is outlined but not carried out. One very important feature of the sheath ionization mode is its initiation at sheath voltages appreciably less than the cesium ionization potential. Further confirmation of the correctness of this conclusion would indicate a two-stage process as has been suggested for the ignited mode.

VAPORIZATION AND DEPOSITION AT CESIUM COVERED SURFACES

The effect of adsorbed impurities (particularly cesium) on vaporization rates and condensation coefficients has been discussed. At cesium coverages, cesium pressures, and electrode temperatures of interest in thermionic energy conversion, it was found that vaporized emitter material has only a 0.0005 to 0.0013 probability for sticking to the collector. No effect with cesium coverages was observed and close correspondence was found for a case where no back scatter occurred to a case where normal converter back scatter occurred. It was concluded, therefore, that the low condensation coefficient is the dominating factor determining material transport in converters.

CESIUM PURIFICATION

Since it has been shown experimentally that impurities or additives to cesium vapor have a profound effect on converter performance, a program was initiated to examine the purity of the commercially available cesium. At the beginning of the program considerable uncertainty existed regarding both the purity of the metal and the accuracy of the chemical analyses of the metal. Analytical techniques were established for examining cesium samples from several suppliers. It was found that the quality of commercially available cesium has continually improved and that in most cases the accompanying analyses are adequate.

III. STATISTICAL MECHANICS OF CESIUM ADSORPTION

C. Warner, III

INTRODUCTION

A statistical mechanical formalism is developed in this study for the adsorption of cesium on metals. The adsorbed cesium is assumed to exist in both ionic and atomic states. This formalism describes more accurately the approach used in the earlier paper "Correlation of Electron, Ion and Atom Emission Energies."[1] Another paper in that report "Statistical Mechanical Treatment of Surface Ionization"[2] assumed that adsorption took place only as ions. The present treatment yields general expressions for the atom, ion and electron evaporation rates (ν_a, ν_i and ν_e) with both adions and adatoms present. Previously,[1] ν_e was derived but not ν_a or ν_i under the same assumptions. In Reference 2, only adions were assumed and the derivation of ν_a and ν_i lay partly outside the statistical mechanical formalism. In Reference 3, an approximation to the energy of ionic evaporation was made with adions only. The approximation considered the adions always to be in their final configuration as the test adion was being adsorbed.

The results of this study are compared with those of Taylor and Langmuir,[4] and the previous ONR work.[1,2,3] Finally, inadequacies in the analysis are discussed. In particular, the difficulties of calculation at high coverages are discussed. A high coverage calculation which includes depolarization of adatoms is shown to alter appreciably the work function predictions.

DEVELOPMENT OF GENERAL EXPRESSIONS FOR DEPARTURE RATES

Consider the closed system at constant temperature T and pressure P shown in Figure 1, and let there be N_a cesium atoms, N_i cesium ions and N_e

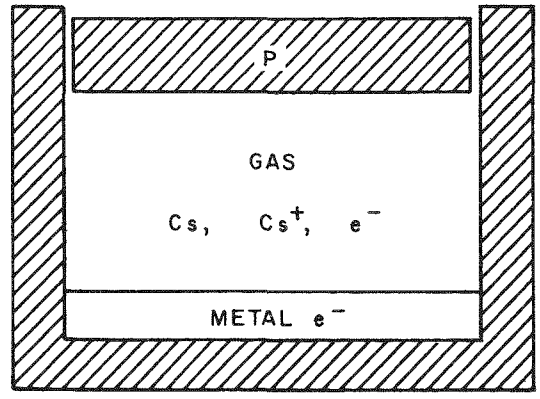

Figure 1. Cesium-[Metal] Systems at Constant T and P

electrons in the gas phase in equilibrium with N_{em} electrons in the metal and N_{sa} cesium atoms and N_{si} cesium ions on its surface. For phase equilibrium, thermodynamic laws require that the corresponding chemical potentials must satisfy these equations:

$$\mu_{em} = \mu_e, \ \mu_a = \mu_{sa}, \ \mu_i = \mu_{si}, \qquad \ldots (1,2,3)$$

and for chemical equilibrium, the following equation

$$\mu_a = \mu_i + \mu_e \ . \qquad \ldots (4)$$

The usual expressions for μ_e, μ_{em}, μ_i and μ_a are

$$\mu_e = kT \ln \frac{N_e}{2V} \left(\frac{2\pi\hbar^2}{mkT} \right)^{3/2} \qquad \ldots (5)$$

$$\mu_{em} = -e \ \phi \left[N_{si} \right] \qquad \ldots (6)$$

$$\mu_i = kT \ln \frac{N_i}{V} \left(\frac{2\pi\hbar^2}{MkT} \right)^{3/2} \qquad \ldots (7)$$

$$\mu_a = kT \ln \frac{N_a}{2V} \left(\frac{2\pi\hbar^2}{MkT} \right)^{3/2} -eI \qquad \ldots (8)$$

for volume V, ionization potential I, electron mass m, cesium mass M, Planck constant $h = 2\pi\hbar$, and Boltzmann constant k. The work function ϕ in Equation 6 is assumed to depend only on the ionic coverage, $N_{si}/\mathcal{S}$ and is given by electrostatic theory,

$$\phi = \phi_o - \Delta\phi = \phi_o - 2\pi \frac{N_{si}}{\mathcal{S}} M \qquad \ldots (9)$$

where M is the electric dipole moment of the adion and its image and $\mathcal{S}$ is the surface area.

Equations 1, 5 and 6 imply

$$\frac{N_e}{V}\sqrt{\frac{kT}{2\pi m}} = \frac{4\pi m k^2}{h^3} T^2 \exp\left(-\phi/kT \right) \qquad \ldots (10)$$

which is just Richardson's equation if the electron departure rate is equated to the electron arrival (which is the left hand side of Equation 10 by kinetic theory).

Equations 4, 5, 7 and 8 imply the Saha equation

$$\frac{N_a}{N_i} = \frac{N_e}{V}\left(\frac{2\pi}{mkT}\right)^{3/2} \hbar^3 \exp\left(e\, I/kT\right) \qquad \ldots (11)$$

The atom and ion departure rates, ν_a and ν_i, follow from Equations 2 and 3 just as the Richardson equation follows from (1). It is necessary in obtaining the Richardson equation from (10) and the departure rates ν_a and ν_i derived below in Equations 24 and 25, that the incident particles are not reflected but all adsorbed; otherwise the departure rate must be equated to that fraction of the incident particles which are adsorbed. This assumption implies that the adsorption process does not have any activation energy.

The chemical potentials μ_{sa} and μ_{si} are not given in the literature and must be calculated by statistical mechanics:

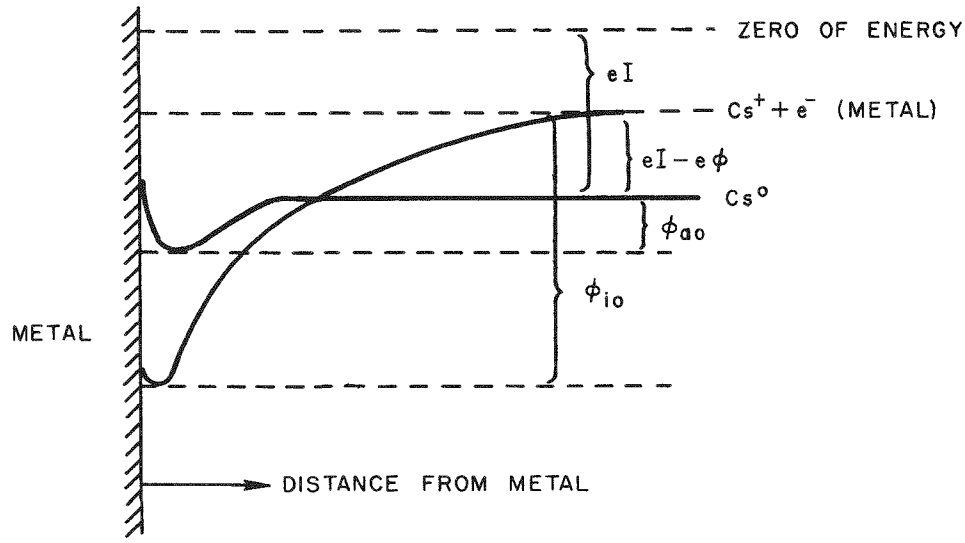

Figure 2. Energy Curves for Cesium Atoms and Ions[8]

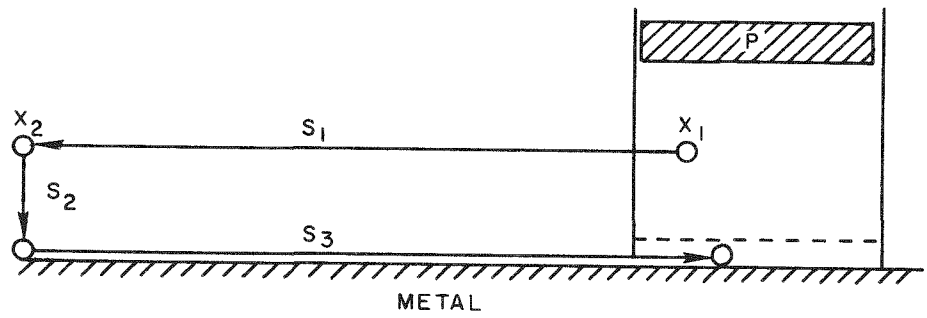

Figure 3. Breakup of Energy of Ionic Adsorption Corresponding to Three Steps, S_1, S_2, S_3

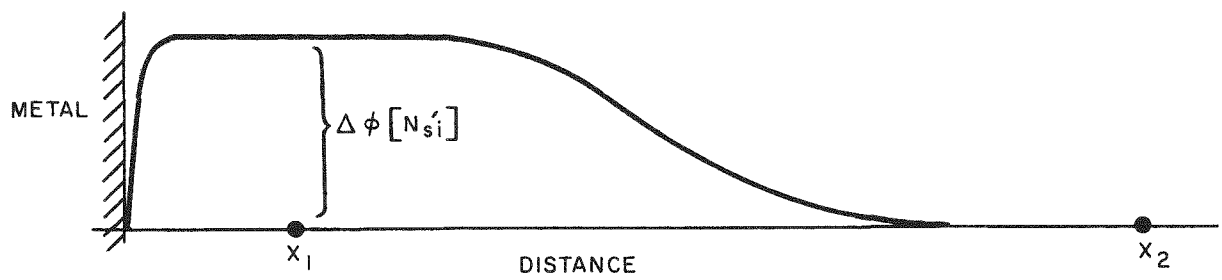

Figure 4. Potential Distribution for Finite Assembly of N_{si}' Dipoles (Points X_1 and X_2 Correspond to Points Shown in Figure 3)

$$\mu_{sa} = - kT \frac{\partial}{\partial N_{sa}} \ln Q \Bigg|_{T,\mathcal{S},\, N_{si}} \qquad \ldots (12)$$

$$\mu_{si} = - kT \frac{\partial}{\partial N_{si}} \ln Q \Bigg|_{T,\mathcal{S},\, N_{sa}} \qquad \ldots (13)$$

where Q is the classical partition function for the particles in the surface phase

$$Q = \frac{1}{N_{sa}!} \frac{1}{N_{si}!} \frac{1}{h^{3N_{sa}}} \frac{1}{h^{3N_{si}}} \int \prod_{i=1}^{N_s=N_{sa}+N_{si}} d^3x_i d^3p_i e^{-H/kT}$$

and H is the complete Hamiltonian of the adsorbed particles. The following expression is considered to approximate the partition function Q:

$$Q = \frac{1}{N_{sa}!} \frac{1}{N_{si}!} \; 2^{N_{sa}} q_a^{N_{sa}} q_i^{N_{si}} \left(\frac{1}{\Lambda^2}\right)^{N_{sa}+N_{si}} e^{N_{si}\phi_{io}/kT}$$

$$e^{N_{sa}(\phi_{ao}+eI)/kT} \exp\left(\sum_{N'_{si}=1}^{N_{si}} e\Delta\phi\,[N_{si}]/kT\right) \mathcal{Z}[N_{sa},N_{si}] \qquad \ldots (14)$$

where the factor 2 is a result of the spin degeneracy of the adatom; $q_a = kT/hf_a$ and $q_i = kT/hf_i$ with f_a and f_i being the frequencies associated with the simple harmonic approximation for the atoms and ions in the direction normal to the metal surface; $\Lambda = h/\sqrt{2\pi MkT}$ and arises from the momentum integrations in the plane of the surface; the exponential factors are associated with the zero of energy which has been taken to be zero for ions or electrons at rest in the gas phase. In Figure 2 the surface atomic state differs from the zero of energy by $\phi_{ao} + eI$; the ionic energy shift can be understood from Figures 3 and 4. Figure 3 shows the container

(Figure 1) on top of a metal of infinite extent. The ion at rest in the gas phase has zero energy by definition. Three steps S_1, S_2 and S_3 are necessary to take an ion from the gas phase to the surface phase as follows:

Step S_1: As shown in Figure 4, an energy $-e\Delta\phi[N'_{si}]$ is required to remove the ion from the gas to a point remote from the finite dipole layer of N'_{si} adions. In Reference 2 a discussion is presented of this figure.

Step S_2: The energy $-\phi_{io}$ is needed next to move the ion up to the bare surface, as shown in Figure 2.

Step S_3: Finally, there is the interaction energy H_s associated with the dipoles as the particles are assembled in the area $\mathcal{A}$. This energy also includes the energy of depolarization.

The energy of steps S_1 and S_2 for N_{si} ions is $N_{si}\phi_{io} + \sum_{N'_{si}=1}^{N_{si}} e\Delta\phi[N'_{si}]$ and appears in the exponentials of Equation 14. The energy associated with S_3 appears in the configuration integral $\mathcal{Z}[N_{sa}, N_{si}]$

$$\mathcal{Z}[N_{sa},N_{si}] = \int \prod_{m=1}^{N_{si}} (d^2x_n) \prod_{n=1}^{N_{sa}} (d^2x_n) \exp(-H_s/kT) \qquad \ldots (15)$$

with

$$H_s = \frac{1}{2} \sum_{1\le i<j\le N_{si}} \frac{M_o M}{r^3_{ij}} + \sum_{\substack{\text{ion}\\+\\\text{atoms}}} u(ij) \qquad \ldots (16)$$

where r_{ij} is the distance between particles i and j, M_o and $M=M_o-\alpha\mathcal{E}$ are the dipole moments at zero and finite coverage, α is the polarizability, and $\mathcal{E}$ is the electric field given by

$$\mathcal{E} = \sum_{i\neq j} \frac{M}{r^3_{ij}} \qquad \ldots (17)$$

in the dipole approximation to be used. The dipole moments have been

replaced by their average values. The dipole-dipole term involves M_oM, rather than MM, because of the energy involved in depolarization. Both the atoms and ions have been assumed to have identical hard core potentials given by u(ij). The interaction of the particles with the metal is assumed to be uniform; that is, no lattice sites exist.

The configuration integral can be expressed in a different form[5] which is amenable to approximate calculations:

$$\mathcal{Z}[N_{sa},N_{si}] = \mathcal{J}_f^{N_{si}+N_{sa}} e^{-N_{si}\varphi/2kT} \qquad \ldots (18)$$

where $\mathcal{J}_f^{N_s}$ is defined by

$$\mathcal{J}_f^{N_s} = \int \prod_{n=1}^{N_s} (d^2x_n)\, e^{-\Sigma u(ij)} \qquad \ldots (19)$$

and is the configuration integral for the hard core problem. The energy φ, defined by Equation 18, is related to the average energy E_s,

$$E_s = \frac{\int \prod_{n=1}^{N_{sa}} (d^2x_n) \prod_{m=1}^{N_{si}} (d^2x_m)\, H_s e^{-H_s/kT}}{\int \prod_{n=1}^{N_{sa}} (d^2x_n) \prod_{m=1}^{N_{si}} (d\, x_m) e^{-H_s/kT}}, \qquad \ldots (20)$$

by

$$-\, kT^2 \frac{\partial}{\partial T}\left[\frac{N_{si}\varphi}{2kT}\right] = E_s \qquad \ldots (21)$$

The chemical potentials μ_{si} and μ_{sa} can be calculated from Equations 12, 13, 14 and 18

$$\mu_{si} = kT \ln \frac{N_{si}\Lambda^2}{q_i\mathcal{J}_f} - \phi_{io} - e\Delta\phi - \frac{N_{si}kT}{\mathcal{J}_f}\frac{\partial\mathcal{J}_f}{\partial N_{si}} + \frac{1}{2}\frac{\partial}{\partial N_{si}}(N_{si}\varphi) \qquad \ldots (22)$$

$$\mu_{sa} = kT \ln \frac{N_{sa}\Lambda^2}{2q_a \mathcal{S}_f} - (\phi_{ao}+eI) - \frac{N_{sa}kT}{\mathcal{S}_f}\frac{\partial \mathcal{S}_f}{\partial N_{sa}} + \frac{1}{2}\frac{\partial}{\partial N_{sa}}(N_{si}\varphi) \qquad \ldots (23)$$

The departure rates ν_i and ν_a are then derived from Equations 2, 3, 7, 8, 22 and 23.

$$\nu_i = \frac{N_i}{V}\sqrt{\frac{kT}{2\pi M}} = f_i \frac{N_{si}}{\mathcal{S}_f} \exp\left(-\frac{N_{si}}{\mathcal{S}_f}\frac{\partial \mathcal{S}_f}{\partial N_{si}}\right)\exp\left(-\frac{\phi_{io}+e\Delta\phi-\frac{1}{2}\frac{\partial}{\partial N_{si}}(N_{si}\varphi)}{kT}\right) \qquad \ldots (24)$$

$$\nu_a = \frac{N_a}{V}\sqrt{\frac{kT}{2\pi M}} = f_a \frac{N_{sa}}{\mathcal{S}_f} \exp\left(-\frac{N_{sa}}{\mathcal{S}_f}\frac{\partial \mathcal{S}_f}{\partial N_{sa}}\right)\exp\left(-\frac{\phi_{ao}-\frac{1}{2}\frac{\partial}{\partial N_{sa}}(N_{si}\varphi)}{kT}\right) \qquad \ldots (25)$$

In Reference 1 the f-factor was defined by

$$\phi_i \equiv \phi_{io} + ef\Delta\phi \qquad .. (26a)$$

A comparison of Equation 26a with the last factor of Equation 24 yields

$$f = 1 - \frac{1}{2e\Delta\phi}(N_{si}\varphi) \qquad .. (26b)$$

The temperature dependence of ϕ_i (B_i in Langmuir and Taylor's notation) is so weak for Cs-[W] that it was not observed by Langmuir and Tyalor. The expression of Equations 24 and 25 in the form

$$\log \nu_{i,a} = A_{i,a} - B_{i,a}/T$$

is not unique when $B_{i,a}$ is a function of temperature. In this case, the departure rates ν_a and ν_i should be compared with experiment rather than the non-unique A and B coefficients.

A different expression for ν_a can be obtained by combining Equations 10 and 11

$$\frac{N_a}{N_i} = 2 \exp\left[e\,(I-\phi)/kT\right] \qquad \ldots (27)$$

Then Equations 24 and 27 yield

$$\nu_a = \frac{N_a}{N_i} \nu_i = 2 f_i \frac{N_{si}}{\mathcal{J}_f} \exp\left(-\frac{N_{si}}{\mathcal{J}} \frac{\partial \mathcal{J}_f}{\partial N_{si}}\right) \exp\left(-\frac{\phi_a^*}{kT}\right) \quad \ldots (28)$$

with

$$\phi_a^* = \phi_i - eI + e\phi$$

Langmuir and Taylor[4] have used forms such as Equations 24 and 28 as indicated by the fact that their B_a and B_i differ by ln2.

The ratio of the number of adatoms to adions can be obtained by comparing Equations 25 and 28

$$\frac{N_{sa}}{N_{si}} = 2 \frac{f_i}{f_a} \frac{\exp\left(\mathcal{J}_f \phi_i\right)}{\exp\left(\mathcal{J}_f \phi_a\right)} \exp\left(-\frac{E}{kT}\right) \quad \ldots (29)$$

with

$$E = \phi_a^* - \phi_{ao}, \ \theta_i = N_{si}/N_{so}, \ \theta_a = N_{sa}/N_{so}$$

N_{so} being the number of cesium particles in a monolayer. This equation can also be obtained directly from the condition for chemical equilibrium,

$$\mu_{sa} = \mu_{si} + \mu_e.$$

BRAGG-WILLIAMS APPROXIMATION

An approximate form for $Z_{N_{sa}, N_{si}}$ in Equation 18 can be obtained with a Bragg-Williams-type approximation.[2] First, the factor $\mathcal{J}_f$ is evaluated for low surface densities:

$$(\mathcal{J}_f)^{N_{sa}+N_{si}} = \int \prod_{m=1}^{N_{si}} (d^2 x_m) \prod_{n=1}^{N_{sa}} (d^2 x_n) \, e^{-\Sigma u(ij)/kT}$$

$$\simeq \mathcal{J}^{N_{sa}+N_{si}} \left(1 - \frac{1}{2} \frac{N\pi r^{*2}}{\mathcal{J}}\right)^{N_{sa}+N_{si}} \quad \ldots (30)$$

with r being the hard-core radius of u(ij). Thus

$$\mathcal{J}_f = \mathcal{J} - \frac{1}{2} N\pi r^{*2}$$

The r^* was chosen as in Reference 2 so that $\sigma_1 \pi r^{*2} = 2$, where σ_1 = density of a monolayer for Cs-[W] = 3.563×10^{14} cm^{-2}, and then $r^* = 4.2 \times 10^{-8}$ cm. Consequently,

$$\mathscr{S}_f = \mathscr{S}(1-\theta) \equiv \mathscr{S}(1-\theta_i-\theta_a) \qquad \ldots (31)$$

and the "entropy" factor in the departure rates will have the same form that Langmuir and Tyalor obtained, that is, the A_i and A_a factors. Equation 31 may be compared with the more accurate expression of Tonks[6]

$$\mathscr{S}_f = \frac{1 - 1.307\theta^3 + 0.307\theta^4}{1 + 1.814\theta + 2.573\theta^2}$$

Equation 31 is assumed to be true for all coverages, although this is rigorously true only for small coverages.

The energy φ calculated in Equation 18 is calculated from the approximate form of E_s obtained by the Bragg-Williams approximation. E_s is first rewritten

$$E_s = \frac{1}{2} N_{si} \bar{\varphi} \qquad \ldots (32)$$

$$\bar{\varphi} = \int d^2 x_2 \; g_i(\vec{x}_1, \vec{x}_2) \; H_i(\vec{x}_1, \vec{x}_2) \frac{N_{si}}{\mathscr{S}} \qquad \ldots (33)$$

$$g_i(\vec{x}_1, \vec{x}_2) = \frac{\mathscr{S}^2 N_{si}}{N_{si}^2 (N_{si}-2)!} \frac{1}{Z[N_{sa}, N_{si}]} \int d^2 x_3 \ldots d^2 x_N e^{-H_s/kT} \qquad \ldots (34)$$

where $H_i(\vec{x}_1, \vec{x}_2)$ is the interaction energy of ions 1 and 2 according to Equation 16. The Bragg-Williams approximation consists of setting the pair correlation function $g_i(\vec{x}_1, \vec{x}_2)$ in Equation 33 equal to that for a random distribution of particles outside the hard-core radius r^*. One then obtains from Equations 21, 32, 33 and 34

$$\varphi = \bar{\varphi} = \frac{N-1}{N_{si}} \frac{\mathscr{S}}{\mathscr{S}-b} \int_{r^*}^{\infty} \frac{N_{si}}{\mathscr{S}} \; \frac{1}{2} \; \frac{M_o M}{r^3} \quad 2\pi r dr \qquad \ldots (35)$$

$$= \frac{2\pi N_{si}}{\mathscr{S}_{r^*}} \; \frac{M_o M}{2}$$

The electric field $\mathcal{E}$ for this distribution is given by

$$\mathcal{E} = \int_{r^*}^{\infty} \frac{M}{r^3} \frac{N_{si}}{\mathcal{S}} 2\pi r dr = \frac{2\pi N_{si}}{\mathcal{S} r^*} M \qquad \ldots (36)$$

and then

$$M = M_o - \alpha\mathcal{E} = \frac{M_o}{1 + \alpha \frac{2\pi N_{si}}{r^*}} \qquad \ldots (37)$$

The chemical potentials can now be calculated from Equations 22 and 23 with Equations 31, 35 and 37

$$\mu_{si} = kT \ln \frac{N_{si}\Lambda^2}{q_i \mathcal{S}_f} - \phi_{io} - e\Delta\phi + \frac{\mathcal{S}}{\mathcal{S}_f} \theta_i kT + \frac{\varphi}{1 + \frac{2\pi\alpha}{r^*} \sigma_1 \theta_i} \qquad \ldots (38)$$

$$\mu_{sa} = kT \ln \frac{N_{sa}\Lambda^2}{2q_a \mathcal{S}_f} - (\phi_{ao} + eI) + \frac{\mathcal{S}}{\mathcal{S}_f} \theta_a kT \qquad \ldots (39)$$

Similarly, the departure rates are obtained from Equations 24 and 25

$$\nu_i = f_i \frac{N_{si}}{f} \exp\left(\frac{\mathcal{S}}{\mathcal{S}_f}\right) \theta_i \exp\left(- \frac{\phi_{io} + e\Delta\phi - \frac{\varphi}{1 + \frac{2\pi\alpha\sigma_1}{r^*} \theta_i}}{kT}\right) \qquad \ldots (40)$$

$$\nu_a = f_a \frac{N_{sa}}{\mathcal{S}_f} \exp\left(\frac{\mathcal{S}}{\mathcal{S}_f} \theta_a\right) \exp\left(- \frac{\phi_{ao}}{kT}\right) \qquad \ldots (41)$$

This work function change $\Delta\phi$ is given by

$$\Delta\phi = \frac{2\pi\sigma_1 M_o \theta_i}{1 + \bar{\alpha}\theta_i} = \frac{4 M_o}{r^{*2}} \frac{\theta_i}{1 + \bar{\alpha}\theta_i} ; \quad \bar{\alpha} = \alpha \frac{2\pi\sigma_1}{r^*} \qquad \ldots (42)$$

It will be shown that $\theta \cong \theta$ for $\theta < 0.50$. The constants $\bar{\alpha}$ and $4M_o/r^{*2}$ in Equation 42 have been determined previously in Reference 2 to be

$$\frac{4M_o}{r^{*2}} = 10.8 \; ; \; \bar{\alpha} = 2$$

The f-factor is obtained from Equations 26b and 35

$$f = 1 - \frac{1}{2e\Delta\phi} \frac{\partial}{\partial N_{si}} (N_{si}\varphi)$$

$$= 1 - \frac{\varphi}{e\Delta\phi} \frac{1+\frac{\bar{\alpha}}{2}\theta_i}{1+\bar{\alpha}\theta_i} = 1 - \frac{M_o}{2er^*} \frac{1+\theta_i}{1+2\theta_i} \qquad \ldots (43)$$

$$= 1 - 0.4 \frac{1+\theta_i}{1+2\theta_i}$$

Thus the f-factor increases slowly from 0.60 at $\theta_i = 0$ to 0.73 at $\theta_i = 1.00$. Experimentally,[7] f decreases from 0.8 at $\theta = 0$ to 0.65 at $\theta = 0.80$. For Cs-[W], $\theta \cong \theta_i$ for $\theta < 0.55$. The above discrepancy is considered minor since the main dependence of ϕ_i on θ occurs through the factor $\Delta\phi$ in Equation 26a, f being approximately constant.

CALCULATION OF $\Delta\phi(\theta,T)$

This section is divided into two parts. First, the modifications of the earlier theory[1,2] in the light of the theory just developed are described. In the second part the effects of adatom polarizability are investigated.

Modifications of Earlier Theory

The work function change is given implicity by the two Equations 29 and 42 in the two unknowns θ_i and $\Delta\phi$ for given θ and T. Previously, in Reference 1, the atom to ion ratio was assumed to be given by a simple Boltzmann factor with a degeneracy factor of 2. The correctness of the factor 2 is very questionable. According to Equation 29, based on a chemical equilibrium for $Cs \leftrightarrow Cs^+ + e^-$, the degeneracy factor is given by

$$2 \frac{f_i}{f_a} \frac{\exp \frac{\partial \theta_i}{\partial f}}{\exp \frac{\partial \varepsilon_a}{\partial f}} = 2 \frac{f_i}{f_a} \exp\left(\frac{\theta_i - \theta_a}{1 - \theta}\right)$$

Before discussing Equation 29 further, it is interesting to evaluate θ_i as a function of θ from Langmuir and Taylor's experimental $\Delta\phi(\theta)$ with Equation 42

$$\Delta\phi = \frac{10.8\ \theta_i}{1+2\theta_i} \text{ volts} \quad \text{or} \quad \theta_i = \frac{\Delta\phi(\theta)}{10.8 - 2\Delta\phi(\theta)}$$

The results are shown in Table I.

TABLE I. ADION COVERAGE θ_i VS. TOTAL COVERAGE θ FOR ZERO ADATOM POLARIZABILITY

$\Delta\phi(\theta)$ =	0.874	1.500	2.003	2.420	2.73	2.83	2.89	2.92	2.92	2.90	2.87
θ =	.10	.20	.30	.40	.50	.55	.60	.65	.70	.75	.80
θ_i =	.097	.192	.295	.406	.511	.551	.576	.589	.589	.580	.567
θ_i/θ =	.975	.96	.98	1.02	1.02	1.00	.96	.91	.87	.77	.71
$\frac{\theta_i-\theta_a}{1-\theta}$ =	.11	.25	.43	.67	1.00	1.22	1.38	1.51	1.59	1.64	1.67

The difference between θ_i and θ for $\theta<0.55$ is not considered to be caused by adatoms; for example, patchiness of the tungsten filament might be important, but has not been considered.[7] The strong decrease of θ_i/θ for $\theta>0.55$ is considered to be real. It might be noted now, however, that in the second part of this section the inclusion of adatom polarizability leads to many less adatoms. In both cases, the rapid turnover of $\Delta\phi(\theta)$ for $\theta>0.55$ is to be attributed to adatoms.

In Equation 29, at the lower coverages the energy factor E is dominant, and $\theta_a \ll \theta_i$. At the higher coverages, $\theta>0.55$, the preceding table shows that $(\theta_i-\theta_a)/(1-\theta)$ is slowly varying, but so is $E = E_o-(1-f)\Delta\phi$ since $\Delta\phi$ is near maximum. At these higher coverages, the model is uncertain because of other factors such as lateral bonding of cesium so that the description of simple dipoles may no longer be valid. It is therefore practical to take

$$\frac{N_{sa}}{N_{si}} = A \exp\left(-\frac{E}{kT}\right) \qquad \ldots (44)$$

with A considered a constant independent of substrate material.

In the previous analysis,[1] the electric field was taken to be

$$\mathcal{E} = \frac{(1-f)\Delta\phi}{er_i} \qquad \ldots (45)$$

which is to be compared with Equation 36. Equation 21 of Reference 1 results if the electric field is given by Equation 45 rather than Equation 36. In solving Equation 21 of Reference 1 for $\Delta\phi(\theta,T)$, the additional θ-dependence through the (1-f) factor is not necessary but does help in obtaining a maximum in $\Delta\phi(\theta)$. The (1-f) factor (taken to be that experimentally determined) in the <u>energy</u> E of Equation 44 is actually sufficient to obtain the $\Delta\phi$-maximum. The (1-f) factor in the electric field in Equation 45 is not on firm theoretical ground since the term $f\Delta\phi$ can be considered to consist of two parts: 1) the energy to rearrange the surface particles from the initial to the final configuration; and 2) the energy to bring the ion to the surface under the electric field of the final configuration. Despite the above uncertainties, the electric field expression, Equation 45, will be maintained since the (1-f) factor is varying slowly and any resulting changes in $\Delta\phi(\theta,T)$ from the use of Equation 45 instead of Equation 36 should be minor. Two effects, atomic polarizability (to be discussed below) and lateral bonding, have been neglected so that the $\Delta\phi$-results at high coverages will be only semi-quantitative. The results presented in Reference 1 must now be reinterpreted slightly with the following ambiguity. From Equation 44 and the expression obtained in Reference 1 for N_{sa}/N_{si} which fits the Cs-[W]

$$\frac{N_{sa}}{N_{si}} = A\exp\left(-\frac{E_o-(1-f)\Delta\phi}{kT}\right) = 2\exp\left(-\frac{1.054-(1-f)\Delta\phi}{.052}\right) \qquad \ldots (46)$$

and thus with $A \equiv 2e^{-I}$ it is necessary that

$$\Psi + 19.2\ E_o = 20.3$$

for example with $\Psi = 0$, $E_o = 1.054$ ev. For $\Psi = 1$, $E_o = 1.01$ ev and for $\Psi = -1$, $E_o = 1.11$ ev. Thus for A not differing from 2 by orders of magnitude, E_o remains approximately 1 ev. In this manner, the rapid turnover of $\Delta\phi(\theta,T)$ with respect to θ at approximately 50% coverage can be explained by the existence of adatoms with an atomic energy of evaporation

$$\phi_{ao} = \phi_o - I + \phi_{io} - E_o = 4.62 - 3.87 + 2.04 - E_o$$

$$= 2.79 - E_o$$

which is in fair agreement with deBoer's rough estimate,[8] $\phi_{ao} \approx 1.4$ ev.

Inclusion of Atomic Polarizabilities

It is to be expected that the adatoms will be polarized by the electric field; therefore, the adatoms will decrease directly the work function change $\Delta\theta$. This effect is easily included in the theory, and the basic equations now become

$$M_i = M_o - \alpha\mathcal{E} \qquad \ldots (47)$$

$$M_a = -\alpha_a\mathcal{E} \qquad \ldots (48)$$

$$\Delta\phi = 2\pi\sigma_1(M_i\theta_i + 2M_a\theta_a) \qquad \ldots (49)$$

$$= \frac{2\pi\sigma_1}{r^*}(M_i\theta_i + M_a\theta_a) \qquad \ldots (50)$$

$$\frac{\theta_a}{\theta_i} = Ae^{-E/kT} \qquad \ldots (51)$$

in the Bragg-Williams-type approximation, where α_a is the atomic polarizability and the factor 2 arises in Equation 49 because the dipole lies outside the metal surface. At zero coverage, the adatom is assumed to have a negligible dipole moment. Without the Bragg-Williams-type approximation, the induced dipole moment M_a will depend on the location of the atom

relative to the ions. At high coverages ($\theta > 0.55$) where we shall find adatoms present, each adatom has two or more adions as nearest neighbors. The surface is sufficiently crowded that the electric field in Equation 50 is a good approximation. At low coverages adatoms might be expected to be found adjacent to adions according to the attractive dipole-dipole interaction (in Reference 8 a different reason is given). In this event, it should be noted that by electrostatics the electric field at the center of the atom due to the adion and its image has its vertical component pointing towards the substrate rather than away as depicted by deBoer. deBoer has recently discarded this picture of adatoms adjacent to adions and now considers the adsorbed cesium as one species whose adsorption bond changes with coverage.[9]

Equations 47-50 can be combined to obtain

$$\Delta\phi = 2\pi\sigma_1 M_o \theta_i \frac{1-\alpha_a C\theta}{1+\alpha C\theta_i + \alpha_a C\theta_a} \qquad \ldots (52)$$

$$C = \frac{2\pi\sigma_1}{r^*}$$

which should be compared with Equation 42. Equation 52 offers another means for obtaining the $\Delta\phi$ maximum. Equation 52 can be used to obtain θ_i, and $\theta_a = \theta - \theta_i$, from the experimental $\Delta\phi(\theta)$ if the adatom and adion polarizabilities are assumed equal. Table II was obtained with

$$\Delta\phi = 10.8\theta_i \frac{1-\theta+\theta_i}{1+2\theta} \qquad \ldots (52)$$

TABLE II. ADION COVERAGE θ_i VS. TOTAL COVERAGE θ FOR EQUAL ADATOM AND ADION POLARIZABILITIES

θ	0.10	0.20	0.30	0.40	0.50	0.55	0.60	0.65	0.70	0.75	0.80
$\Delta\phi$	.8738	1.500	2.003	2.420	2.73	2.83	2.89	2.92	2.92	2.90	2.87
θ_i	.0974	.194	.297	.402	.504	.550	.593	.633	.669	.704	.737
θ_i/θ	.974	.970	.990	1.01	1.01	1.00	.988	.974	.956	.939	.921

The $\Delta\phi$-maximum is obtained with less adatoms than in Table I, the reason being that the adatoms are directly decreasing $\Delta\phi$ with their induced dipole moments. Previously, the adatoms caused the decrease of $\Delta\phi$ because of the (1-f) factor in E in Equation 46. The values of θ_i are consistent with

$$\frac{\theta_a}{\theta_i} = 2 \exp\left(-\frac{E}{kT}\right) = 2 \exp\left(-\frac{1.19 \text{ ev} - (1-f)\Delta\phi}{.052 \text{ ev}}\right) \quad \ldots (53)$$

where $(1-f)\Delta\phi$ is taken from the experimental data. This form for E is not really correct since no energies involving the adatom dipoles are included. These interactions can be included by rederiving Equations 33 and 35 to obtain a new expression for $\bar{\varphi}$

$$\bar{\varphi} = \int d^2r\, g_i(r)\, H_i(r)\, \frac{N_{si}}{\mathscr{S}} + \frac{N_{sa}}{N_{si}} \int d^2r\, g_a(r)\, H_a(r)\, \frac{N_{sa}}{\mathscr{S}} \quad \ldots (54)$$

$$+ 2 \int d^2r\, \frac{N_{sa}}{\mathscr{S}}\, g_{ai}(r)\, H_{ai}(r)$$

where $g_i(r)$ is the ion-ion pair correlation function given by Equation 34, and $g_a(r)$ and $g_{ai}(r)$ are the atom-atom and atom-ion pair correlation functions given by expressions similar to Equation 34.[4] $H_i(r)$ is the same as in Equation 34. $H_a(r)$ and $H_{ai}(r)$ are the atom-atom and the atom-ion interaction energies, respectively. Equations 18, 21-26 and 32, which involve φ and $\bar{\varphi}$, still hold. The Bragg-Williams approximation for the pair correlation functions could be made in Equation 54 and the evaporation

rates ν_a, ν_i and ν_e calculated. These calculations have not yet been made, but would be relatively simple. It is very likely that other forces besides the dipole-dipole forces envisioned in Equation 54 will be very important at high coverages such as cohesive metallic bonds. The calculation preceding from Equation 54 would then not have much significance.

The significant factor shown in this section is the possible effect of adatom polarization on the work function. It must be remembered that the existence of adatoms and adions as two distinct species is a debatable point. It might be expected, however, that the vibrational spectrum of adatoms and adions would be coverage- and temperature-dependent and that these effects could be observed in infra-red adsorption or reflection spectra. Adsorption as two species, then, would not have to remain a speculative point.

SUMMARY

The previous ONR work[1,2,3] might be summarized as follows. In Reference 2 a statistical mechanical treatment yielded evaporation rates ν_a, ν_i and ν_e in terms of various microscopic constants. Examination of these constants showed how to treat different substrate materials. The treatment yielded the same form for the A-factors ($\nu = e^{A}e^{-B/T}$) that Langmuir predicted (the basic assumptions were the same, but the treatments were quite different in the two cases). The energy factor B was obtained from outside the statistical mechanical formalism, whereas Langmuir did not derive an expression for B. No adatoms were assumed. In Reference 1 adatoms were found capable of explaining the maximum in the work function change. By this means, predictions of $\Delta\phi(\theta,T)$ were for arbitrary substrate. Theoretical expressions for ν_a and ν_i were calculated from the Cs-[W] data by assuming that a variation of the substrate work function left A_a, A_i,

B_i unchanged and changed B_a in a manner indicated in Reference 2. In Reference 3 a calculation of the f-factor ($B_i \sim \phi_i = \phi_{io} + f\Delta\phi$) was made. This calculation did not include any energy associated with the rearrangement of the adions as the test ion is brought to the surface. The results did agree well with the experiment.

The present treatment calculates the expressions for the evaporation rates ν_a, ν_i and ν_e with adatom and adion adsorption. For polarizable adatoms, the calculation of ν_a and ν_i is only indicated. In this treatment, a general expression for the f factor falls directly out of the formalism. In the Bragg-Williams type approximation, $f(\theta_i)$ does not agree with experiment[7] as well as $f(\theta)$ in Reference 3 did, but the agreement was still considered satisfactory. The expressions for ν_a and ν_i differ from those obtained by Langmuir for appreciable adatom coverage. This difference is not in the right direction to explain the small $4.8(\theta-\theta^2/2)$ dependence[4] found experimentally in A_a in addition to that prediction. Finally, it was found possible to explain the maximum in $\Delta\phi$ with adatom polarizabilities whereas previously in Reference 1 it was necessary that the f factor decrease with θ.

There are many points at which the present theory may fail and these have often been pointed out in the text. One point often made was that lateral bonding of the cesium and possible accompanying effects, such as change of polarizability, could greatly affect the calculations. Patchiness of the surface was never included.

Most useful would be measurements of ν_a, ν_i and ν_e as functions of θ and T for a low work function substrate material.

REFERENCES

1. N.S. Rasor and C. Warner, "Correlation of Electron, Ion and Atom Energies," Basic Research in Thermionic Energy Conversion Processes, AI-6799 (1961) p 45
2. C. Warner, "Statistical Mechanical Treatment of Surface Ionization," Basic Research in Thermionic Energy Conversion Processes, AI-6799 (1961) pp 85, 96
3. A.R. Vernon, "Potential of an Ion in a Discrete Dipole Layer," Basic Research in Thermionic Energy Conversion Processes, AI-6799 (1961) p 81
4. J.B. Taylor and I. Langmuir, Phys. Rev. 44 423, 433 (1933)
5. R.H. Fowler and E.A. Guggenheim, Statistical Thermodynamics (Cambridge, 1960) pp 252, 568
6. L. Tonks, Phys. Rev. 50 955 (1936)
7. W.B. Nottingham, "Thermionic Emission," Handbuch de Physik XXI, (1956) p 110
8. J.H. DeBoer, Electron Emission and Adsorption Phenomena (Cambridge, University Press, 1935) pp 81,90
9. J.H. DeBoer, Advances in Catalysis VIII (New York, Academic Press, 1956)
10. T.L. Hill, Statistical Mechanics (New York, 1956) 262 ff

IV. SPACE CHARGE ANALYSIS FOR LOW PRESSURE THERMIONIC DIODES

C. Warner, III

INTRODUCTION

Space charge analyses of collisionless, plane electrode, thermionic converters have been performed by various authors.[1-8] These analyses can be considered as extensions of the work of Langmuir[9] who solved the space charge problem with one charged species. If both ions and electrons are emitted, the potential distribution can assume a variety of forms. This paper first considers the space charge problem for infinite spacings. Particular types of solutions are shown to exist in different regions of η_m, η_{min} space as shown in Figure 1, in which η_m is the dimensionless potential where the electric field first vanishes (this point is sometimes an inflection point); and η_{min} is the potential of the collector. These potentials η_m and η_{min} are shown in Figure 2. In Figure 1 it is shown that the independent paramaters η_m and η_{min} determine the form of the potential distribution. The parameters η_m and η_{min} also determine the volt-ampere curves for given emission conditions (that is, where β is constant). Each point on the volt-ampere curve can be identified with a particular form of potential distribution, and thus the continuous change of potential form becomes apparent as the collector potential η_{min} varies. Finally, the effect of finite spacing is discussed.

THE BASIC EQUATIONS

The potential distributions are obtained by solving Poisson's equation in which the charge density is given in terms of the potential. This expression for the charge density depends on the particular potential shape chosen. The motion of the charged particles is assumed to be governed entirely by the potential distribution η, that is, the Vlasov equation is

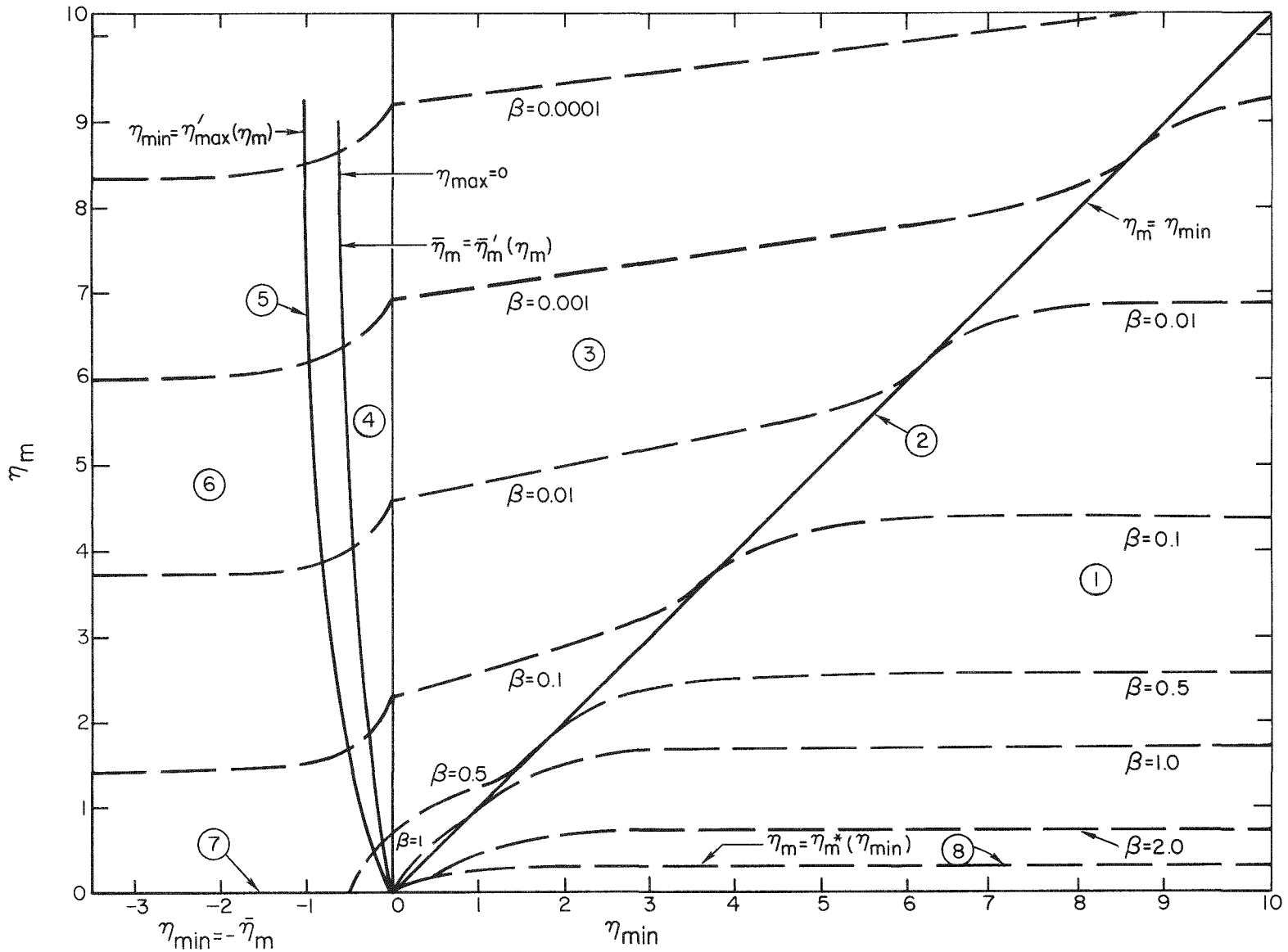

Figure 1. Separation of η_m, η_{min} Space into Regions According to the Shape of the Potential Distribution (The Numbers 1 to 7 Correspond to Curves 1 to 7 in Figure 2 η_m and η_{min} are defined in Figure 2)

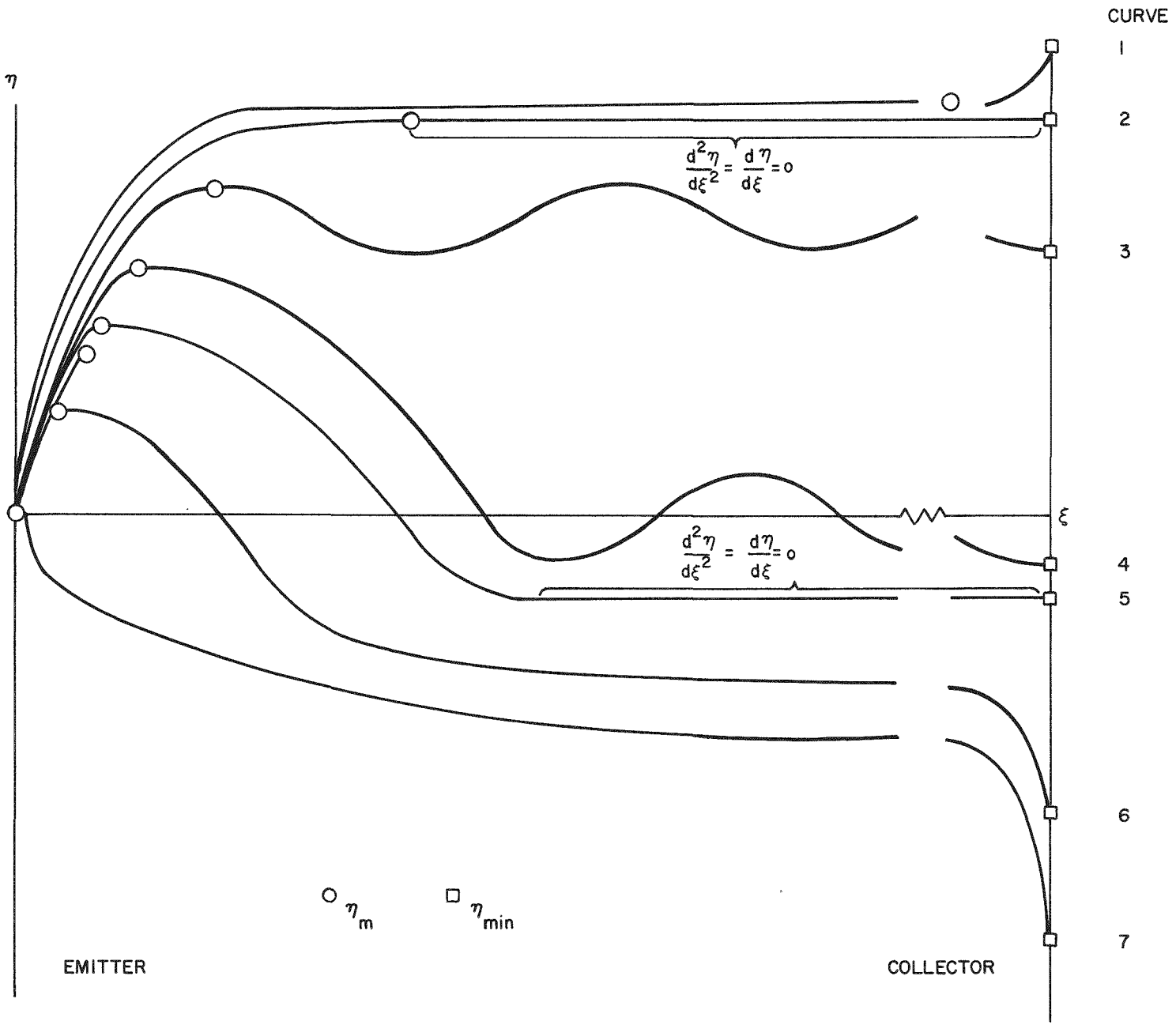

Figure 2. Some Typical Potential Distributions for Infinite Spacing

being solved. The emitted charged particles are assumed to have a Maxwellian distribution corresponding to the emitter temperature.

For the potential distribution shown in Figure 3, Poisson's equation takes the form

$$\frac{d^2\eta}{d\xi^2} = \frac{\beta e^{\eta}}{2}\left\{1-\text{erf}\sqrt{\eta}+\text{erf}\sqrt{\eta+\bar{\eta}}\right\} - \frac{e^{-\eta}}{2}\left\{1 \pm \text{erf}\sqrt{\eta_m-\eta}\right\} \qquad \ldots (1)$$

the plus sign holding for $0<\xi<\xi_m$ and the minus sign for $\xi_m<\xi<\xi_o$. The dimensionless potential is defined by $\eta = eV/kT$, and vanishes at the emitter, V being the potential and T the temperature. The parameter $\beta = n_{-o}/n_{+o}$ where $n_{-o}/2$ and $n_{+o}/2$ are the emitted electron and ion densities at the emitter. The dimensionless distance is measured in ion Debye lengths

$$\xi^2 = \frac{4\pi n_{+o} e^2}{kT} x^2 \qquad x = \text{distance} \qquad \ldots (2)$$

Equation 1 is typical of the form of Poisson's equation. In all cases, the first integration may be done analytically. For the potential distribution of Figure 3, there results

$$\left(\frac{d\eta}{d\xi}\right)^2 = F_1(\eta) - F_1(\eta_m) \qquad 0<\xi<\xi_m \qquad \ldots (3)$$

$$= F_2(\eta) - F_2(\eta_m) \qquad \xi_m<\xi<\xi_o \qquad \ldots (4)$$

$$= F_3(\eta) - F_3(-\bar{\eta}_m) \qquad \xi_o<\xi<\xi_m \qquad \ldots (5)$$

$$= F_4(\eta) - F_4(-\eta_m) \qquad \bar{\xi}_m<\xi<\xi_{max} \qquad \ldots (6)$$

where

$$F_1(\eta) = 2e^{-\eta} - e^{-\eta_m} G(\eta_m-\eta) + 2\beta G(\eta) - \beta e^{-\bar{\eta}_m} G(\bar{\eta}_m+\eta) \qquad \ldots (7)$$

$$F_2(\eta) = e^{-\eta_m} G(\eta_m-\eta) + 2\beta G(\eta) - \beta e^{-\bar{\eta}_m} G(\bar{\eta}_m+\eta) \qquad \ldots (8)$$

$$F_3(\eta) = e^{-\eta_m} G(\eta_m-\eta) + 2\beta e^{\eta} - \beta e^{-\bar{\eta}_m} G(\bar{\eta}_m+\eta) \qquad \ldots (9)$$

$$F_4(\eta) = e^{-\eta_m} G(\eta_m - \eta) + \beta e^{-\bar{\eta}_m} G(\bar{\eta}_m + \eta) \qquad \ldots (10)$$

$$G(\eta) = e^{\eta} \operatorname{erfc} \sqrt{\eta} + \frac{2}{\sqrt{\pi}} \sqrt{\eta} \qquad \ldots (11)$$

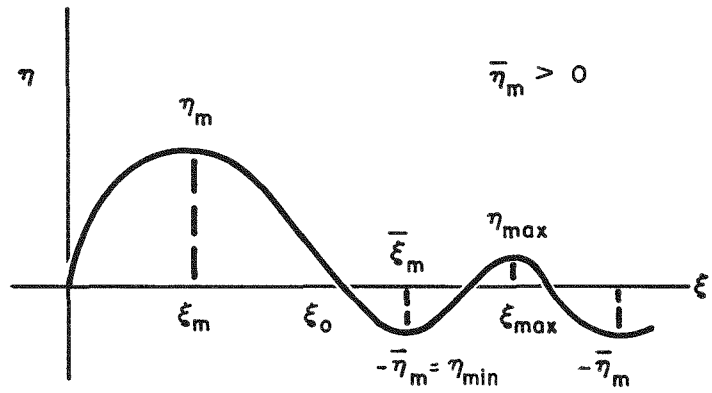

Figure 3. Oscillatory Potential Distribution Exhibiting Potential Maxima, η_m and η_{max}, and Potential Minimum η_{min}

The first integrations for all the various potential forms are basically contained in Equations 7 to 10. For example, the potential distribution for curve 1 in Figure 2 is given by

$$\left(\frac{d\eta}{d\xi}\right)^2 = \left(\frac{d\eta}{d\xi}\right)^2_{\eta=\eta_{min}} + F_1(\eta, \eta_m = \eta_{min}, \bar{\eta}_m = 0) - F_1(\eta=\eta_{min}, \eta_m=\eta_{min}, \bar{\eta}_m=0) \qquad \ldots (12)$$

which is obtained from Equations 3 and 7. As discussed later, the derivative $(d\eta/d\xi)^2 \Big|_{\eta=\eta_{min}}$ must be chosen properly to obtain the vanishing of $(d\eta/d\xi)^2 [\eta, \eta_{min}, \beta]$ at $\eta=\eta_m$.

The parameters β, η_m, $\bar{\eta}_m$ and η_{max} are not independent for the distribution of Figure 3. The continuity of the electric field implies

$$F_2(0) - F_2(\eta_m) = F_3(0) - F_3(-\bar{\eta}_m) \qquad \ldots (13)$$

from which is obtained $\beta=\beta[\eta_m,\bar{\eta}_m]$. The vanishing of the electric field at η_{max} implies

$$F_4(\eta_{max}) - F_4(-\bar{\eta}_m) = 0 \qquad \ldots (14)$$

from which is obtained $\eta_{max} = \eta_{max}\,[\beta,\eta_m,\bar{\eta}_m]$. Similar relationships arise for other potential distributions. It should also be noted that the solution for $\xi>\xi_{max}$ is obtained by reflection of the solution between $\bar{\xi}_m$ and ξ_{max} about $\xi=\xi_{max}$, $2\xi_{max} - \bar{\xi}_m$, etc.

SOLUTIONS FOR INFINITE SPACING

The oscillatory solution shown in Figure 3 corresponds to infinite spacing. In Figure 2 are shown other possible forms for infinite spacing. Solutions 2-5 are also solutions for finite spacing if the collector is placed at any point at which all the ions and electrons are moving towards the collector. Besides the oscillatory solutions, potential distributions such as curves 1, 6 and 7 in Figure 2 are possible. The break in curves 1, 6 and 7 corresponds to an infinite distance. To obtain these solutions, the input parameters must be selected so that the second integral to obtain ξ diverges. For example, in order to obtain curve 1, $\left(\frac{d\eta}{d\xi}\right)^2_{\eta=\eta_{min}}$ in Equation 12 is taken equal to the negative of the minimum of $F_1(\eta,\eta_m = \eta_{min}, \bar{\eta}_m = 0) - F_1(\eta=\eta_{min},\eta_m = \eta_{min}, \bar{\eta}_m = 0)$ with respect to η. The electric field $d\eta/d\xi$ vanishes at the corresponding "plasma potential" and the second integral for ξ diverges logarithmically. A proper choice of β for given values of η_m and $\bar{\eta}_m$ yields curves 6 and 7. That is, with proper choice of β, $\left(\frac{d\eta}{d\xi}\right)^2$ exhibits a minimum with respect to η and also vanishes at that minimum point. The second integral for ξ also diverges.

Systemization of Space Charge Solutions

The various types of solutions shown in Figure 2 are used to define regions on the η_m, η_{min} plot in Figure 1. Lines of constant β are also

shown. The lines labeled with numbers 2, 5 and 7 and the regions with the circled numbers 1, 3, 4 and 6 can be identified with the curves in Figure 2 with the same numbers. The β-values in Figure 1 are given by the following

For $0<\eta_{min}<\eta_m$ (e.g. curve 3 in Figure 2)

$$\beta e^{\eta_m} = \frac{G(\eta_m-\eta_{min})-1}{G(\eta_m)-G(\eta_{min})} \qquad \ldots (15)$$

For $\eta'_{max}(\eta_m)<\eta_{min} = -\bar{\eta}_m \leq 0$ (e.g. curves 4 and 5 in Figure 2

$$\beta e^{\eta_m} = \frac{G(\eta_m+\bar{\eta}_m)-1}{2G(\eta_m)-e^{-\bar{\eta}_m}\left[G(\eta_m+\bar{\eta}_m)+1\right]} \qquad \ldots (16)$$

The function $\eta'_{max}(\eta_m)$ is defined below. Equation 16 is equivalent to Equation 13

For $-\infty<\eta_{min} = -\bar{\eta}_m<\eta'_{max}$(e.g. curve 6 in Figure 2)

$$\beta e^{\eta_m} = \min \frac{G(\eta_m-\eta)-1}{2\left[G(\eta_m)-e^{\eta}\right] + e^{-\bar{\eta}_m}\left[G(\bar{\eta}_m+\eta)-G(\bar{\eta}_m+\eta_m)\right]} \qquad \ldots (17)$$

The minimum is with respect to η for $-\bar{\eta}_m<\eta<0$. Equation 17 is derived from

$$\left(\frac{d\eta}{d\xi}\right)^2 = e^{-\eta_m}\left[G(\eta_m-\eta)-1\right] - \beta\left[e^{-\bar{\eta}_m}\left\{G(\bar{\eta}_m+\eta)-G(\bar{\eta}_m+\eta_m)\right\} + 2\left[G(\eta_m)-e^{\eta}\right]\right] \quad \eta<0 \qquad \ldots (18)$$

$$= A(\eta_m,\eta) - \beta B(\eta_m,\bar{\eta}_m,\eta) = B\left(\frac{A}{B} - \beta\right)$$

The function A/B has a minimum with respect to η and Equation 17 therefore leads to the divergence in the second integration for infinite spacing.

For $\eta^*_m(\eta_{min})<\eta_m<\eta_{min}$(e.g. curve 1 in Figure 2)

$$\beta e^{\eta_m} = \frac{2 - e^{-(\eta_{min}-\eta_m)}G'(\eta_{min}-\eta_m)}{G'(\eta_m)} \qquad \ldots (19)$$

In this region, $(d\eta/d\xi)^2$ is given by Equation 12. According to the definition of η_m as given in the introduction and in Figure 2, Equation 19 is just equivalent to

$$\frac{\partial F_1}{\partial \eta}\,(\eta=\eta_m,\ \eta_m = \eta_{min},\ \bar{\eta}_m = 0) = 0 \qquad \ldots (19)$$

It is also of interest to give the equations for the boundary lines.

For $\eta_m = \eta_m^*\ (\eta_{min})$ (i.e. curve 8 in Figure 1 or 2)

The function $\eta_m^*\ (\eta_{min})$ is given implicitly by

$$\frac{2(e^{\eta_m^*}-1) - e^{-(\eta_{min}-\eta_m^*)}\,G(\eta_{min})-G(\eta_{min}-\eta_m^*)}{G(\eta_m^*)-1}$$

$$= \frac{2 - e^{-(\eta_{min}-\eta_m^*)}\,G'(\eta_{min}-\eta_m^*)}{G'(\eta_m^*)} \qquad \ldots (20)$$

which is obtained by eliminating β from Equation 19 and the equation that states that $\left(\frac{d\eta}{d\xi}\right)^2 = 0$ at the emitter:

$$F_1(\eta_m,\eta_{min},\beta) = F_1(0,\eta_{min},\beta)$$

For $\bar{\eta}_m = \bar{\eta}_m'\ (\eta_m)$ for $\eta_{max} = 0$ (See Figure 3)

The curve $\bar{\eta}_m = \bar{\eta}_m'\ (\eta_m)$ for $\eta_{max} = 0$ is given by

$$\frac{G(\eta_m+\bar{\eta}_m')-1}{2G(\eta_m)-e^{-\bar{\eta}_m'}\,G(\eta_m+\bar{\eta}_m')+1} = \frac{G(\eta_m+\bar{\eta}_m')-G(\eta_m)}{G(\eta_m')-G(0)}\ e^{\bar{\eta}_m'} \qquad \ldots (21)$$

which is obtained by setting $\eta_{max} = 0$ in Equation 14 and eliminating β between Equations 13 and 14.

For $\eta_{min} = \eta_{max}'\ (\eta_m)$ for $\eta_{min} = \eta_{max}$ (see curve 5 in Figures 1 and 2)

This curve is given implicitly by

$$\frac{G(\eta_m-\eta'_{max})-1}{G(\eta_m-\eta'_{max})} = e^{-\eta'_{max}}\, G(\eta_m) - G(\eta_m-\eta'_{max})-1 \qquad \ldots (22)$$

which is obtained by letting $\bar{\eta}_m$ approach $-\eta_{max}$ in Equations 13 and 14 and eliminating β.

The solutions for $\eta_{min} = 0$ are not shown in Figure 2, but serve as a good starting point for explaining Figure 1. The discussion breaks naturally into the three regions, $0<\beta<0.405$, $0.405<\beta<0.786$ and $0.786<\beta<1.000$. The $\beta=0.405$ line is asymptotic to $\eta_m=0$ line for negative η_{min}. The $\beta=(0.786)^{-1}$ line is tangent to the $\eta_m=\eta_{min}$ line at $\eta_{min}\cong.20$ and does not cross that line.

The Region $0.405<\beta<0.786$

The $\beta = 0.5$ line is considered. As the collector voltage η_{min} is varied, the potential distributions will progress through the sequence shown in Figure 2. As η_{min} is increased from zero the oscillating region in curve 3 of Figure 2 decreases in amplitude and wavelength, until finally curve 2 is reached where $\eta_m=\eta_{min}$. As η_{min} is further increased, the potential distribution resembles curve 1. For $\beta = 0.5$, η_m varies little as η_{min} goes to infinity. If η_{min} is made negative, the distribution resembles curve 4, of Figure 2. As η_{min} is made more negative, η_{max} decreases to zero ($\eta_{max}=0$ in Figure 3) and finally $\eta_{max}=\eta_{min}$ (curve 5 in Figures 1 and 2). Curve 5 has $E=d\eta/d\xi=0$ at a finite distance and everywhere thereafter. Further decrease of η_{min} develops a collector sheath. As η_{min} is decreased, η_m finally vanishes and curve 7 in Figure 2 is obtained. To proceed further, the following <u>symmetry principle</u> must be recognized:

> Every ion-rich solution, $\eta=f(\xi)$, with $\beta=\beta_1<1$, corresponds to an electron-rich solution, $\eta=-f(\xi)$, with $\beta=1/\beta_1$. The electron-rich solution is the negative

of the ion-rich solution. The spacing ξ in the electron-rich solution is measured in electron Debye lengths instead of ion Debye lengths for the ion-rich solution. Only the electric charges of the ions and electrons, and not the masses, enter the steady-state equations.

Further decrease of η_{min} for $\beta=0.5$ thus corresponds to an increase of η_{min} from the E(emitter) = 0 curve (curve 8) in the first quadrant along the $\beta=2$ curve. In this manner, as the collector sheath voltage increases without limit, the "plasma potential" ($-\eta_m$ in first quadrant) approaches a finite value asymptotically. In accordance with the symmetry principle, Equation 17 evaluated for $\eta_m=0$ becomes Equation 19 for $\eta_m=\eta_m^*$ under the transformation: $\eta\rightarrow-\eta_m$, $\beta\rightarrow1/\beta$ and $\bar{\eta}\rightarrow\eta_{min}$.

The Region $0<\beta<0.405$

For $\beta<0.405$, as η_{min} goes to negative infinity, a finite barrier remains. This possibility is unexpected since even with electrons only, the barrier can be made to vanish for any finite spacing. This infinite spacing and infinite voltage situation is perhaps unphysical, but is resolved by reference to Figure 4a in the section "Emission Requirements for Removal of Space Charge Barriers." If the limit $\xi_L\rightarrow\infty$ is taken first, then the limit $\eta_L\rightarrow\infty$ results in zero space charge barrier only if $\beta<0.4049$. If $\eta_L\rightarrow\infty$ first, then the space charge barrier is always removed. It must therefore be remember that the formation of a "plasma" is not the only means by which an infinite spacing solution may be obtained. The other means corresponds to increasing the voltage, $-\eta_{min}$, and spacing simultaneously to maintain zero field at the emitter.

The Region $0.786<\beta<1.000$

In this region, the sequence shown in Figure 2 is slightly altered, as shown in Figure 1. For positive η_{min}, the sequence is the same as in Figure 2. As shown in Figure 1, the decrease of η_{min} through negative values leads to the curve E(emitter) = 0, curve 7 of Figure 2. Then proceeding along the "$1/\beta$" curve in Figure 1 from curve 8 in the first quadrant, the sequence runs through the set of curves shown in Figure 4. Curves 9, 10 and 11 in Figure 4 are not found in the sequence for $0<\beta<0.786$, and exist because the "$1/\beta$" curve enters the $\eta_m>\eta_{min}$ region as shown in Figure 1.

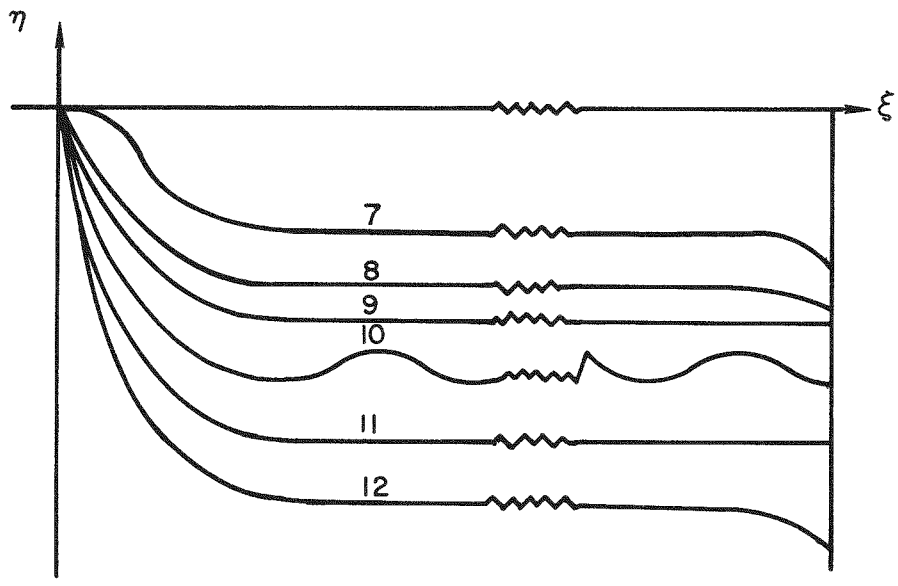

Figure 4. Sequence of Potential Distributions for $0.786<\beta<1.000$

For a given temperature, the volt-ampere curve for a given β is easily extracted since the values of η_m and η_{min} determine the ion and electron currents that pass to the collector. It is important to note that there is a solution and thus a current for all potentials. The load line will

therefore always intersect the diode characteristic to yield an operating point. Calculations indicate that similar steady state solutions exist for finite spacings. Hernqvist[2] and Johnson[3] have claimed to the contrary that steady state solutions, which must also satisfy a load line, do not exist for certain values of β. As will be pointed out later it is actually possible to have two different operating points with different currents at the same potential difference. The explanation for the oscillations (in time) appears more likely to be found in the <u>instability</u> of the steady state solutions in a manner discussed qualitatively by Hernqvist[2] and Johnson[3]. A good discussion on oscillations is presented by Auer in Reference 1.

<u>Existence Proofs</u>

It has been proven analytically that the potential solutions exist for the region bounded by $\eta_m = \eta_{min}$ and $\eta_m = \eta_m^*(\eta_{min})$. That is, the expressions for $\left(\frac{d\eta}{d\xi}\right)^2$ never become negative. Specific solutions have been found in all the other regions. Existence proofs for the other regions were not attempted since it appears certain that the solutions exist, especially since the identification of the E(emitter) = 0 lines in the two quadrants gives the results a certain unity.

SOLUTIONS FOR FINITE SPACING

The oscillatory solutions for infinite spacing are equally solutions for finite spacing if the collector is placed at a position where all the ions and electrons are moving away from the emitter. When this is not the case, the solution will have one of the forms (or the negative thereof) shown in Figure 5. Solutions are obtained by varying β, η_m, and η_{min} in order to satisfy the boundary conditions. The first integrations are all

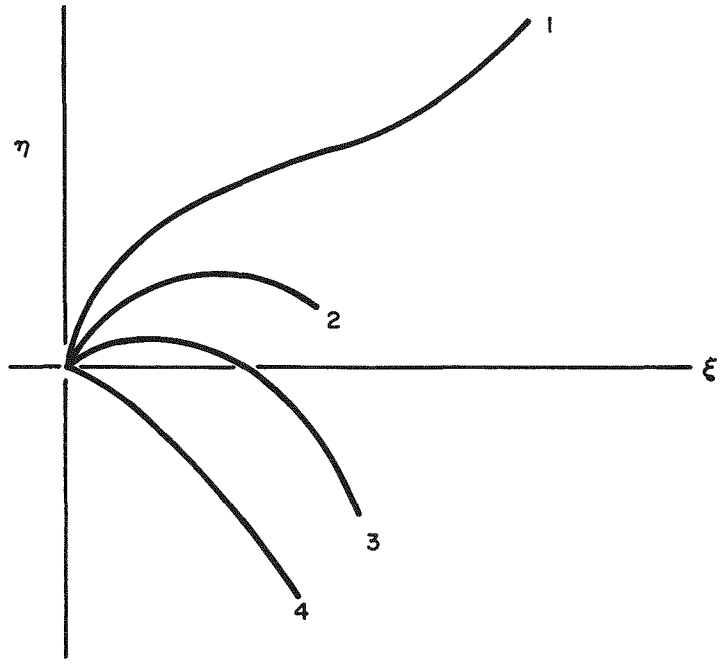

Figure 5. Non-oscillatory Potential Distributions For Finite Spacing

contained in Equations 7 to 10. For finite spacing there are no equations such as 13 and 14. As an example, Equation 12 holds for curve 1 in Figure 5, if η_{min} is interpreted as the collector potential. For given β, η_{min}, and spacing ξ_L, $(d\eta/d\xi)^2_{\eta=\eta_{min}}$ would be varied until the second integration yielded $\xi(\eta_{min}) = \xi_L$.

Of special interest are those solutions which have vanishing electric field at either the emitter or collector, and are thus just space-charge neutralized. These solutions have been discussed in detail in the section "Emission Requirements for Removal of Space Charge Barriers."

In Figure 6, some solutions for $\beta = 0.1$ are shown. It is seen that two solutions with different currents are possible at a given voltage, since the two oscillatory solutions are good finite solutions if the collector is put at either intersection points in Figure 6. This bi-stability has been previously pointed out by Auer.[1] For the example

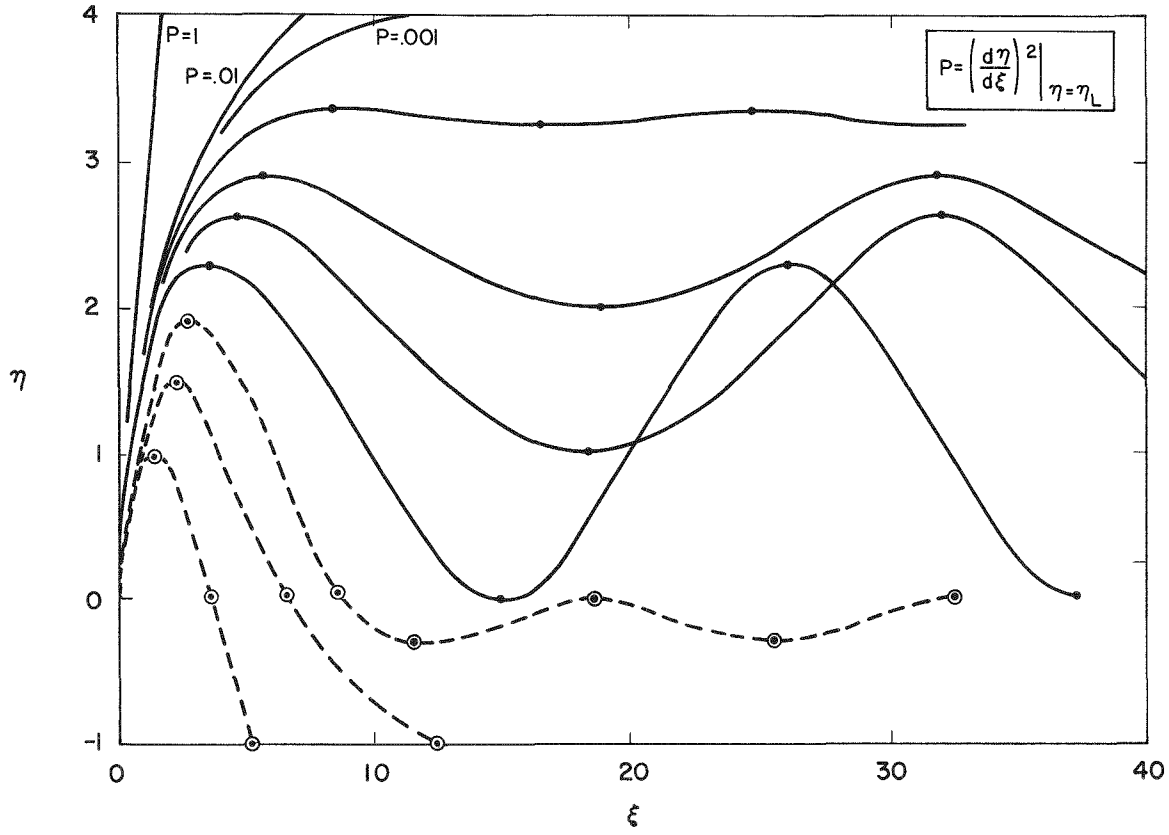

Figure 6. Some Potential Distributions for β = 0.1

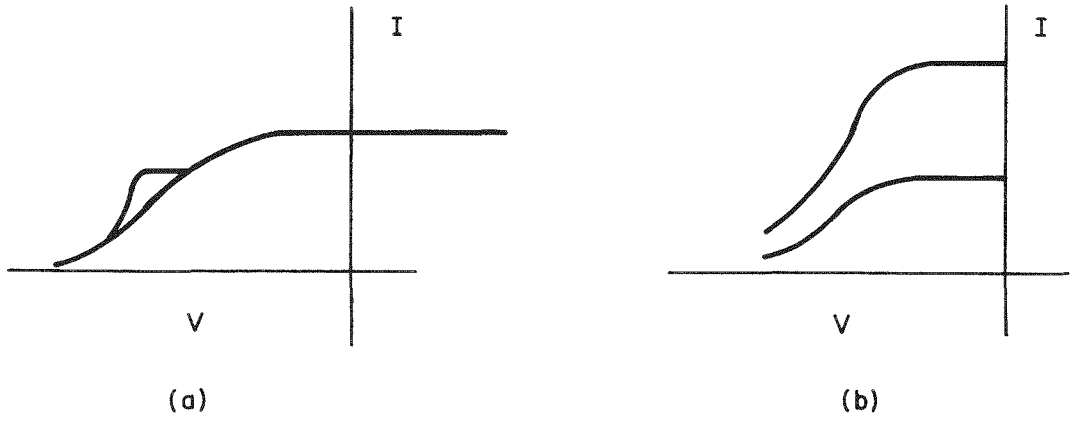

Figure 7. Volt-Ampere Curves Showing Bi-stability
(a) Schematic V-I for β=0.1 According to Figure 6
(b) Type of Bi-stability According to Auer[1]

β=0.1 the volt-ampere curve appears to have the shape shown in Figure 7a rather than that in Figure 7b which is taken from Auer's paper. Figure 7a for a given β=0.1, both modes correspond to oscillatory solutions with potential maximum next to the emitter. Auer's two modes in Figure 7b and his Figure 3a appear to differ in that one mode has a potential maximum and the other a potential minimum next to the emitter. For given β, such a possibility does not seem to exist according to Figure 3. Such a possibility might exist for varying β. Such variations in β may arise from ion barrier charges which affect the total arrival rate.

REFERENCES

1. P.L. Auer, J. App. Phys. 31 2096 (1960)
2. K.G. Hernqvist, RCA Review XXII 7 (1961)
3. F.M. Johnson, RCA Review XXII 21 (1961)
4. M. Ferentz and W.B. Teutsch, Bull. Am. Phys. Soc. 6 29 (1961)
5. C. Warner, "Analysis of the Space Charge Mode in the Cesium Termionic Diode," Basic Research in Thermionic Energy Conversion Processes, AI-6799 (1961) p 145
6. C. Warner, "Space Charge Analysis for Cesium-filled Thermionic Diodes," Paper at Colorado Springs Conference on Thermionic Conversion (May 1961)
7. R.G. McIntyre, J. App. Phys. 33 2485 (1962)
8. P. Mazur, J. App. Phys. 33 2653 (1962)
9. I. Langmuir, Phys. Rev. 21 419 (1923)

V. EMISSION REQUIREMENTS FOR REMOVAL OF SPACE CHARGE BARRIERS

L. K. Hansen and C. Warner, III

INTRODUCTION

The potential distributions for collisionless, plane electrode, converters have been examined to determine the required conditions for converter operation in the retarding field, space charge limited, or saturated emission mode. Such analyses have previously been given for vacuum diodes. The following analysis represents a generalization to the case where ions as well as electrons are generated at the emitter.

VACUUM DIODE

For a vacuum diode with a specific spacing the boundary in volt-ampere space which separates retarding field operation from space charge limited operation is the locus of points whose volt-ampere coordinates are associated with a zero field condition at the collector. Approximate expressions for this boundary curve have been obtained.[1-3] Similarly the curve separating the regions of space charge limited operation and saturated emission operation defines the parameters associated with a zero field condition at the emitter. An approximation of this relationship is the well known Child-Langmuir law.[4-5] The three regions of vacuum diode operation have also been defined by Ferris[6] in terms of universal diode characteristics. Nottingham[3] has used the same approach. In his treatment, however, the space charge limited region appears as the "collapsed" region between his asymptotic master curve and his universal limiting curve.

Langmuir[7] was able to give a universal potential distribution for a plane parallel, vacuum diode operating in the space charge limited mode.

(His analysis has been reviewed and amplified by Foritsky.[8]) Langmuir defined the reduced variables*

$$\xi = 4\left(\frac{\pi}{2kT}\right)^{3/4} m^{1/4} (ei)^{1/2} (x-x_m) \qquad \ldots (1)$$

$$\eta = \frac{V-V_m}{kT} \qquad \ldots (2)$$

where i is the current density through the diode, x_m the position of the potential minimum and V_m the value of the potential minimum. Langmuir's solution for $x>x_m = 0$ is the zero emitter field solution. The solution for $x<x_m = 0$ is the zero collector field solution. Since these are universal curves they also represent the boundaries, in η-ξ space, between the regions of retarding field, space charge limited and saturated emission operation. In this interpretation ξ can be thought of as a current coordinate ($i \sim \xi^2$) with a coordinate scale which depends upon spacing. The coordinate η becomes the potential difference η_L across the diode. These universal boundaries separating the three regions of diode operation are shown in Figure 1. (Data for these curves can be obtained from Kleynen.[9]) A sample volt-ampere characteristic is shown by the dashed line.

The magnitude of the space charge barrier is also obtained easily from Langmuir's solution of the general potential distribution. A plot in η-ξ space of a curve representing the constant barrier height is obtained simply by the appropriate translation of Langmuir's solution for the potential distribution. In the coordinate system of Figure 1, the translated curve

$$\xi(\eta_L;\eta_A = \text{const.}) = \xi(-\eta_A) + \xi(\eta_L + \eta_A) \qquad \ldots (3)$$

* These reduced variables differ from those used in the preceding section, but are closely related to the former variables because of symmetry between ions and electrons in the space charge equations. In the preceding paper, ξ is measured in terms of the <u>emitted</u> current and η is zero at the emitter.

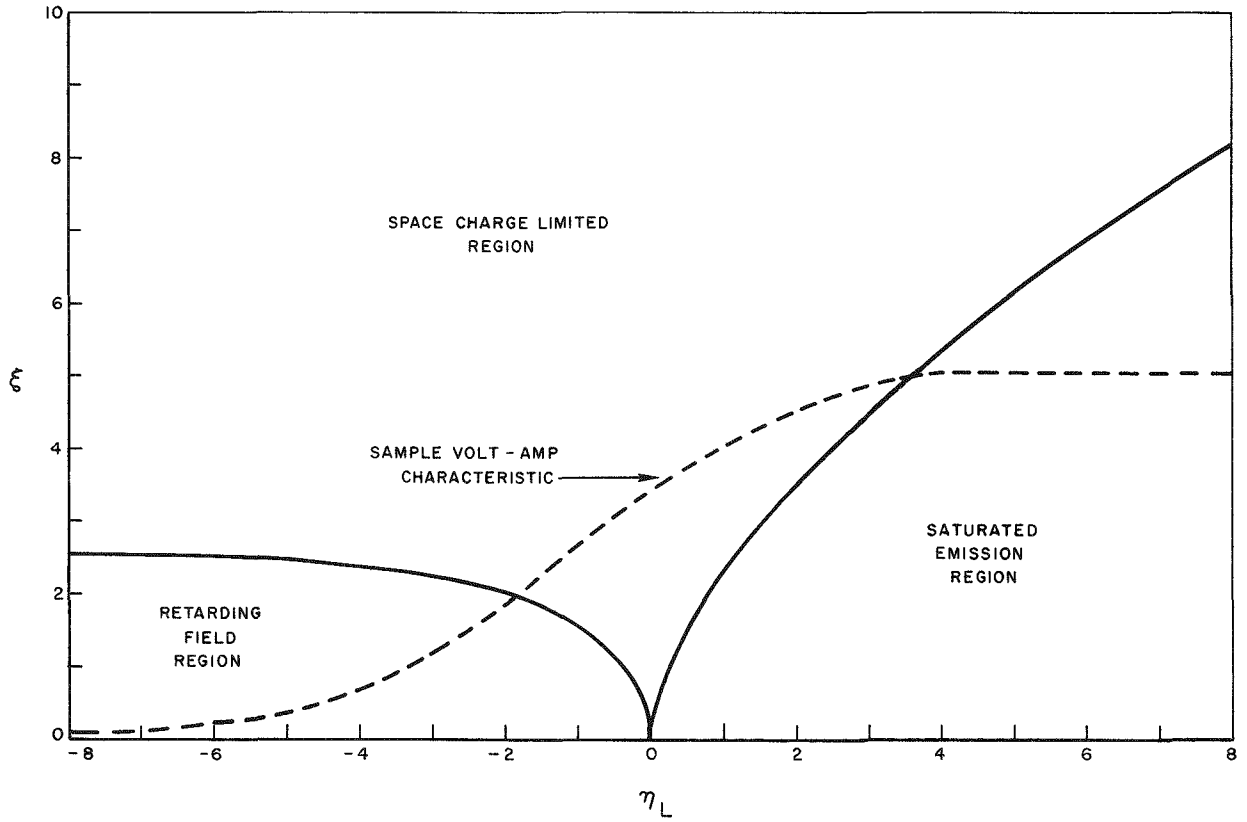

Figure 1. Regions of Vacuum Diode Operation

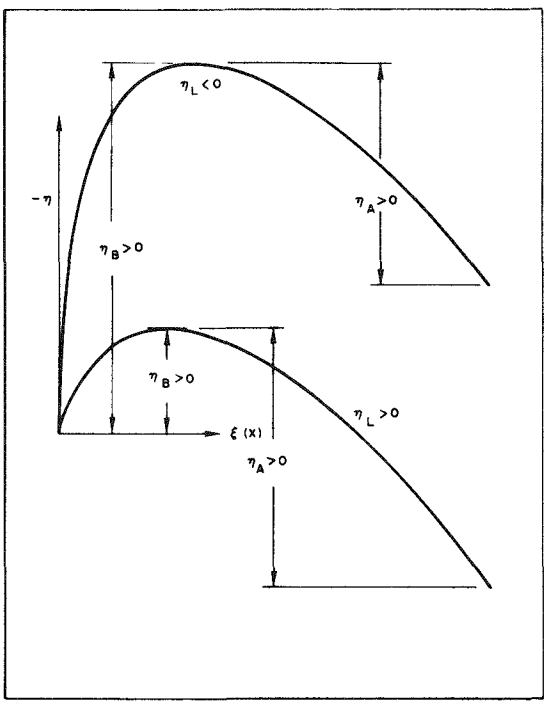

Figure 2. Definition of Symbols

is the locus of parameters η_L and ξ for which there is a constant potential difference, η_A, between the potential minimum and the collector. For $\eta_L<0, \eta_A$ is the magnitude of the space charge barrier as shown in Figure 2. The translated curve

$$\xi(\eta_L;\eta_B = \text{const.}) = \xi(\eta_B) + \xi(\eta_L-\eta_B) \qquad \ldots (4)$$

represents the locus of parameters for which the potential barrier $\eta_{(B)}$ between the potential minimum and the emitter is constant. For $\eta_L>0, \eta_B$ is the magnitude of the space charge barrier as well as the total potential barrier. For $\eta_L<0$, η_B, the total potential barrier is the sum of the diode potential η_L and the magnitude of the space charge barrier η_A. These potential notations are illustrated in Figure 2. The translated curves are shown in Figure 3.

GENERALIZATION TO INCLUDE ION EMISSION

The equations necessary to generalize Figure 1 to include plane parallel diodes which emit ions as well as electrons at the emitter have already been examined by a number of authors.[10] These analyses are based upon the assumption that there are no collisions in the diode interelectrode space. Poisson's equations, using this assumption, become

$$-\frac{d^2\eta}{d\xi^2} = \beta e^{-(\eta+\eta_L)}\left\{1-\text{erf}\sqrt{(\eta+\eta_L)}\right\} - \frac{e^{\eta+\eta_L}}{2}\left\{1+\text{erf}\sqrt{\eta}\right\} \qquad \eta_L>0 \qquad \ldots (5)$$

$$-\frac{d^2\eta}{d\xi^2} = \frac{\beta e^{-\eta}}{2}\left\{1+\text{erf}\sqrt{\eta_L-\eta}\right\} - \frac{e^{\eta}}{2}\left\{1-\text{erf}\sqrt{\eta}\right\} \qquad \eta_L>0 \qquad \ldots (6)$$

for the retarding field and saturated emission cases respectively, where η_L is the potential difference across the diode and β* is the ratio of the

* The quantity β given by Equation 7 is the reciprocal of the β found in the preceding paper. The above notation is becoming more conventional and is adopted here because the present paper is not a continuation of previous work.

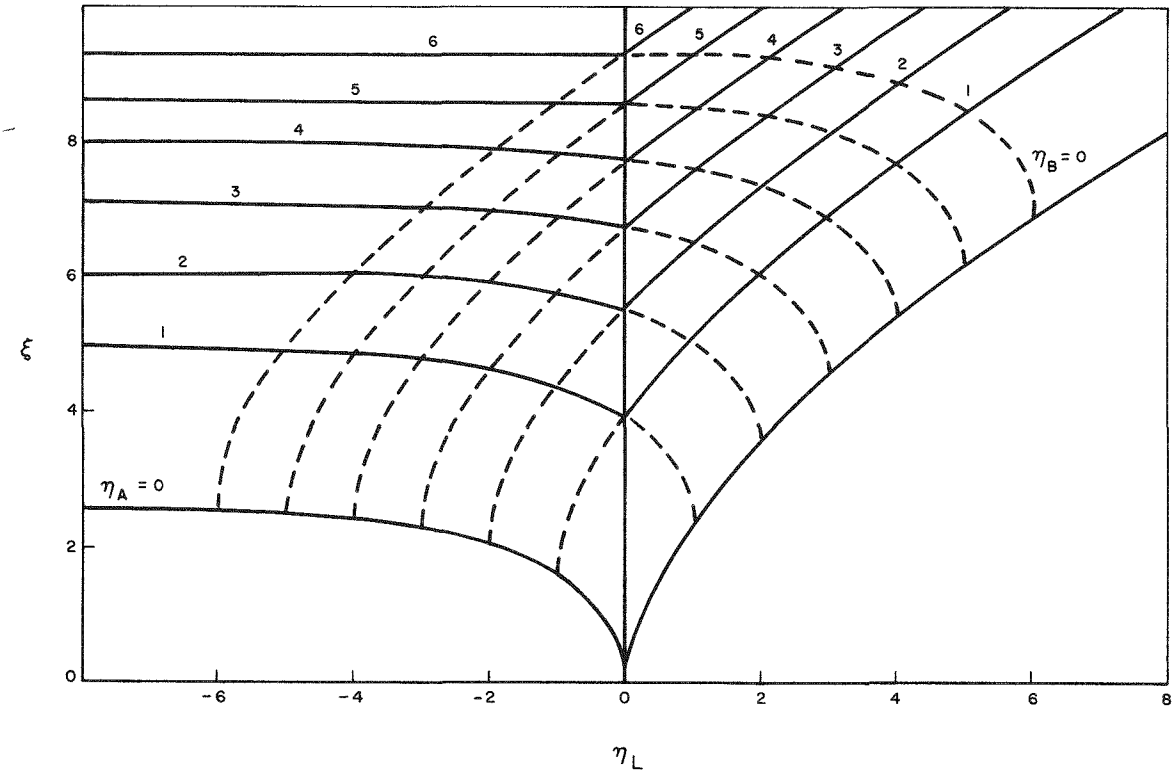

Figure 3. Magnitude of Space Charge Barriers

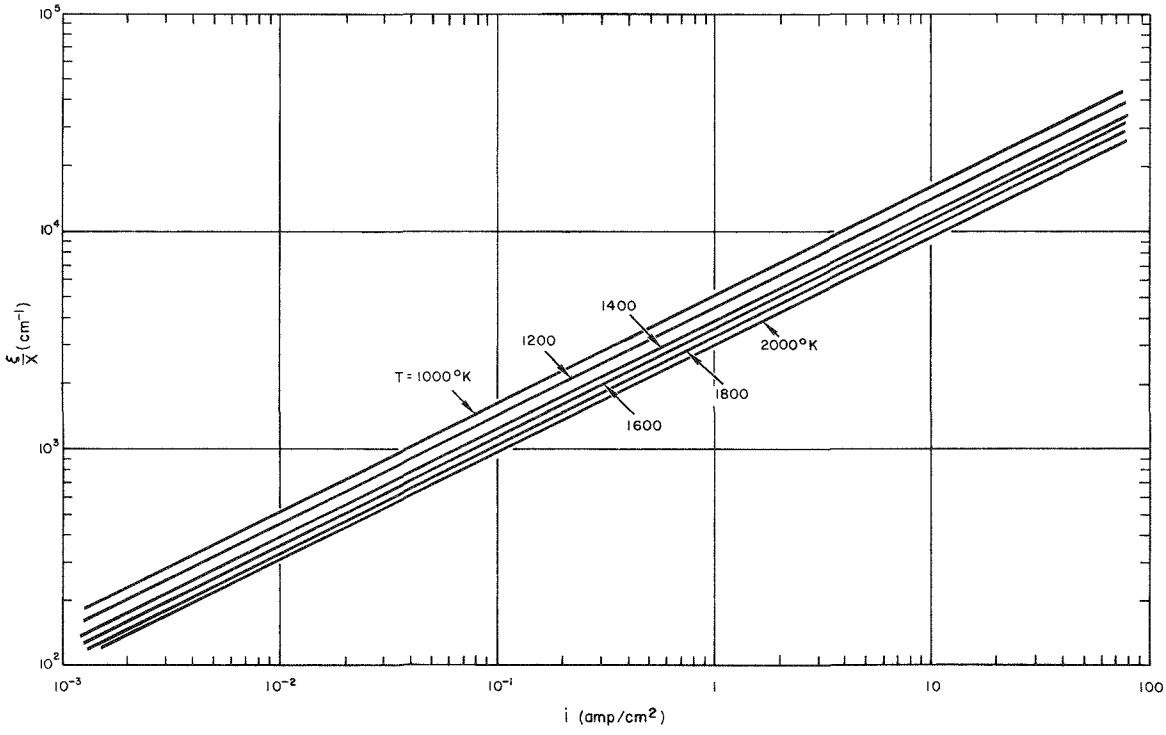

Figure 4. Plot of $\frac{\xi}{X}$ vs Electron Current i for Various Temperatures

densities at the emitter surface of ions and electrons coming <u>from</u> the emitter surface.

$$\beta = \frac{n+}{n-} = \sqrt{\frac{m+}{m-}} \cdot \frac{J+}{J-} \qquad \ldots (7)$$

The quantities m+ and m- are the ion and electron masses and J+ and J- are the current densities of the <u>emitted</u> ions and electrons respectively. In these equations and in the results which follow the definition of η is equivalent to that given by Langmuir, Equation 2. Likewise, ξ is defined in terms of the <u>emitted</u> electron current

$$\xi = 4 \frac{\pi}{2kT}^{3/4} m^{1/4} \left[e \cdot i_{-}(\xi=0) \right]^{1/2} x \qquad \ldots (8)$$

For convenience in applying the results of this discussion Equation 8 is plotted in Figure 4. The boundary conditions for the desired solutions are:

$$\left.\frac{d\eta}{d\xi}\right|_{\xi=\xi_L} = 0 \qquad \eta_L<0 \quad \text{retarding field case} \qquad \ldots (9)$$

$$\left.\frac{d\eta}{d\xi}\right|_{\xi=0} = 0 \qquad \eta_L>0 \quad \text{saturated emission case} \qquad \ldots (10)$$

where $\eta(\xi_L) = \eta_L$.

Only monotonic solutions have been studied and time and stability have not been considered. The solution of Equations 5 and 6, reduced to a plot of η_L vs. ξ_L for various values of β is shown in Figures 5a and 5b. The dependence of ξ_L on current is on the actual emitted current rather than the net diode current, ξ, used in Figure 1. The two currents are related by

$$\xi_L = \xi \qquad \eta_L>0 \qquad \ldots (11)$$

$$\xi_L = \xi e^{\eta_L/2} \qquad \eta_L<0 \qquad \ldots (12)$$

The $\beta=0$ curves correspond to the curves of Figure 1. The shaded region in Figures 5a and 5b is the only region where $\beta>1$ is needed to remove the

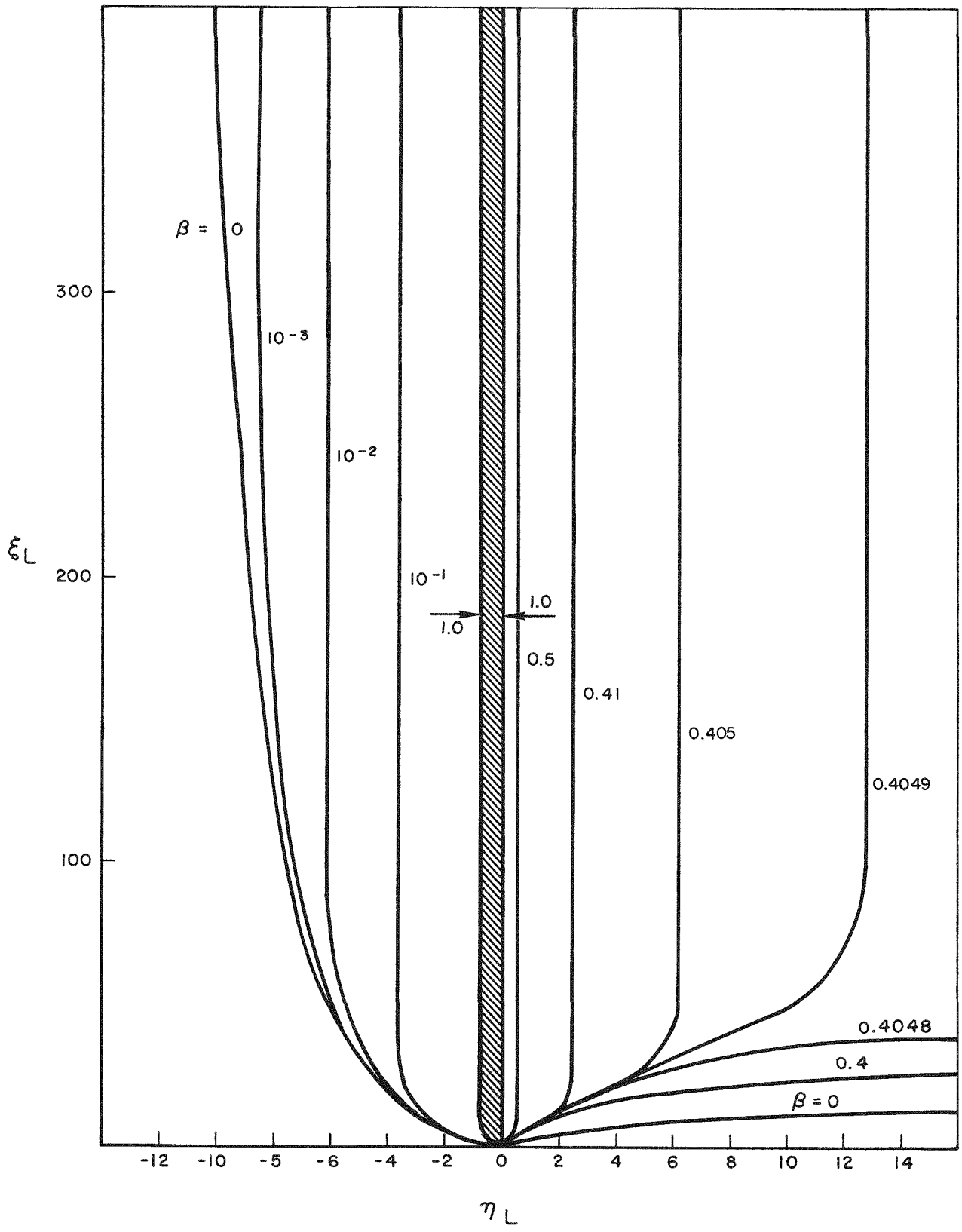

Figure 5a. 8 Emission Requirements for Removal of Space Charge Barriers (ξ_L = 0 to 400)

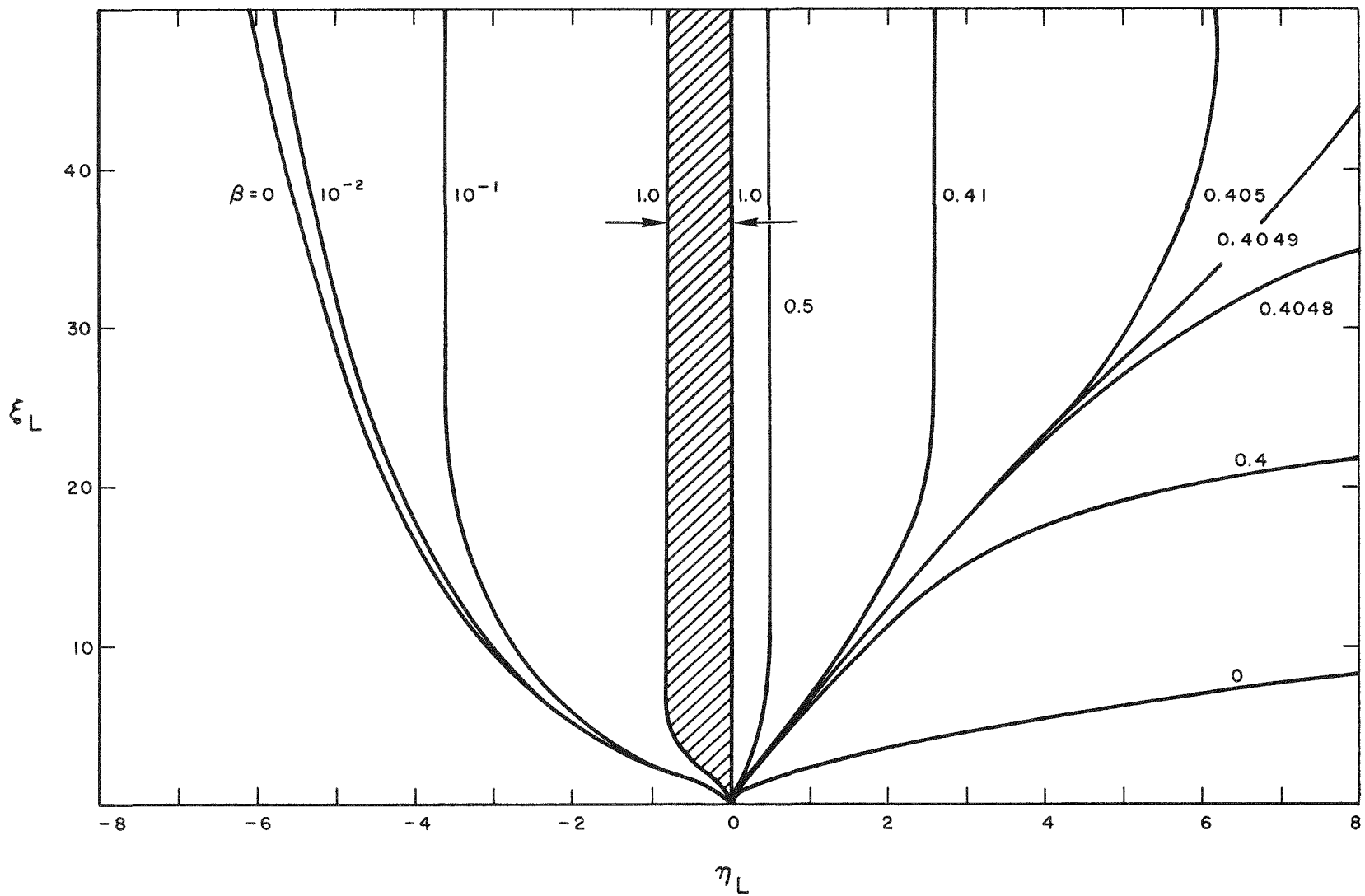

Figure 5b. β Emission Requirements for Removal of Space Charge Barriers (ξ_L = 0 to 50)

space charge barrier. At $\eta_L \sim -0.2$ and for large ξ_L the value rises to a maximum of $\beta=1.27$. For a specific β value in Figures 5a and 5b, η-ξ space is again divided into three regions corresponding to the three modes of diode operation as in Figure 1. It can be seen, however, that as β increased from zero the region of space charge limitation diminishes and eventually disappears.

Some potential distributions corresponding to the parameters specified in Figures 5a and 5b are shown in Figure 6. ($\eta_L = \pm 6$) It will be seen that for $\eta_L<0$ as β increases from zero, eventually a value is reached where not only the first derivative but also the second is zero at the collector. Let us designate the value of ξ_L when this occurs as h, $h=h(\eta_L,\beta)$. It is evident that the potential distribution for $\xi \leq h$ is independent of ξ_L as long as $\xi_L \geq h$. Under these restrictions, variation of ξ_L merely lengthens or shortens a collector plasma column. For large ξ_L, therefore, η_L and β become independent of ξ_L and related only to each other. This asymptotic relationship is

$$\frac{1}{\beta} = e^{-2\eta_L} \left(1-\mathrm{erf}\sqrt{-\eta_L}\right) \qquad \ldots (13)$$

and is plotted in Figure 7. In a similar manner, one finds that for $\eta_L>0$, as β increases from zero, a value of β is reached where the potential distribution develops two inflections and then, with very small changes in β, ξ_L goes to infinity developing a plasma column which is isolated from both emitter and collector. In this asymptotic case the β corresponding to a particular η_L is given by the minimum of the following function of η.

$$\frac{G(\eta)-1}{2\{1-e^{-\eta}\} - 2e^{-\eta}\{G(\eta_L) - G(\eta_L-\eta)\}} \qquad 0<\eta<\eta_L \qquad \ldots (14)$$

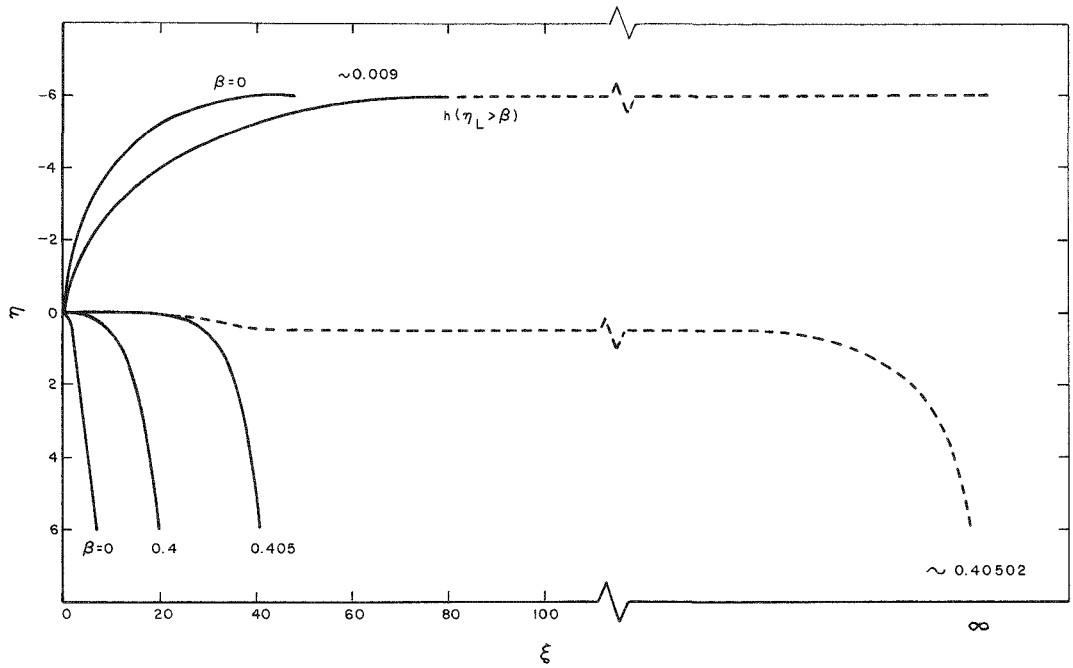

Figure 6. Potential Distributions with Zero Collector or Zero Emitter Field

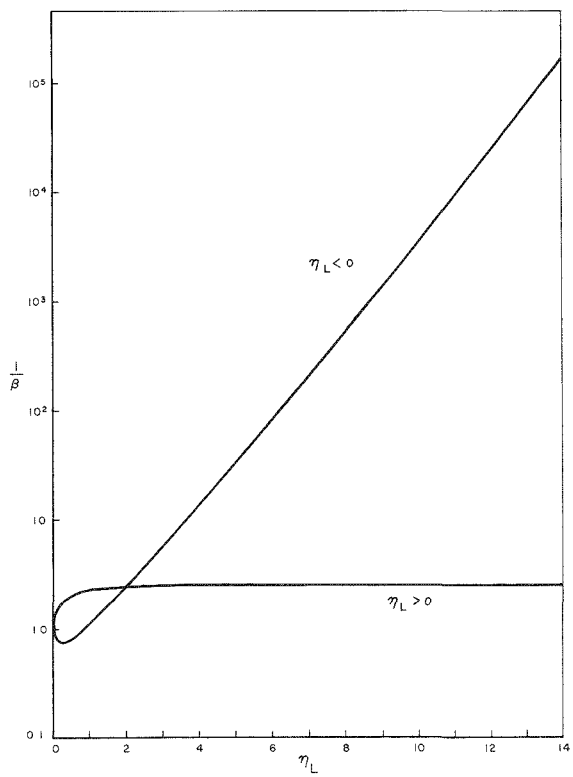

Figure 7. Asymptotic β Values

where

$$G(\eta) = e^{\eta}(1-\mathrm{erf}\sqrt{\eta}\ ) + \frac{2}{\sqrt{\pi}}\sqrt{\eta} \qquad \ldots (15)$$

The value of η for which the minimum occurs is the potential of the plasma in the asymptotic potential distribution. It is zero for $\eta_L=0$ and approaches 0.34 as η_L becomes very large. The asymptotic function, $\beta(\eta_L)$ from Equation 14, is also plotted in Figure 7. The physical significance of these asymptotic values is simple to understand. In retarding field operation the electron current reaching the collector is diminished from that emitted by a factor $e^{-\eta_L}$. The ion emission requirements for neutralization at the collector are therefore diminished accordingly since all emitted ions are accelerated to the collector. In saturated emission operation ion emission requirements for removal of space charge barriers at the emitter are about half that needed for neutral emission. This is understandable since emitted ions are reflected in the interelectrode space and return to contribute again to neutralization at the emitter. A value of $\beta=0.5$ is not obtained since complete neutralization is not needed for removal of the space charge barrier. Since most of the ions will be reflected when the potential, V, across the diode is such that $eV \approx kT$ this asymptotic value will be essentially reached for $\eta=1$. This effect can be seen in Figure 7.

The curves of Figure 3 can be placed in the coordinate system of Figures 5a and 5b by using the following transformation

$$\xi_L = \xi e^{\eta_B/2} \qquad \ldots (16)$$

In Figure 8 this transformation is shown for the same coordinate range of Figure 5a. Figure 8 shows that for a given spacing and electron emission (ξ=const.) the space charge barrier (η_A for $\eta_L<0$ and η_B for $\eta_L>0$) varies rapidly with η_L for $\eta_L<0$ and slowly with η_L for $\eta_L>0$. In Figure 5a it can be seen that the ion requirement, β, as a function of η_L, varies slowly for

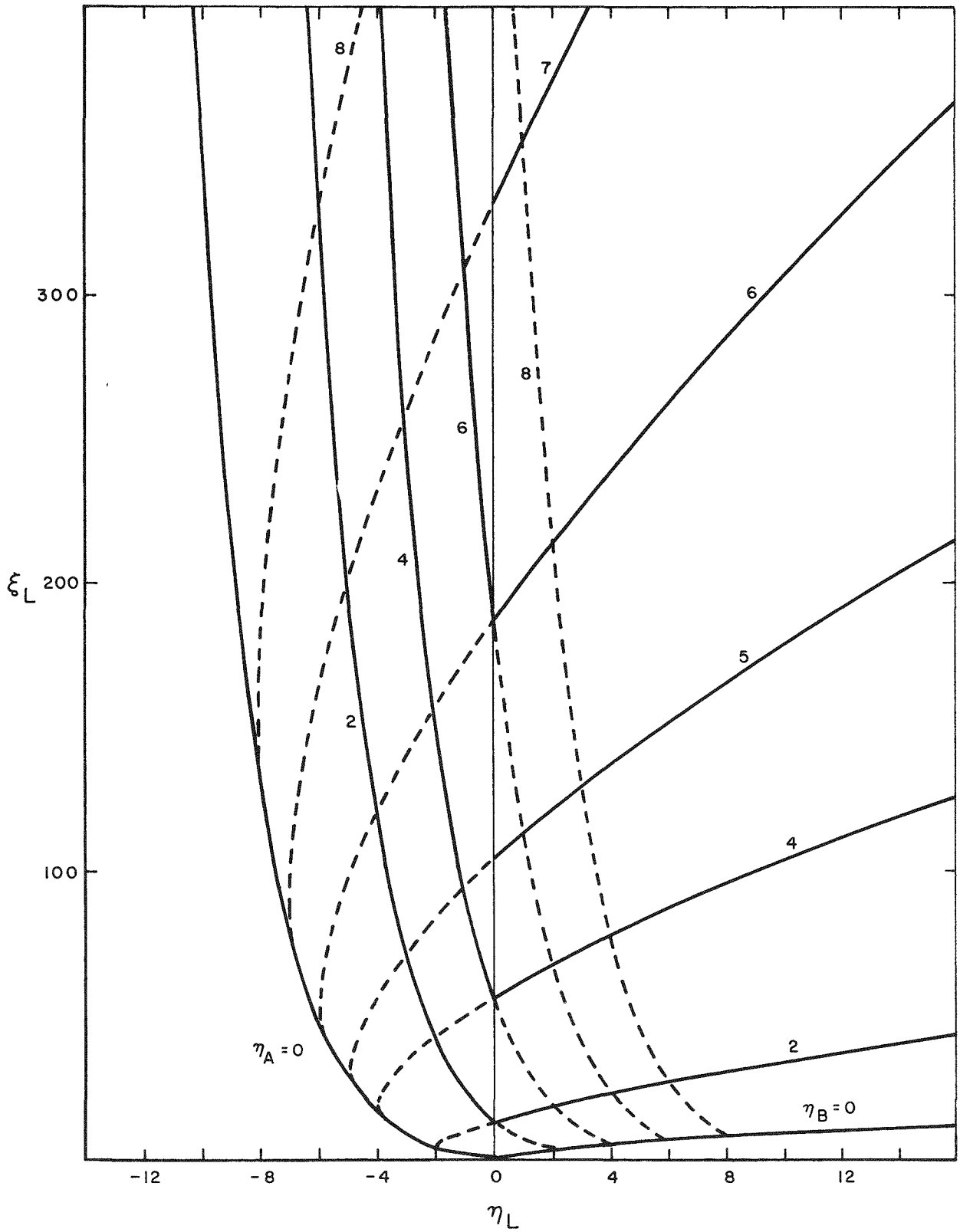

Figure 8. Magnitude of Space Charge Barriers
(η_A and η_B Defined in Figure 2)

$\eta_L > 0$ where the space charge barrier varies slowly with η_L and varies rapidly for $\eta_L < 0$ where the space charge barrier varies rapidly with η_L.

REFERENCES

1. W. Schottky, Verh. dtsh. physik Ges. 16, 490 (1914) (Referred to in G. Herrmann & S. Wagener, The Oxide-Coated Cathode vol. 2 London, Chapman & Hall 1951)
2. G.H. Moller & F. Detels, Jb. d. drahtl. Telegr. u. Teleph., 27 74 (1926) (Referred to in G. Herrmann & S. Wagener, op. cit.)
3. W.B. Nottingham,"Thermionic Emission", Handbuch der Physik (vol. 21, S. Flugge ed. Springer, 1956) p 43
4. C.H. Child, Phys. Rev. 32, 498 (1911)
5. I. Langmuir, Phys. Rev. 2, 450 (1913)
6. W.R. Ferris, RCA Review, 10, 134 (1949)
7. I. Langmuir, Phys. Rev. 21, 419 (1923)
8. H. Poritsky, IRE Trans. PGED 1, 60 (1953)
9. P.H.J.A. Kleynen, Philips Res. Rep. 1, 81 (1946)
10. See references associated with preceding section, p 43

VI. UNIGNITED MODE OF THERMIONIC CONVERTERS

L. K. Hansen and H. Hori

INTRODUCTION

The volt-ampere characteristics of thermionic converters in the unignited mode are sensitive to changes in emitter temperature, cesium pressure and spacing. The dependence of the characteristic on these parameters has been measured in order to study some of the basic processes occurring in thermionic converters. It is recognized that a converter operating in the unignited mode is far from optimized with respect to either power output or efficiency; however, in this "off-optimum" mode the processes in thermionic converters produce detailed structure in the volt-ampere characteristics. Therefore, the detailed structure and the trends in this structure can be used to identify and formalize such basic converter phenomena as potential distributions, ion emission, mean free paths, patch effects, and ionization processes. The advantage of using the unignited mode for this study is that volt-ampere characteristics are not complicated by the additional mechanisms which produce anomalously high current densities in the ignited mode.

APPARATUS

The converter used to obtain the volt-ampere characteristics which follow was a variable spacing, plane parallel diode with molybdenum electrodes,* as shown in Figures 1 and 2. The area of the plane surfaces of the electrodes was 2.0 cm^2. Spacing between the electrodes, which was variable from zero to 0.125 in. by means of a differential screw assembly,

* This converter was constructed in another research program carried out under contract AT(11-1)-GEN-8 with the U.S. Atomic Energy Commission, (Reference 1).

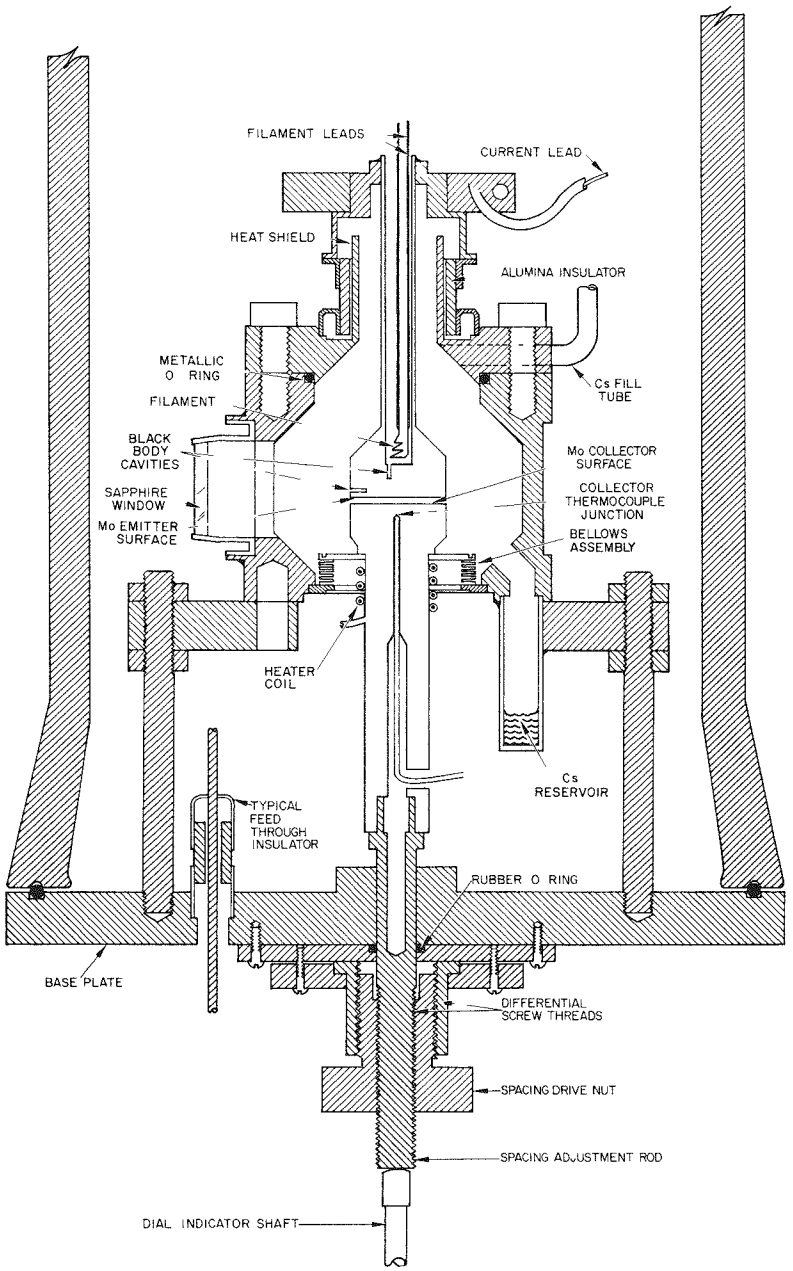

Figure 1. Variable-Spacing Converter

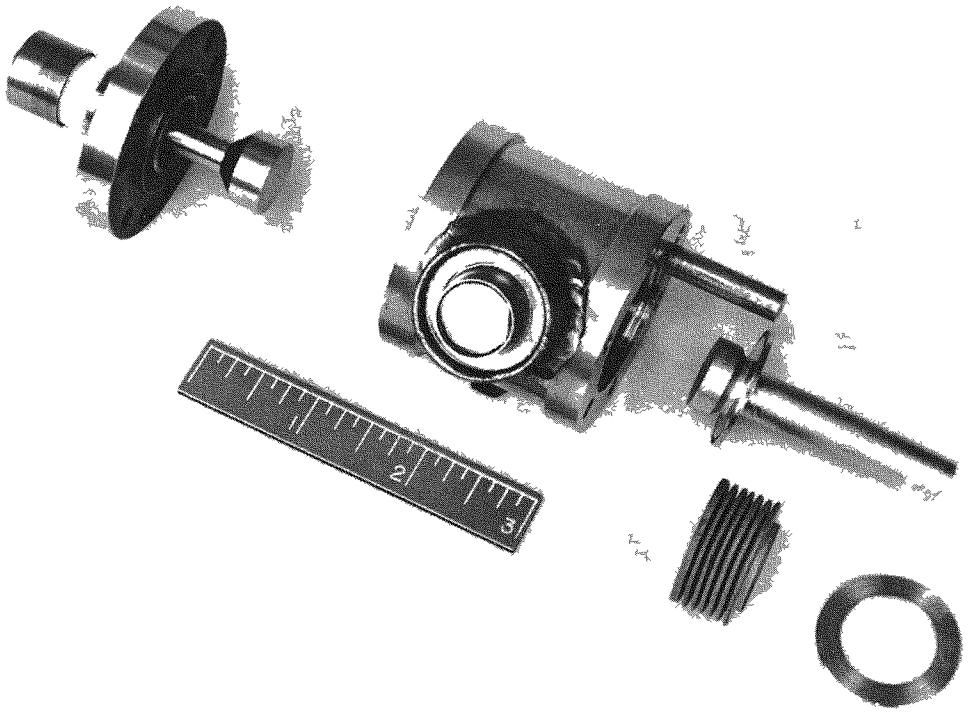

Figure 2. Exploded View of Variable-Spacing Converter

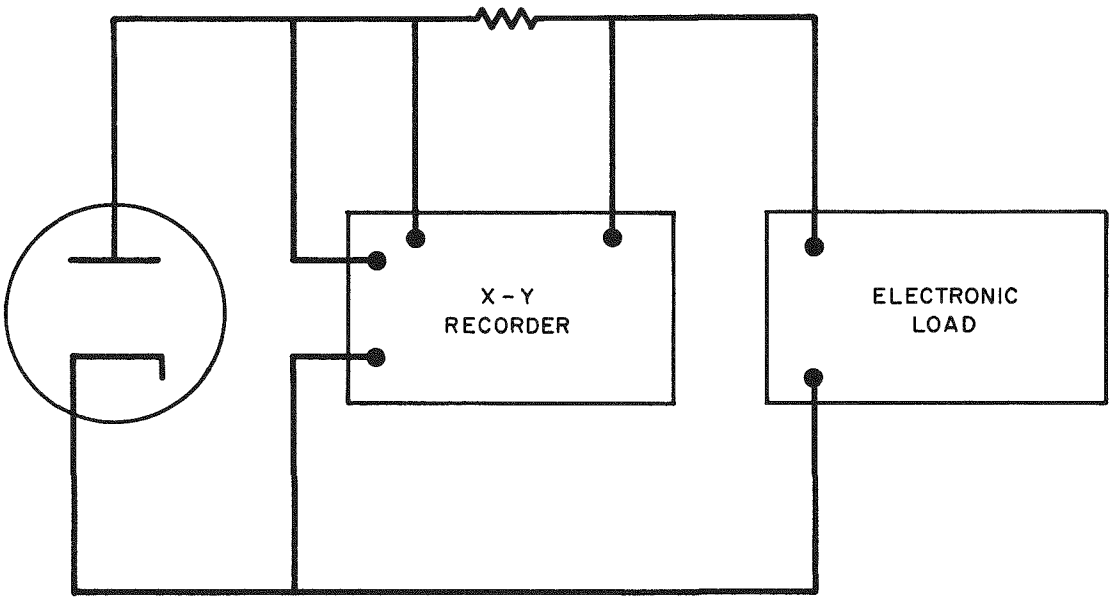

Figure 3. Circuit for Obtaining Converter Volt-Ampere Characteristics

was measured by means of an attached precision dial indicator. The electrode surfaces were adjusted with a precision jig to make them parallel within 0.0005 in. The collector was maintained at a constant temperature by the combined effect of an attached heater coil and an attached cooling tube. The latter was cooled by forced air. The temperature of the collector was measured with a thermocouple mounted within the collector. Visual appearances of the discharge could be determined through a sapphire window opposite the interelectrode space. The emitter temperature was measured with an optical pyrometer, sighting through the sapphire window and into a black body cavity at the side of the emitter. Several layers of molybdenum foil (not shown in Figure 1) were placed around the curved surfaces of the emitter to reduce radiation losses.

The circuit used to obtain the volt-ampere characteristics is shown in Figure 3. All characteristics were taken with an X-Y recorder. Sweep speeds were about one inch per second. The sweep was controlled manually by an adjustment in the transistorized, current-controlled load.

VOLT-AMPERE CHARACTERISTICS

The volt-ampere characteristics of the unignited mode are shown in Figures 4 to 9. These figures contain a large number of volt-ampere characteristics. Such an extensive coverage of the parameters concerned is very useful for identifying and studying some of the basic effects occurring in thermionic converters. For this reason they are included in this report. An attempt was made to develop a consistency in temperatures and scale factors so that the trends in the data could be easily determined. For various experimental reasons this did not always occur; however the necessary information is listed with the individual characteristics. The essential trends are relatively easy to follow. The origins for these

Figure 4a. Unignited Mode for Spacing L = 5 mils

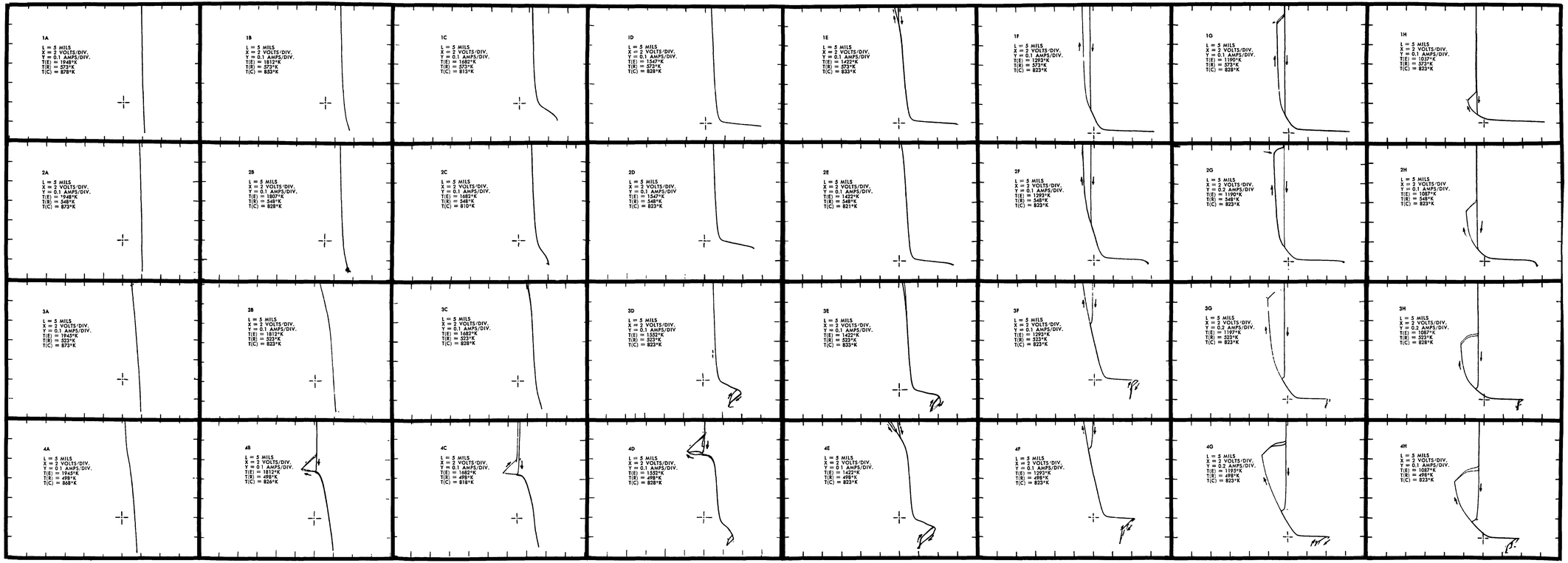

LEGEND:
T(E) = Emitter Temperature
T(R) = Cesium Reservoir Temperature
T(C) = Collector Temperature

Figure 4b. Unignited Mode for Spacing L = 5 mils

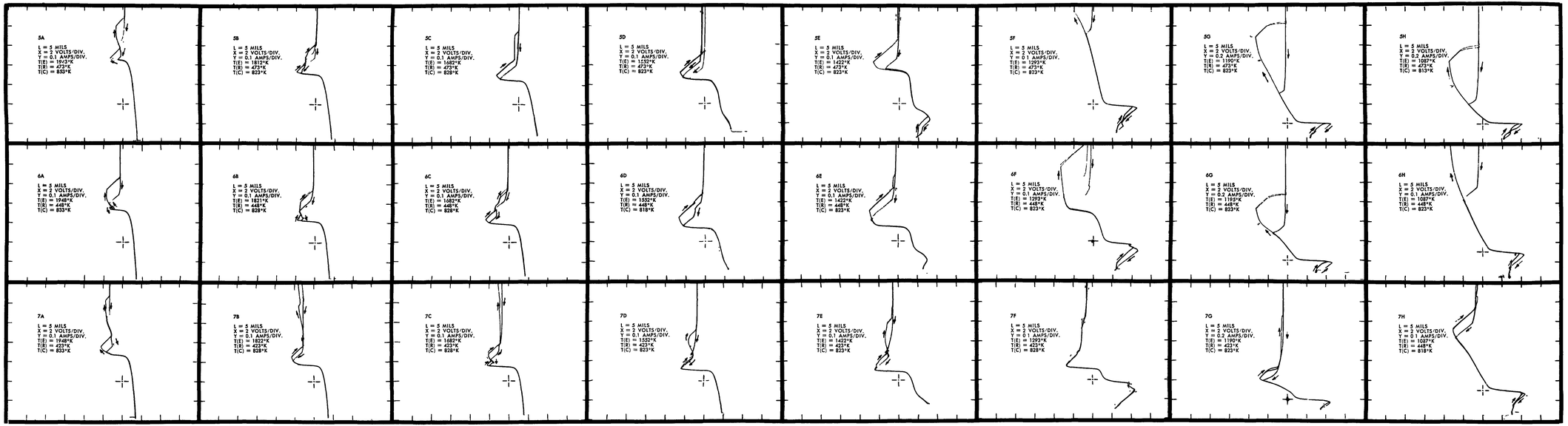

LEGEND:
T(E) = Emitter Temperature
T(R) = Cesium Reservoir Temperature
T(C) = Collector Temperature

Figure 5a. Unignited Mode for Spacing L = 10 mils

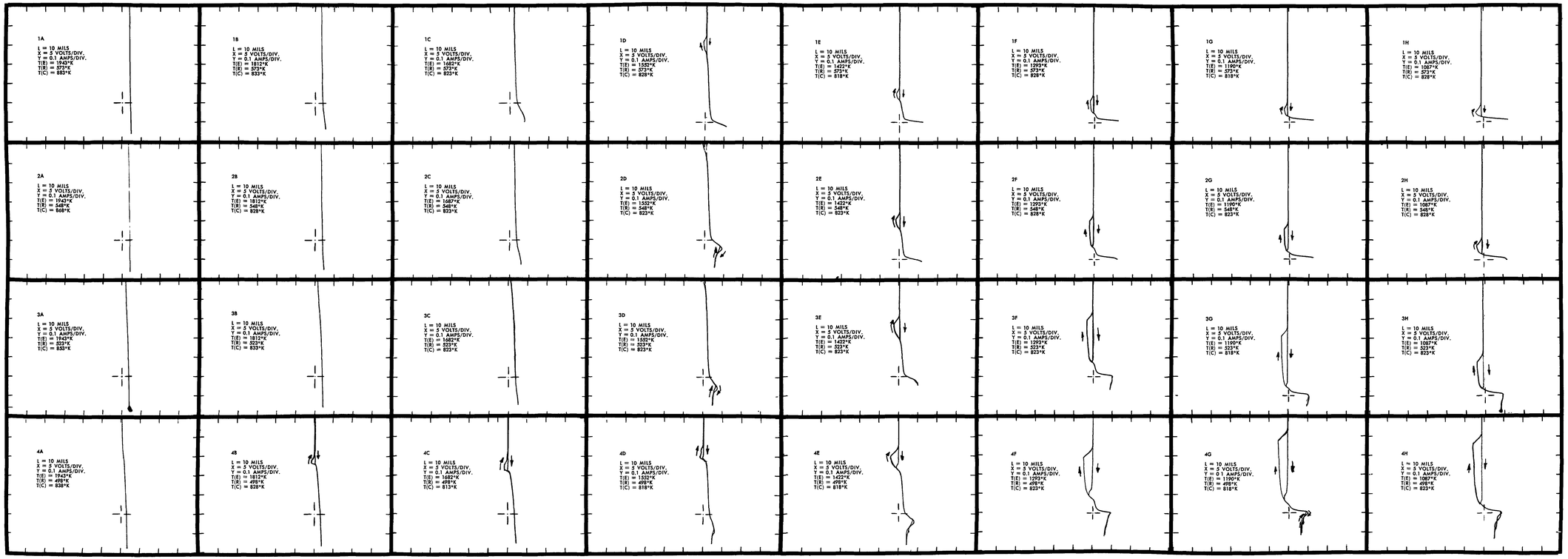

LEGEND:
T(E) = Emitter Temperature
T(R) = Cesium Reservoir Temperature
T(C) = Collector Temperature

Figure 5b. Unignited Mode for Spacing L = 10 mils

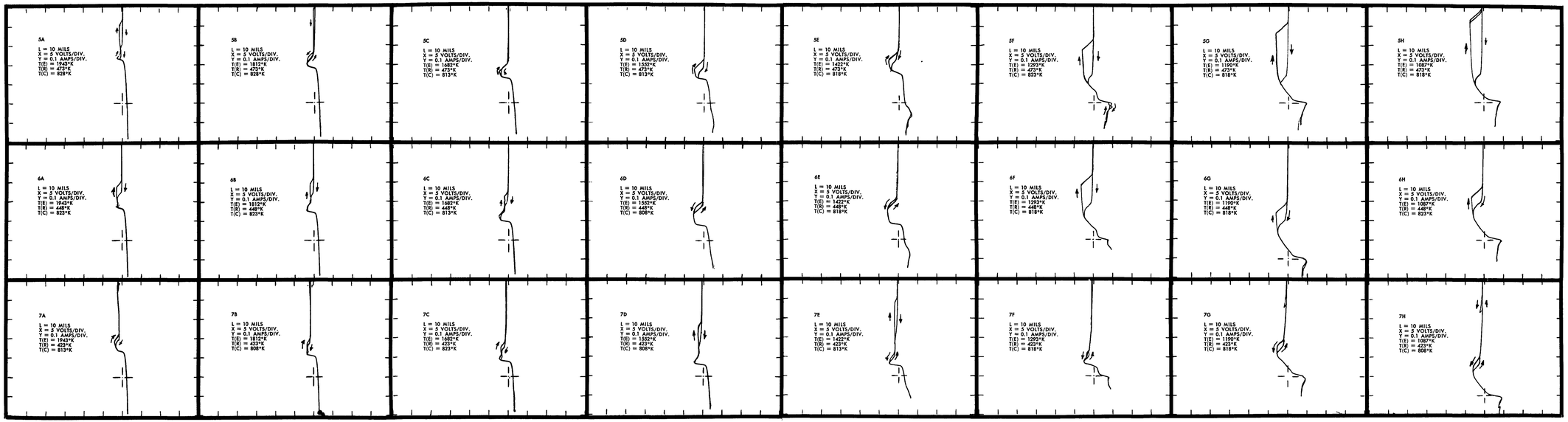

LEGEND:
T(E) = Emitter Temperature
T(R) = Cesium Reservoir Temperature
T(C) = Collector Temperature

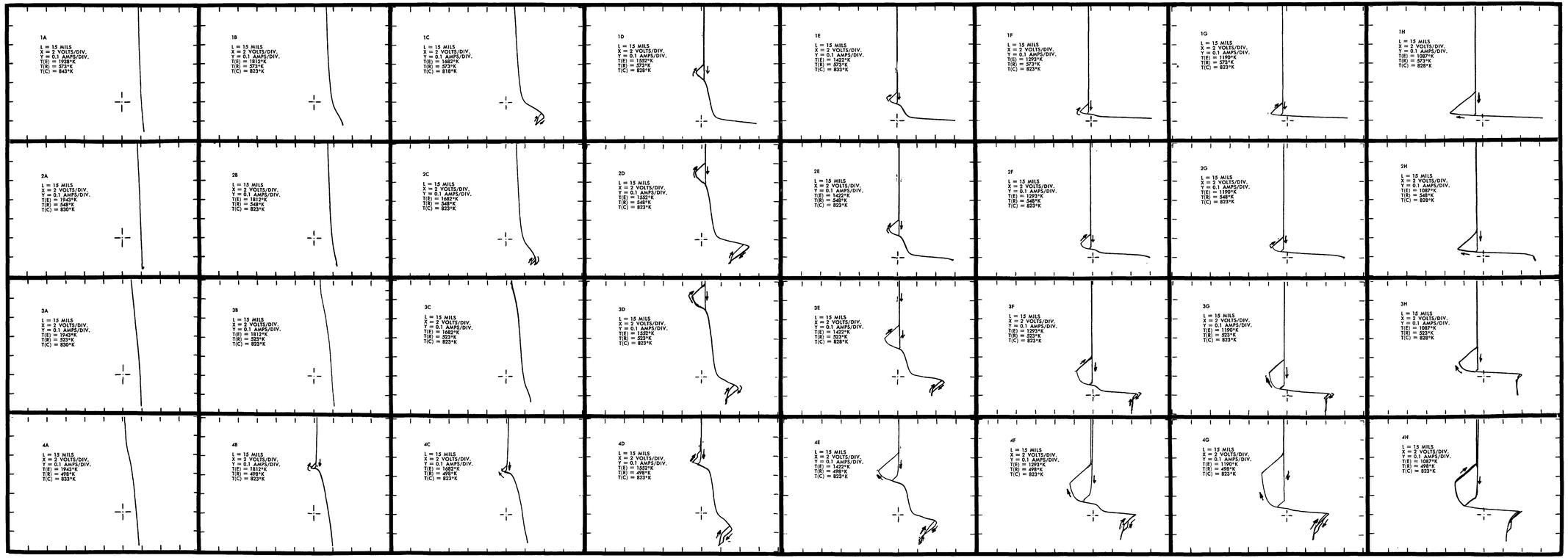

Figure 6a. Unignited Mode for Spacing L = 15 mils

LEGEND:
T(E) = Emitter Temperature
T(R) = Cesium Reservoir Temperature
T(C) = Collector Temperature

Figure 6b. Unignited Mode for Spacing L = 15 mils

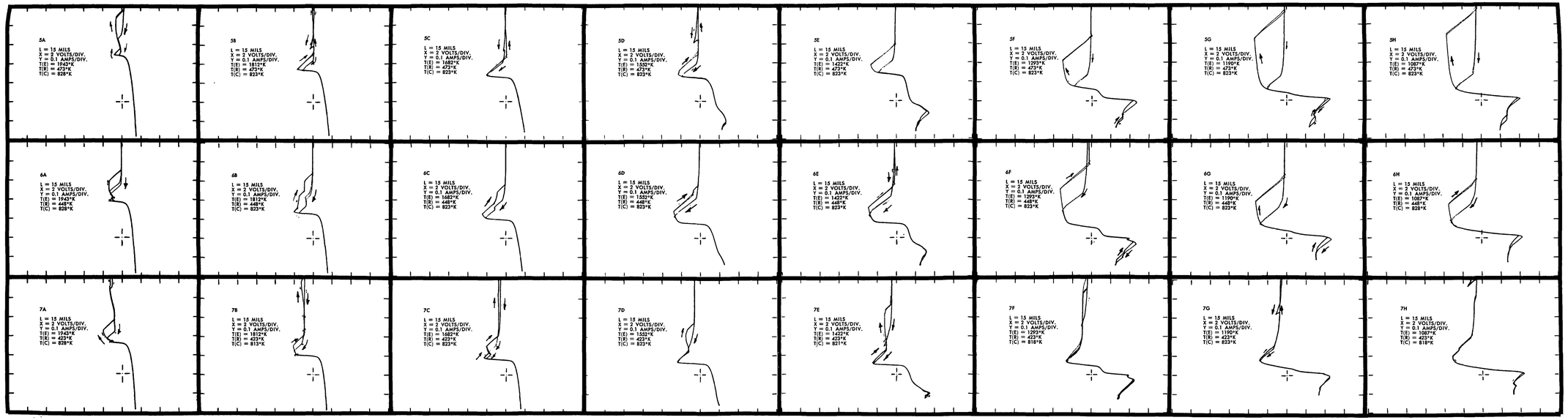

LEGEND:
T(E) = Emitter Temperature
T(R) = Cesium Reservoir Temperature
T(C) = Collector Temperature

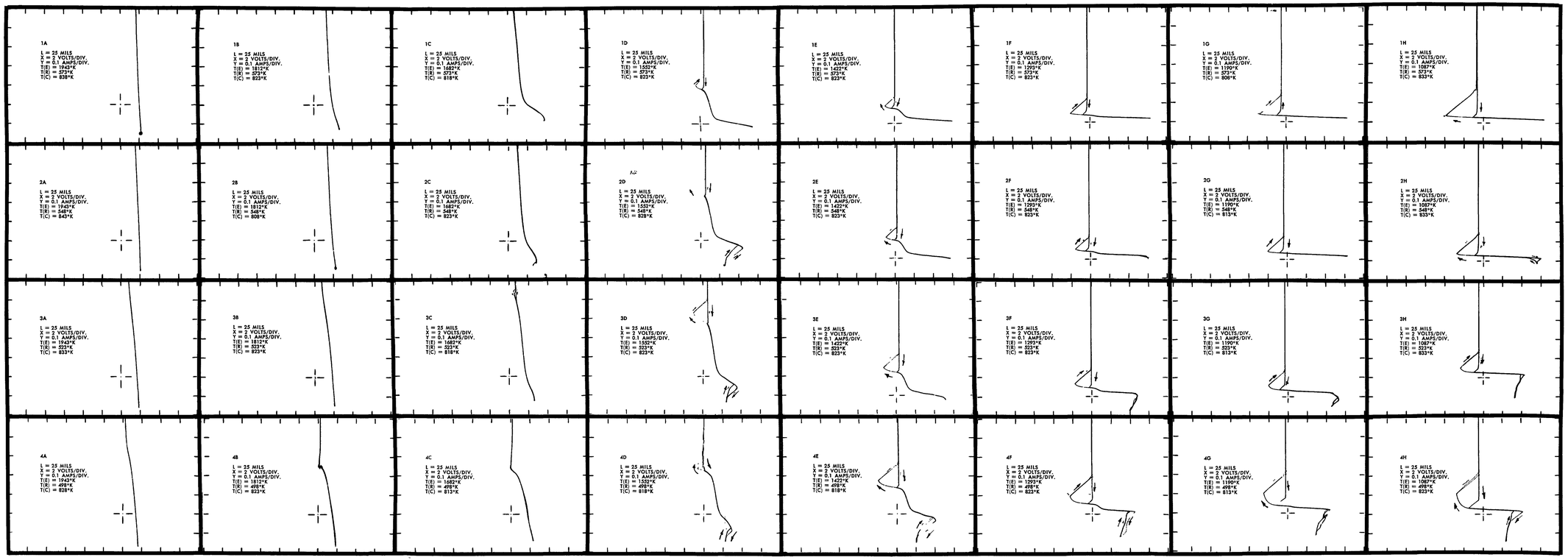

Figure 7a. Unignited Mode for Spacing L = 25 mils

LEGEND:
T(E) = Emitter Temperature
T(R) = Cesium Reservoir Temperature
T(C) = Collector Temperature

AI-7979

Figure 7b. Unignited Mode for Spacing L = 25 mils

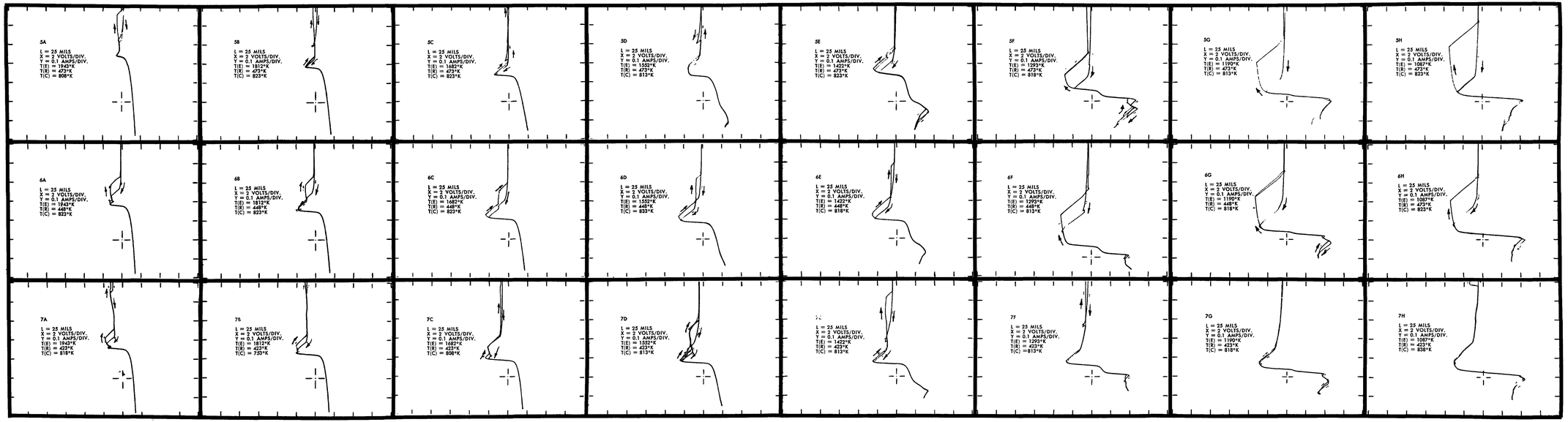

LEGEND:
T(E) = Emitter Temperature
T(R) = Cesium Reservoir Temperature
T(C) = Collector Temperature

Figure 8a. Unignited Mode for Spacing L = 50 mils

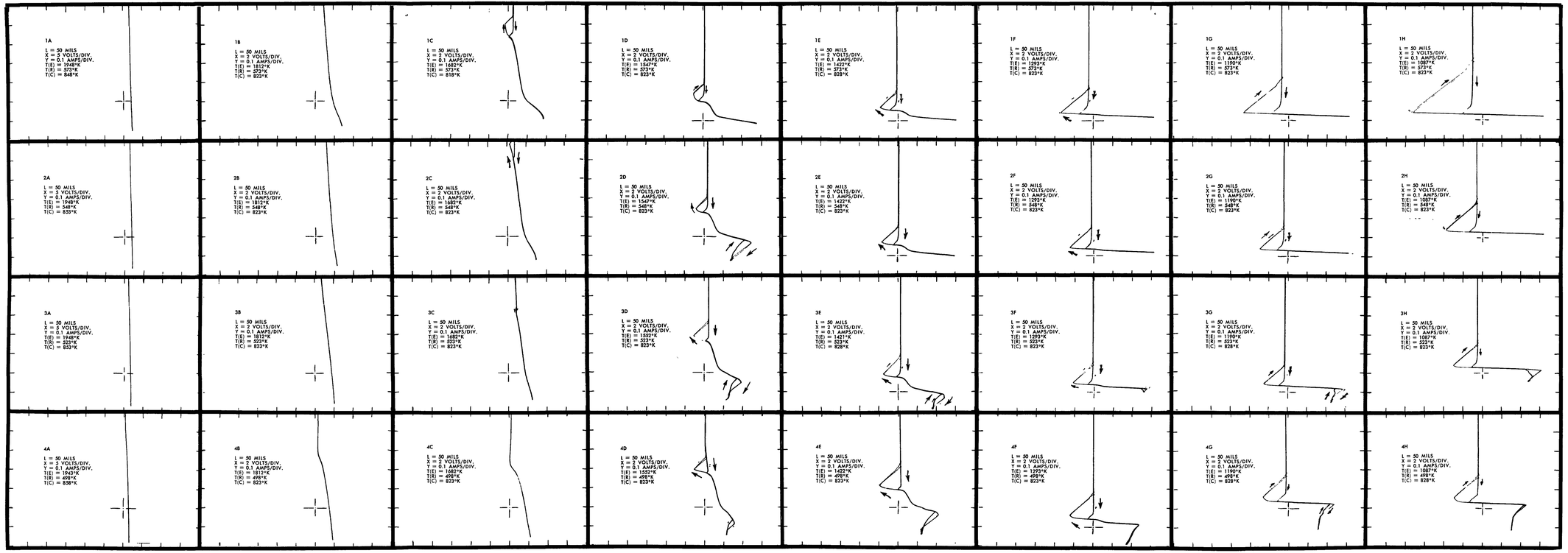

LEGEND:
T(E) = Emitter Temperature
T(R) = Cesium Reservoir Temperature
T(C) = Collector Temperature

AI-7979

Figure 8b. Unignited Mode for Spacing L = 50 mils

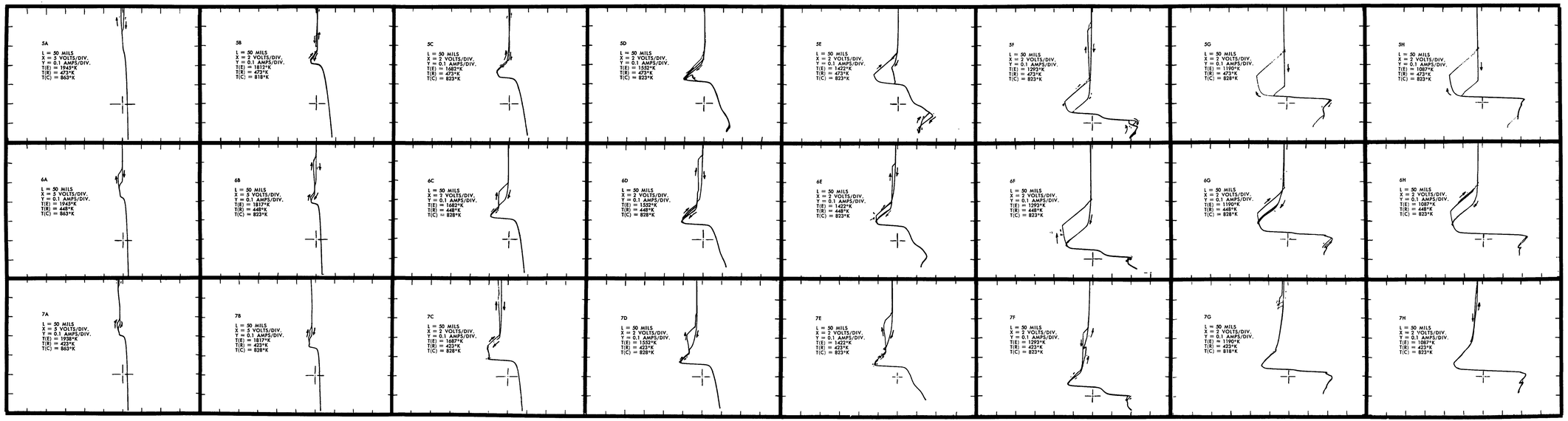

LEGEND:
T(E) = Emitter Temperature
T(R) = Cesium Reservoir Temperature
T(C) = Collector Temperature

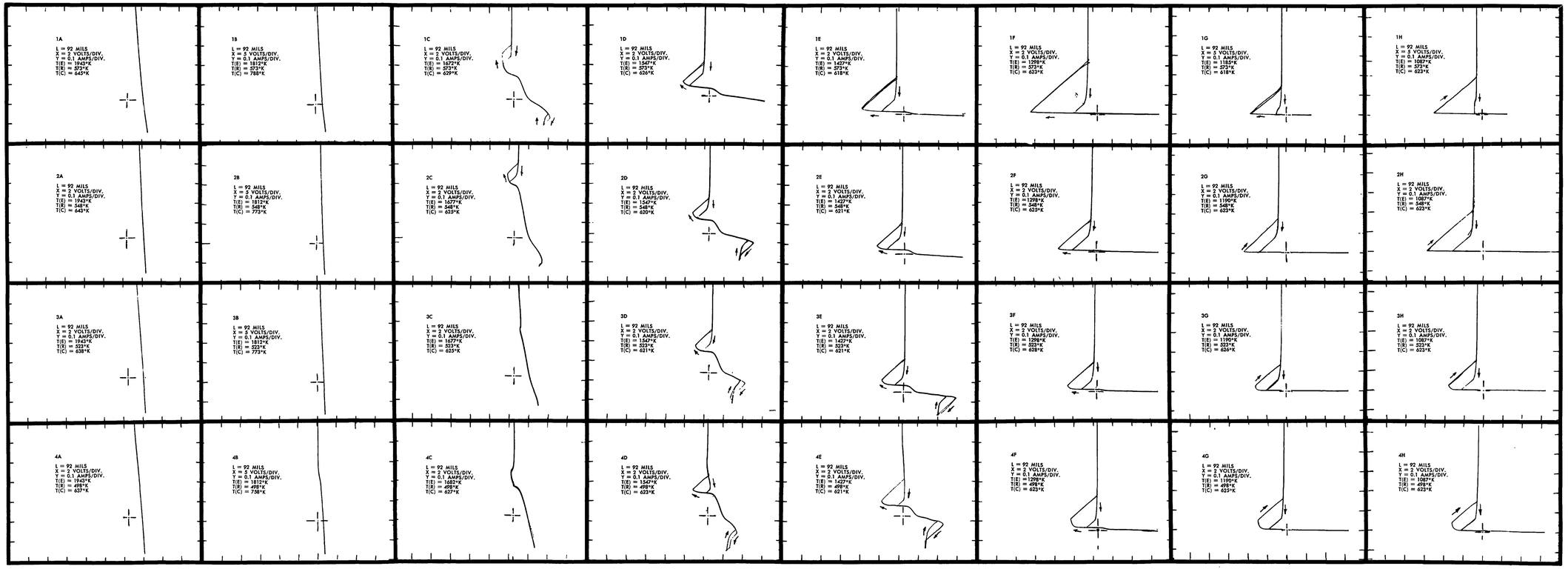

Figure 9a. Unignited Mode for Spacing L = 92 mils

LEGEND:
T(E) = Emitter Temperature
T(R) = Cesium Reservoir Temperature
T(C) = Collector Temperature

AI-7979

Fibure 9b. Unignited Mode for Spacing L = 92 mils

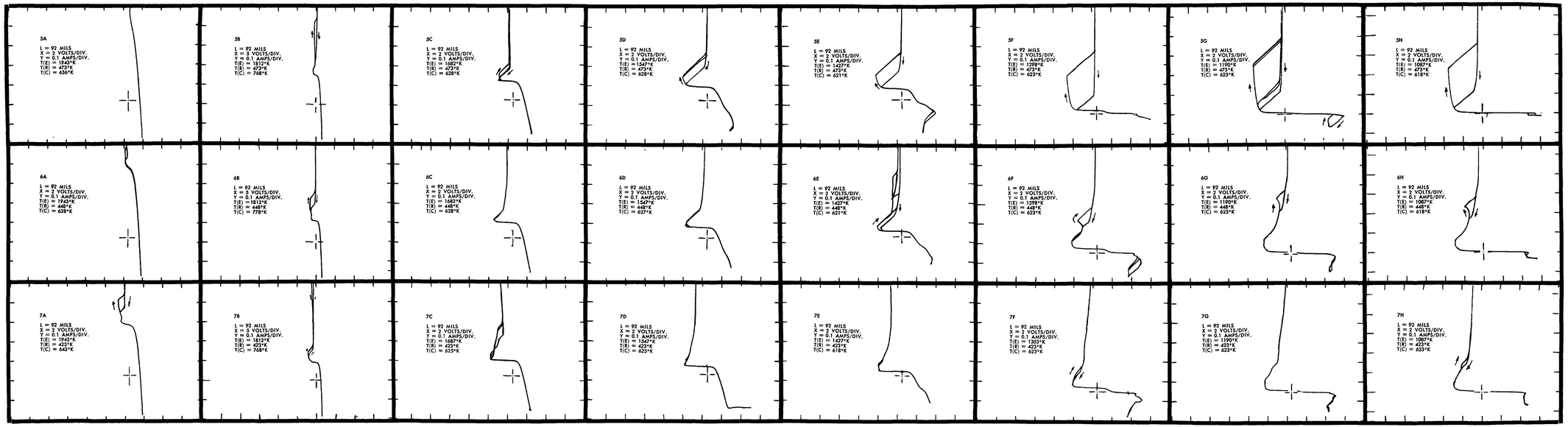

LEGEND:
T(E) = Emitter Temperature
T(R) = Cesium Reservoir Temperature
T(C) = Collector Temperature

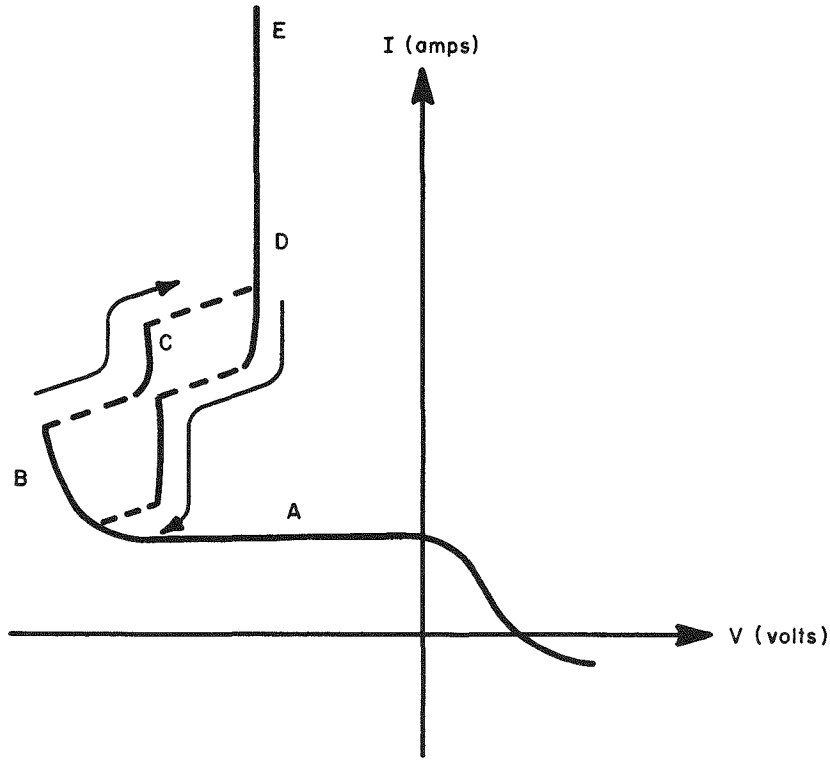

Figure 10. A Typical Volt-Ampere Characteristic

characteristics were obtained by temporarily shorting the inputs of the X-Y recorder.

VISUAL APPEARANCES

The visual appearance of the discharge is closely correlated to the position of the operating point on the volt-ampere characteristic. A typical volt-ampere curve is shown in Figure 10. With a diode operating in region A of the characteristic, either when there is an apparent saturation current as shown in Figure 10 or no current at all, there appears to be no radiation coming from the interelectrode space. In region B a sheet of glow appears on the surface of the collector, increasing the brightness as the current increases. When a stable region C exists, a ball of glow appears at the edge of the interelectrode space, protruding out into the surrounding volume. At region D a small ball of glow appears, usually at the center of the electrodes. As the current is increased the ball widens to fill the interelectrode space. For large spacings this ball appears somewhat as a hemispherical shape resting on the collector. Sometimes the ball will have bright columns in it about 1 mm in diameter, running perpendicular to the electrodes. As current is increased the columns have been noticed to increase in number. The electrodes are polycrystalline, therefore, this is presumably a direct observation of a patch effect.

INTERPRETATION

A discussion of these volt-ampere characteristics for the unignited mode is presented in Section VII.

REFERENCE

1. N. S. Rasor and C. C. Weeks, "Thermionic Converters for Compact Nuclear Power Plants," Atomics International Report NAA-SR-7144 (1962)

VII. INTERPRETATION OF VOLT-AMPERE CHARACTERISTICS

C. Warner, III and L. K. Hansen

INTRODUCTION

Only a small portion of converter volt-ampere characteristics can be used for efficient energy conversion. The entire characteristic is useful, however, as a tool for analyzing the basic processes occurring in thermionic converters. An understanding of these processes is needed at the present time to assist in evaluating the efficiency limitations in existing converters and to guide further developments in thermionic energy conversion.

In the discussion which follows several interesting features of converter operation are examined, particularly the features of the unignited mode. Converters operating in this mode pass currents which may be either temperature limited, space charge limited, collector voltage limited, or diffusion limited. In addition, ions may be generated thermally at the emitter surface, by collisions in the collector sheath, or by collisions in the interelectrode space. All of these conditions have their particular effect on the volt-ampere characteristics. An analysis of the characteristics therefore leads to an insight into these basic phenomena as they occur in thermionic converters. Analysis of the unignited mode leads also to understanding of the ignited mode because in the unignited mode phenomena associated with ignition can be studied at their inception.

Long before thermionic converters became of interest for energy conversion this same type of discharge was studied extensively and was referred to as the low voltage arc or the externally heated hot cathode arc. Some of this work is related to the following discussion of converter characteristics and therefore is reviewed, particularly as it related to the unignited mode of thermionic converters and the transition to the ignited mode.

REVIEW OF RELATED PHENOMENA IN GASEOUS DISCHARGES

Discharges in general have what one might refer to as ignited and unignited modes. Ignition occurs whenever the increasing current of a discharge introduces a new phenomena which in turn increases the efficiency of the discharge. Since the increase in efficiency results in further increase in the current, a positive feedback develops which drives the discharge into an ignited mode. The effect of the increase in efficiency is not only increased current, but also a reduction in the applied voltage required to sustain the discharge.

In the Townsend discharge, for example, positive feedback occurs when the ionization level is sufficient to develop a sheath with dimensions of the order of the interelectrode space, for then ion production becomes more efficient and there is a resulting increase in secondary electron production. The discharge therefore ignites becoming a glow discharge. On the other hand, with the glow discharge, when ion bombardment of the cathode heats the cathode to a point where thermionic emission supplements secondary electron emission or when sheaths develop which introduce field emission, another feedback develops which drives the discharge into arc operation. The volt-ampere characteristic associated with these ignitions are shown schematically in Figure 1.

Externally heated hot cathode discharges differ in several respects from the above discharges. In the ignited or arc mode a very striking difference is that its maintenance potential can be lower than the ionization potential of the gas, a feature which attracted interest almost 50 years ago. Today, of course, thermionic energy conversion exists because the maintenance potential may be negative. An explanation for the ionization in this low voltage mode was first demonstrated by Compton and

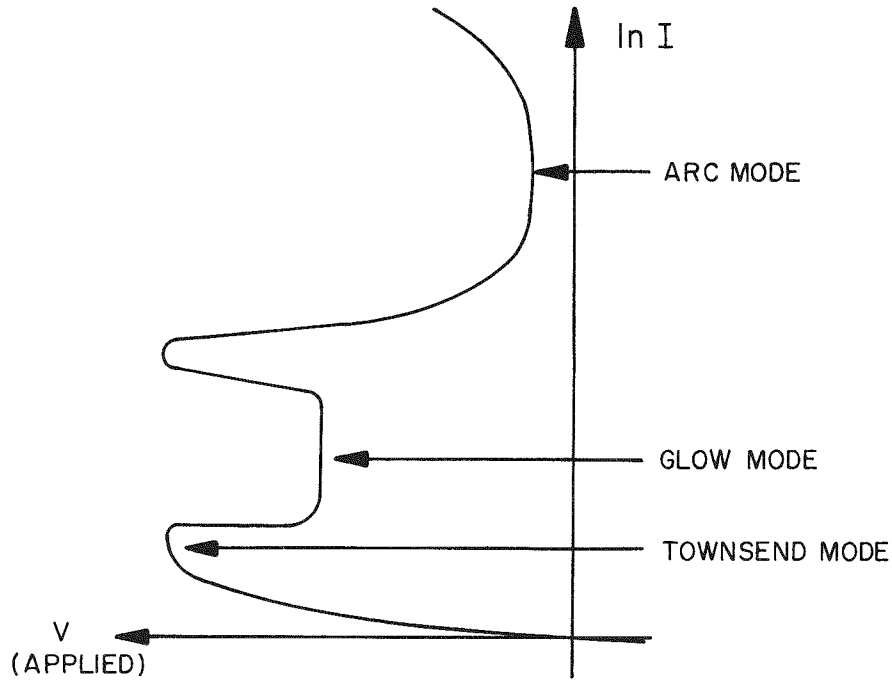

Figure 1. Volt-Ampere Characteristics for a "Cold" Electrode Discharge

Eckart[1] when they showed the existence of a virtual anode or high potential region in the interelectrode space. Electrons would tend to neutralize such a region; however, Druyvesteyn[2] proposed an electron-electron collision mechanism by which neutralization of this virtual anode could be prevented. Johnson[3] has given an extensive study of these effects. More recently this ignited mode has been studied by a great number of people for the case of cesium in thermionic converters.

For the discussion which follows, previous work with the unignited mode of externally heated hot cathode discharges is of special interest. The unignited mode of these discharges can be expected to differ greatly from the unignited modes of discharges without externally heated cathodes because thermionic electrons are available to the discharge, and therefore the effects of secondary electrons are suppressed. Many of the features of

the unignited mode presented in Section VI of this report have been observed in earlier work with gases other than cesium. The anode glow mode, for example, has been known for many years. An extensive study of this mode has been made by Malter, Johnson and Webster[4-6] for noble gases in cylindrical diodes. Daly and Emeleus[7] used mercury vapor in cylindrical diodes and obtained similar results. A planar system with argon used by Cairns and McCullagh[8] also showed an anode glow mode. The intermediate or first ignited mode shown by region C of Figure 10 in Section VI (p 74) has also been observed previously. Both Daly and Emeleus and Pengelly and Wright[9] have examined this feature. The apparent saturation of the current in the unignited mode was reported by Cairns and McCullagh and, much earlier, by Duffendack[10] using hydrogen. Some of the results of Section VI are at variance with the works referred to above. For example, Cairns and McCullagh report that the anode glow mode occurs when the diode current is increasing to the apparent saturation level, but, as shown in Figure 10 of Section VI, the present work indicated that the anode glow mode occurred (when there was also an apparent saturation current) when the current increased abruptly above the apparent saturation level. Daly and Emeleus[7] also ascribe the cause of their first ignited mode to the voltage drop along their cathode. They do, however, mention that similar results were obtained by Pengelly and Wright for nearly equipotential cathodes. In the present work, no voltage drops existed across the cathode; therefore, the characteristics of the first ignited mode do not appear to be related to cathode voltage drops. This mode, in which the glow positions itself at the edges of the interelectrode space, evidently occurs because the increased electron path at the electrode edges allows the discharge to ignite at a lower current than would be required for ignition in the interelectrode space.

The characteristics of Section VI show that this mode occurs only for low cesium pressures where the extra path length is essential. Such an effect is common in other types of discharges.

As yet the unignited mode in thermionic converters has not been studied extensively. Houston and Gibbons[11-12] however, have measured some trends in this mode for the case where there are many mean free paths in the inter-electrode separation and have concluded that the apparent saturation current is space charge limited.

INTERPRETATION OF THE UNIGNITED MODE

Before the unignited mode volt-ampere characteristics contained in Section VI can be interpreted, several important parameters must be calculated for the ranges of emitter temperature (T_E) and cesium reservoir temperature (T_R) covered by the characteristics. First, it is important to know the work function (ϕ_E) and saturation electron current (J_s) for the molybdenum emitter as a function of T_E and T_R. This information has been reported by Houston[12] and Aamodt[13] and is plotted in Figure 2 for the temperature ranges of interest. In the preparation of this figure, some comparisons were made to the plots prepared by Nottingham.[14] Some curves of constant Debye length, h

$$h = 690 \sqrt{\frac{T}{10^4} \frac{1}{n_{-o}}} \text{ cm} \qquad \ldots (1)$$

where

$$n_{-o} = 4.02 \times 10^{13} \frac{J_s}{\sqrt{T_E}} \text{ cm}^{-3} \qquad \ldots (2)$$

have also been plotted in Figure 2. For convenience, the parameters T_E and T_R associated with the characteristics of Section VI are indicated on the figure by dots adjacent to the number-letter designation for the appropriate characteristic. It is also important to know the ratio, at the emitter, of

the ion to electron densities (β) for the emitted particles. Lines of constant β have been plotted in Figure 3. These lines are calculated from the work function information in Figure 2. Figure 3 also contains a plot of lines of constant electron mean free path, λ_e. Nottingham's[15] choice for the mean free path has been adopted here.

From Figures 2 and 3 several limiting cases can be identified which suggest appropriate analytical models for analyzing the volt-ampere characteristics. Figure 3, for example, indicates two limiting cases, where the mean free path is either large or small compared to the interelectrode spacing. In the latter case, the surface ionization mode of the volt-ampere characteristics are appropriately interpreted with space charge analysis. Figure 3 also indicates that the emission may be either electron-rich or ion-rich in this large mean-free-path case. For the very electron-rich and large mean-free-path case the space charge analysis of Langmuir[16] may be used for interpreting the characteristics. If ion emission is not negligible, however, then a more general analysis is required, along the lines indicated in Sections IV and V.

Figure 2 indicates that those characteristics associated with a mean free path which is small compared to the interelectrode distance also tend to have a Debye length small compared to the interelectrode spacing. Because of the smallness of the mean free path the analysis of these characteristics must include diffusion and mobility effects. Because of the smallness of the Debye length a first analysis may assume quasineutrality and divide the interelectrode space into sheath and plasma regions. Such a model is developed here for both the electron-rich and ion-rich cases.

The effects of sheath and volume ionization can be identified in the characteristics and are briefly discussed here. An extensive analysis of

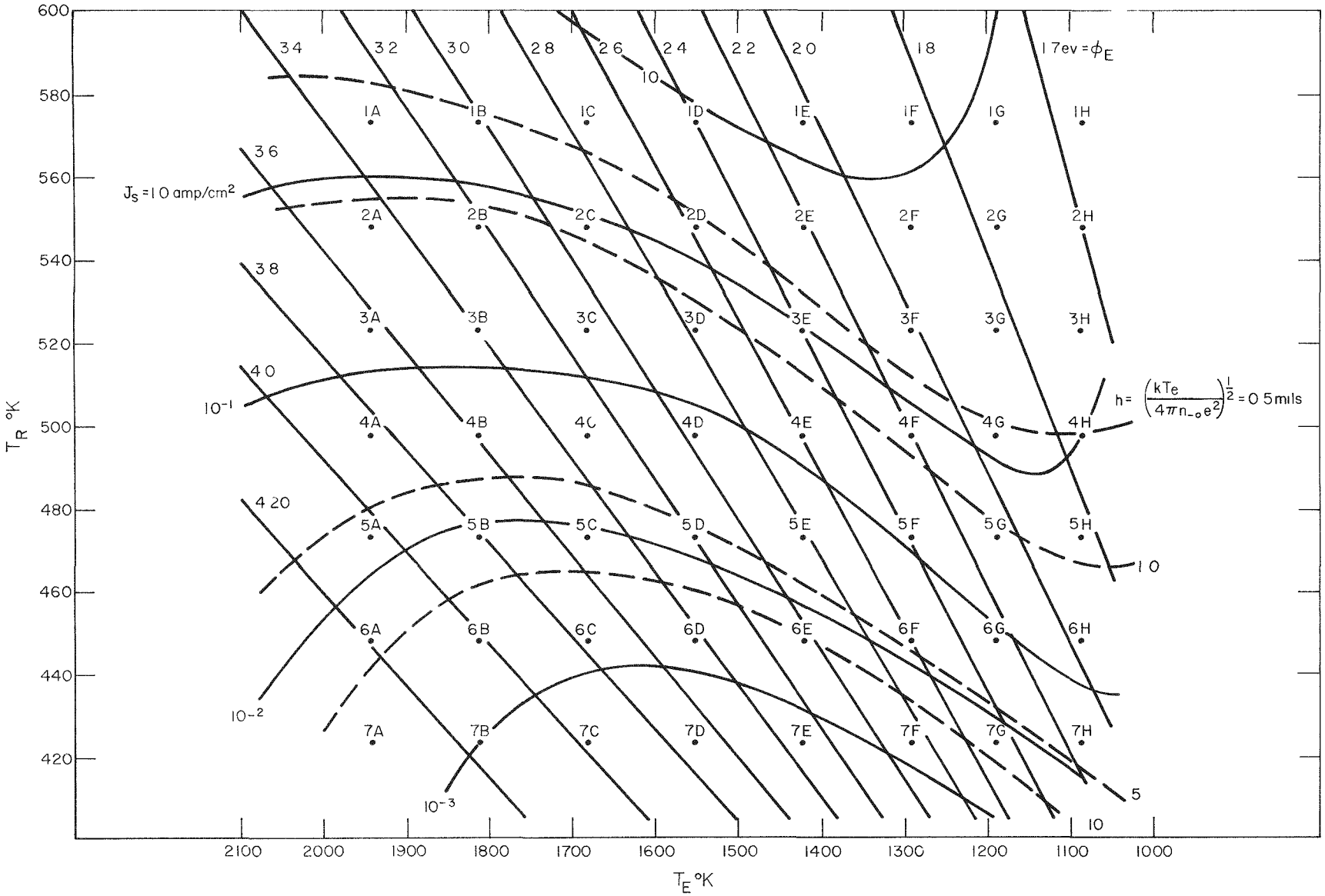

Figure 2. Work Function, Emitted Current, and Debye Length for Cesium-Covered Molybdenum

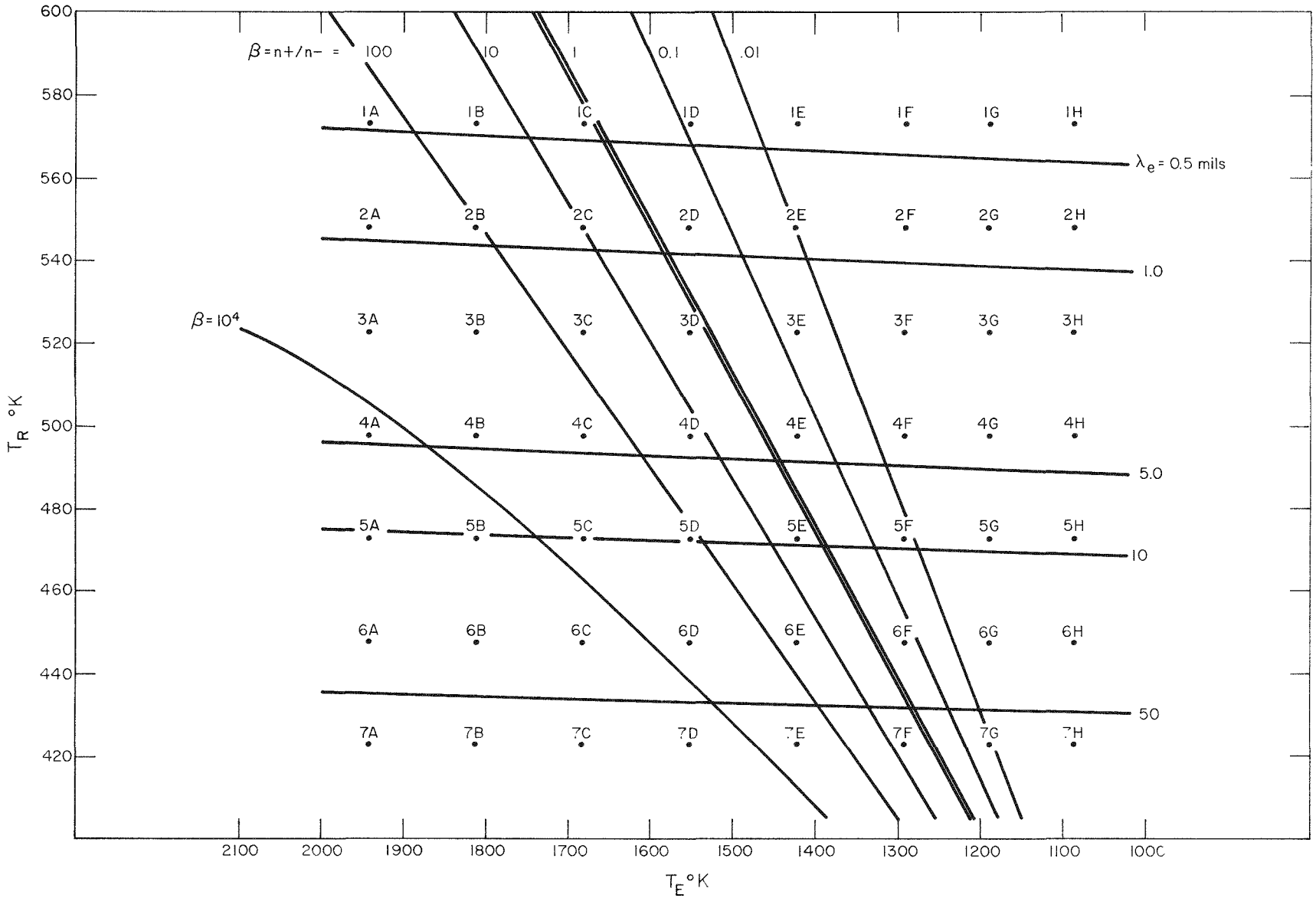

Figure 3. Emission Ratio for Cesium-Covered Molybdenum and Mean Free Path for Electrons in Cesium

these effects however will not be given.

Surface Ionization Modes

1. Space Charge Mode

A collisionless model is appropriate for interpreting the characteristics of Section VI which are associated with low pressure (T_R <480°K) and close spacing (L=5 mils). In these cases the electron mean free path is large compared to the interelectrode spacing (λ_e=2L to 10L). The collisionless model for the surface ionization mode has been examined in Section IV and V. The analysis of Section IV provides the necessary background for the calculation of volt-ampere characteristics. Section V indicates the voltage interval over which converter currents are space charge limited. When ion generation at the emitter can be neglected ($\beta \ll 1$) the characteristics should approximate those determined from Langmuir's space charge analysis.

Since Langmuir's space charge analysis assumes a vacuum diode and assumes electrons only to be generated at the emitter, the characteristics most likely to correspond to his analysis are those for postion 7H in Figures 2 and 3. The characteristics for this position, for several spacings, is shown in Figure 4. It is difficult to compare the voltage and spacing dependence obtained from space charge calculations to that shown in this figure since the saturation current is not determined. Position 7G has a lower saturation current and the results of Section VI indicate that the β value for this position is low enough that the volt-ampere characteristic is not significantly affected by ion emission. The calculated and experimental characteristics for this position are shown in Figure 5. The theoretical curves were calculated assuming a saturation current of 62.5 ma. The voltage coordinate for the experimental curves has been corrected for a

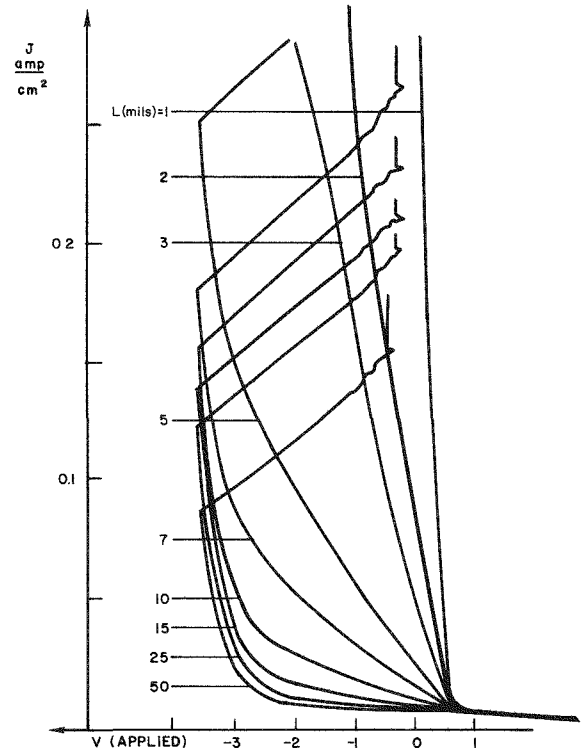

Figure 4. Volt-Ampere Characteristics for Position 7H of Figure 2

0.7-volt contact potential difference. A possible error in the position of the curves with respect to the current coordinate was not corrected for. Figure 5 indicates a qualitative agreement between the experimental and calculated curves. It is interesting to note that the experimental curves develop a saturation for both the close and the wide spacing cases. The former is evidently the true saturation current; the latter "apparent" saturation could be either a saturation induced by diffusion and mobility effects such as discussed in the next sub-topic (Plasma Mode), or a true saturation current from high work function patches. Since the mean free path is so large in this case ($\lambda_e \approx L$) the latter explanation seems more reasonable. Since the two currents differ only by a factor of 5 to 10, the space charge barrier that would be needed to produce this reduction in current

is of the order of the difference in patch contact potential that would produce the relative saturation currents. It is reasonable, therefore, that some patches could be space charge limited while others were emitting saturated currents. According to the results of Section V the low work function patches would not have saturated (62.5 ma) for the 50-mil spacing case until about 36 volts had been applied across the diode. For the same spacing, however, the high work function patches (5-10 ma saturation) would saturate near zero applied voltage. This conforms to the experimental results shown in Figure 5.

A result of Section V which should be compared to the characteristics of Section VI is that for β values equal to or greater than 1.2, no space charge limitations can exist in a diode operating in the surface ionization mode. This effect can be observed qualitatively in the characteristics for the 4-B to 4-H, the 5-A to 5-H, the 6-A to 6-H and the 7-B to 7-H sequences, for the 5- and 10-mil spacings. In the characteristics with $\beta<1.2$ there is little variation with emitter temperature of the voltage needed to produce saturation current. With $\beta>1.2$, however, the voltage needed to produce saturation varies rapidly with emitter temperature. This variation occurs because the saturation current changes, therefore ξ_L and η_L vary. The exact value of β for which the transition takes place cannot be determined because characteristics were not taken for smaller intervals of emitter temperature and because of the uncertainties in β as a function of cesium reservoir and emitter temperatures.

2. Plasma Mode

This discussion will be concerned with the high-pressure diode which has a plasma region as well as emitter and collector sheaths and which has surface ionization as the only source of ions. The collisionless, long

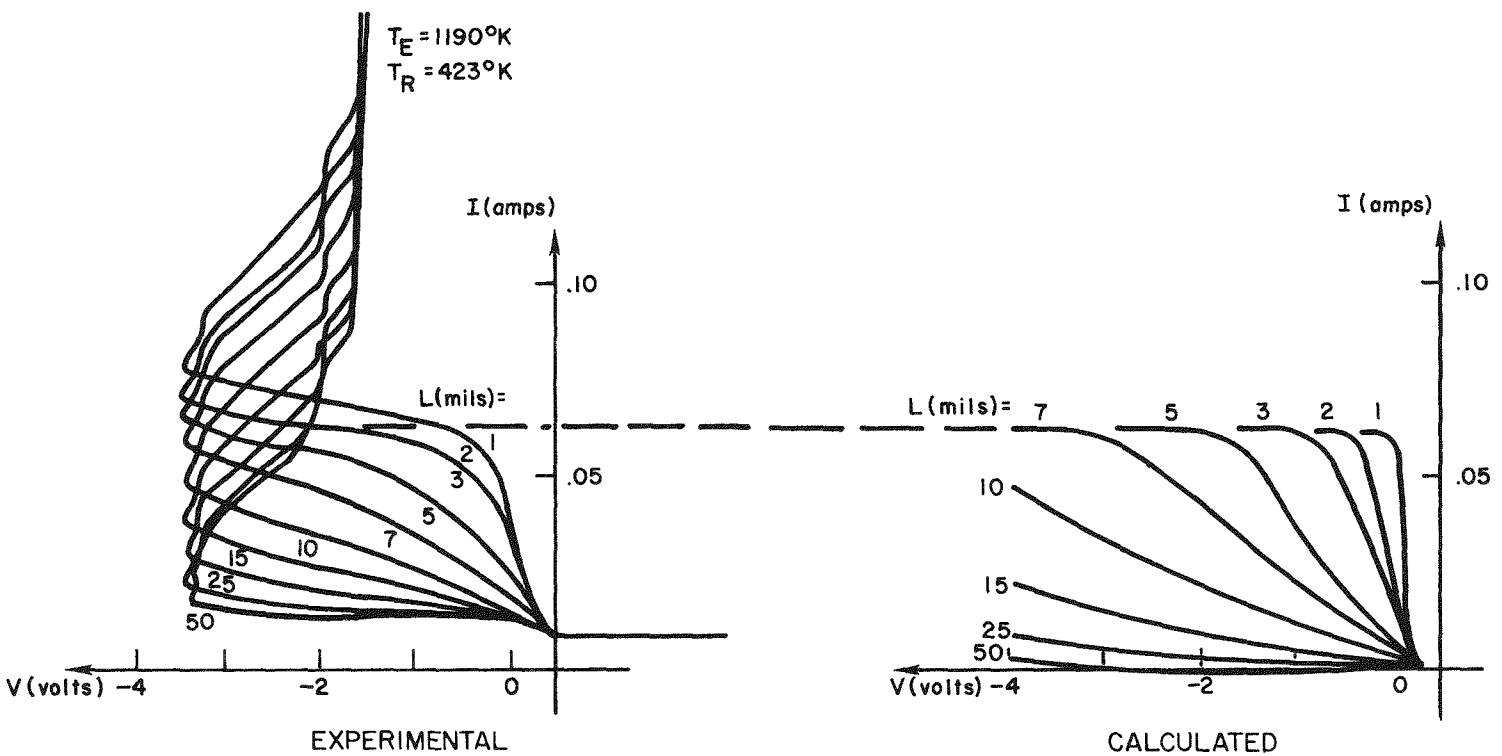

Figure 5. Comparison of Converter Volt-Ampere Characteristics for Position 7G in Figure 2 with Some Vacuum Diode Characteristics for the Same Emitter Temperature and Saturation Current

mean-free-path case, has been considered in Sections IV and V.

a. Plasma Equations

The basic equations for the plasma region are assumed to be

$$\frac{\Gamma_e}{D_e} = -\nabla n - \frac{e}{kT} n\mathcal{E} \qquad \ldots (3)$$

$$\frac{\Gamma_p}{D_p} = -\nabla n + \frac{e}{kT} n\mathcal{E} \qquad \ldots (4)$$

The notation is conventional and given in the glossary. These equations assume approximate charge neutrality. They also assume that the electron temperature is that of the emitter; and that the Einstein relation, $\mu = eD/kT$, is valid. The electron distribution function will not be characterized by the emitter temperature if there is a large injection voltage. In this case, the electron "temperature" might better be determined by an energy balance equation[17] or even more exactly by approximate use of the Boltzmann equation.[18] Inelastic collisions will tend to keep the electron "temperature" from increasing strongly with increasing injection voltage. For this reason and because of the invalidity of the model in the presence of important volume ionization effects, the present model is considered a good first approximation.

Equations 3 and 4 can be solved for the particle density

$$\nabla n = -\frac{1}{2}\left(\frac{\Gamma_e}{D_e} + \frac{\Gamma_p}{D_p}\right) \qquad \ldots (5a)$$

$$n(x) = n(0) - \frac{1}{2}\left(\frac{\Gamma_e}{D_e} + \frac{\Gamma_p}{D_p}\ x\right) \qquad \ldots (5b)$$

where n(0) is the particle density at the emitter edge of the plasma.

Equations 3 and 5a or 4 and 5a can be solved for the electric field, $\mathcal{E}$,

$$\mathcal{E} = -\frac{kT}{2e}\,\frac{1}{n}\left(\frac{\Gamma_e}{D_e} - \frac{\Gamma_p}{D_p}\right) \qquad \ldots (6)$$

This electric field $\mathcal{E}$ then determines the charge difference $e(n_p - n_e)$ by Poisson's equation

$$\frac{d\mathcal{E}}{dx} = \frac{e}{\epsilon_o}(n_p - n_e) = \frac{kT}{e}\,\frac{1}{2}\left(\frac{\Gamma_p}{D_p} - \frac{\Gamma_e}{D_e}\right)\,\frac{1}{2}\left(\frac{\Gamma_e}{D_e} + \frac{\Gamma_p}{D_p}\right)\,\frac{1}{n^2} \qquad \ldots (7)$$

Equation 7 must be used to check the assumption of approximate charge neutrality.

b. Boundary Conditions for $\eta_E > 0$, $\eta_C < 0$

The plasma equation 5b must be supplemented by boundary conditions which reflect the continuity of particle flow. For a positive emitter sheath, $\eta_E = eV_E/kT > 0$, and a negative collector sheath, $\eta_C = eV_C/kT < 0$, as shown in Figure 6, these boundary conditions are

$$\frac{n_{eC}\,v_e}{4} - \frac{\Gamma_e}{2} = 0 \qquad \ldots (8)$$

$$\left(\frac{n_{eC}\,v_p}{4} + \frac{\Gamma_p}{2}\right) e^{\eta_C} = \Gamma_p \qquad \ldots (9)$$

$$\nu_e - \left(\frac{n_{eE}\,v_e}{4} - \frac{\Gamma_e}{2}\right) e^{-\eta_E} = \Gamma_e \qquad \ldots (10)$$

$$\frac{n_{eE}\,v_p}{4} + \frac{\Gamma_p}{2} = \nu_p e^{-\eta_E} \qquad \ldots (11)$$

where ν_e and ν_p are the emitted electron and ion fluxes. Equation 10 assumes that the fraction $e^{-\eta_E}$ of the current incident on the emitter sheath from the plasma, $\Gamma_e = \frac{n_{eE}\,v_e}{4} - \frac{\Gamma_e}{2}$, penetrates to the emitter. Equation 10 thus assumes that the electrons are characterized by the emitter temperature.

c. Solution of Equations for $\eta_E > 0$, $\eta_C < 0$

The plasma density n_{eC} is related to the density n_{eE} by the plasma

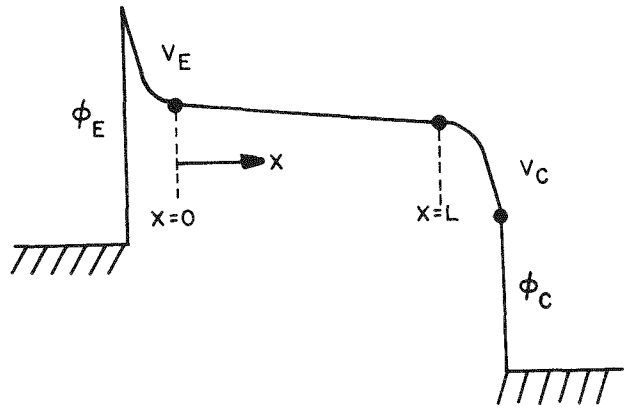

Figure 6. Potential Distribution for Ion-Rich Emission and an Accelerating Collector Sheath

Equation 5b. Then, the four equations (8), (9), (10) and (11) determine the four unknowns Γ_p, η_E, η_C, and n_{eE} for an assumed value for Γ_e. Finally, the plasma potential drop, $\Delta\eta$ is determined by integrating the electric field given by Equation 6.

Algebraic manipulation of Equations 8 to 11 yields

$$1 - \frac{\Gamma_e}{\nu_e} = \frac{1}{8}\left(\frac{3L}{4\lambda_e}\right)^2 \left(\frac{1+R}{2}\right)^2 \left(\frac{\Gamma_e}{\nu_e}\right)^2 \left[1 + \frac{1 + \frac{\lambda_p}{\lambda_e} R}{(1+R)\frac{3L}{4\lambda_e}}\right] \qquad \ldots (12)$$

$$e^{-\eta_E} = \frac{1 - \Gamma_e/\nu_e}{\left(\frac{\Gamma_e}{\nu_e}\right)\left(\frac{1+R}{2}\right)\left(\frac{3L}{4\lambda_e}\right)} \qquad \ldots (13)$$

$$e^{-\eta_C} = \left(\frac{\lambda_e}{\lambda_p} + R\right)(2R) \qquad \ldots (14)$$

$$\Gamma_r \equiv \frac{n_{eE}\, v_e}{4} = \frac{\Gamma_e}{2}\left[1 + (1+R)\frac{3L}{4\lambda_e}\right] \qquad \ldots (15)$$

$$\Delta\eta \equiv \int_0^L \frac{e\mathcal{E}}{kT}\, dx = -\frac{1-R}{1+R} \ln \frac{\Gamma_r}{\Gamma_e/2} \qquad \ldots (16)$$

where

$$D_e = \frac{1}{3}\lambda_e v_e \qquad D_p = \frac{1}{3}\lambda_p v_p$$

$$\frac{\Gamma_p}{\Gamma_e} = R\frac{D_p}{D_e} = R\frac{1}{500}\frac{\lambda_p}{\lambda_e}$$

$$\nu_p = \beta\frac{1}{500}\nu_e$$

The parameter R has been chosen so that the electric field $\mathcal{E}$ in the plasma vanishes for R=1 according to Equation 6; the parameter R vanishes for infinite applied field $\eta_C = -\infty$ according to Equation 14.

Plots of Equations 12, 14, 15 and 16 are presented in Figures 7 to 10. In Figure 7, Equation 12 is plotted for $\frac{3L}{4\lambda_e} >> 1$. This model predicts the saturation currents in the ion-rich cases. More explicitly, for R=0, the abscissa in Figure 7 is just $\gamma = \frac{1}{\beta}\left(\frac{3L}{4\lambda_e}\right)^2$ and determines the saturation current $\Gamma_e/\nu_e\Big|_{R=0}$. Equation 12 holds for all negative η_C, and thus R varies from R=0 at $\eta_C = -\infty$ to $R = \lambda_e/\lambda_p$ at $\eta_C = 0$.

Equation 14 is plotted in Figure 8 for two values of λ_e/λ_p. Equation 15 is plotted in Figure 9 and Equation 16 in Figure 10. The parameter R was varied only between 0 and 1, although the equations hold for larger values.

d. Boundary Conditions for $\eta_E > 0$, $\eta_C > 0$

The boundary conditions (8) and (9) at the collector must be changed for the positive collector sheath $\eta_C = \frac{eV_C}{kT} > 0$ shown in Figure 11:

$$\left(\frac{n_{eC}\, v_e}{4} + \frac{\Gamma_e}{2}\right) e^{-\eta_C} = \Gamma_e \qquad \ldots (17)$$

$$\frac{n_{eC}\, v_p}{4} + \frac{\Gamma_p}{2} = \Gamma_p \qquad \ldots (18)$$

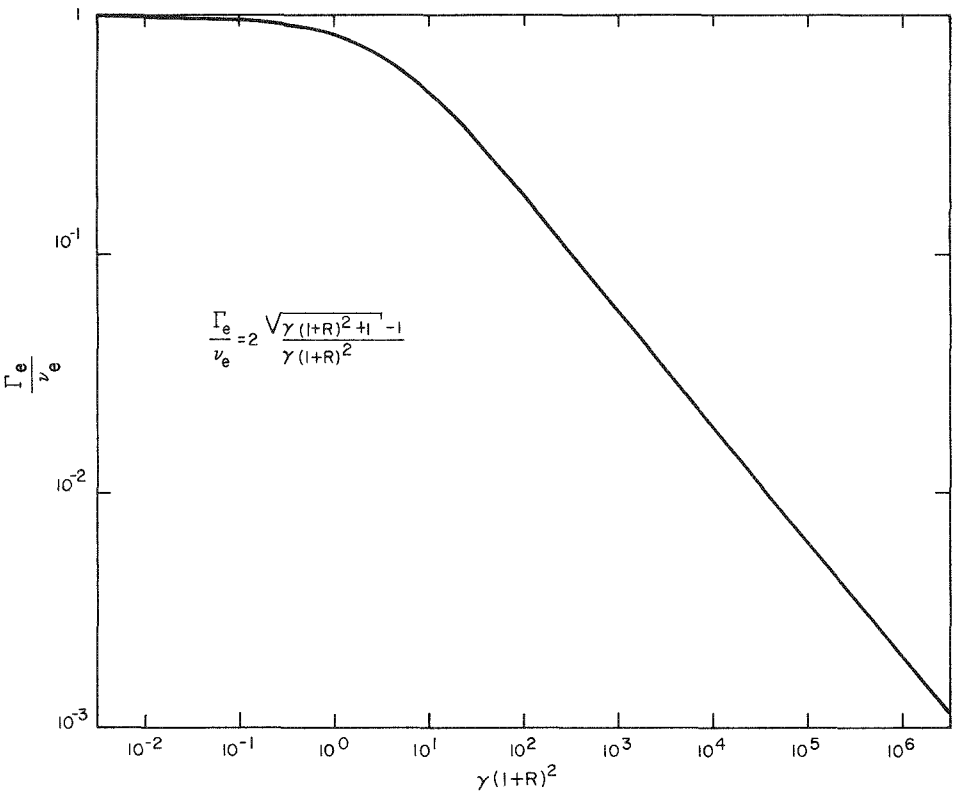

Figure 7. Diode Current, Γ_e/ν_e, Vs. the Parameter $\gamma(1"R)^2$

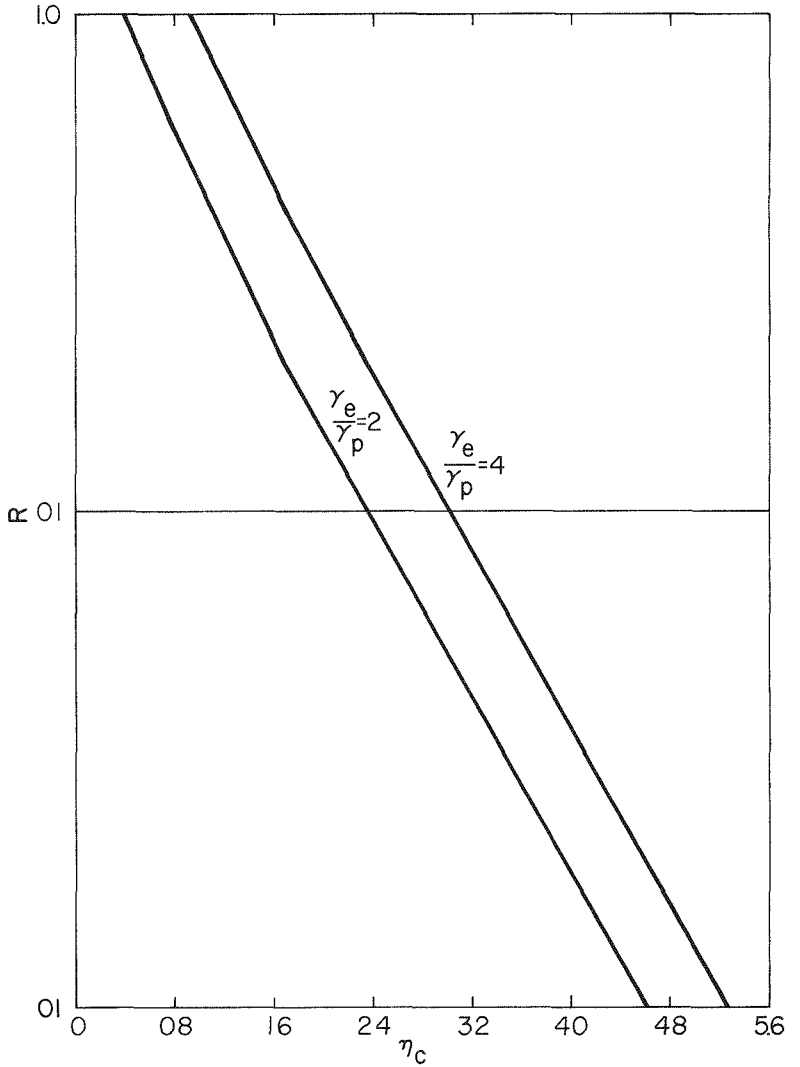

Figure 8. Current Ratio Coefficient, R, Vs. the Collector Sheath Potential for Ion-Rich Emission

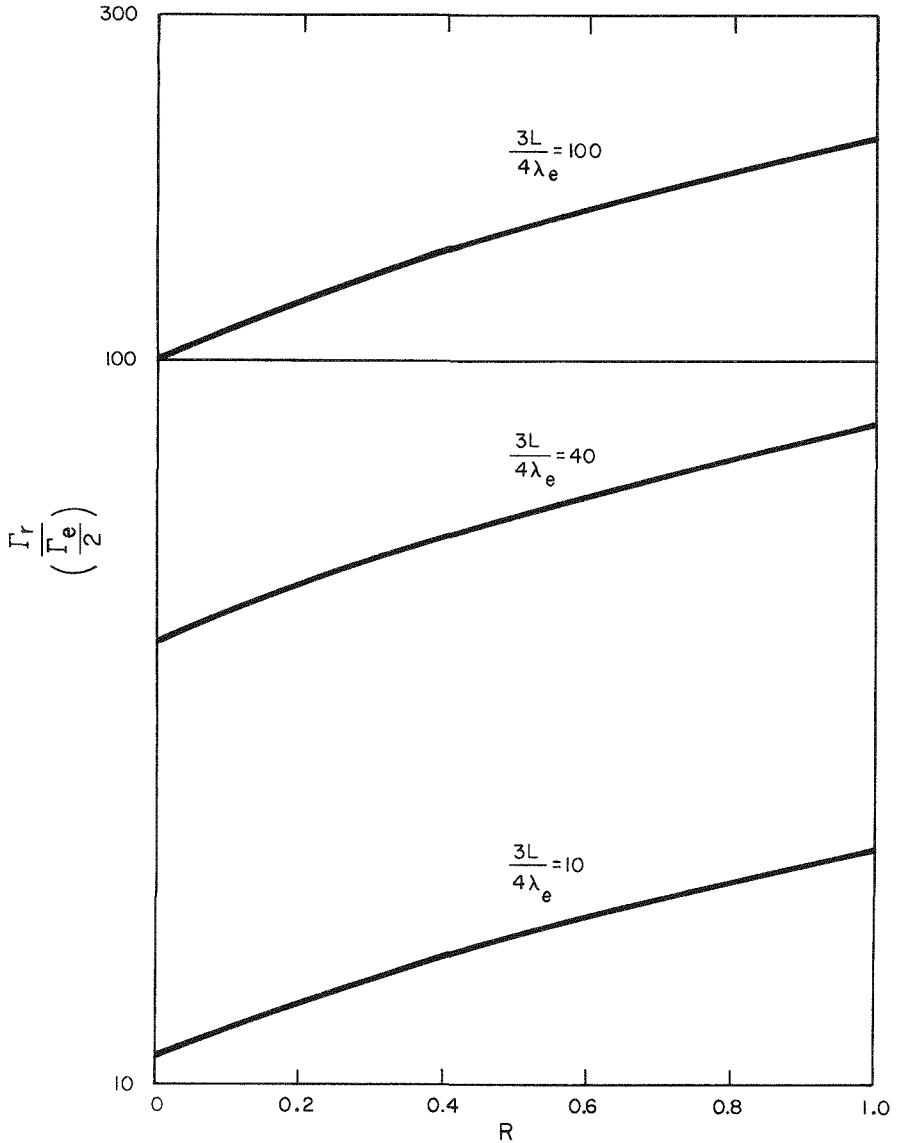

Figure 9. Random Current, Γ_r, at the Emitter Sheath Edge Vs. the Current Ratio Coefficient, R

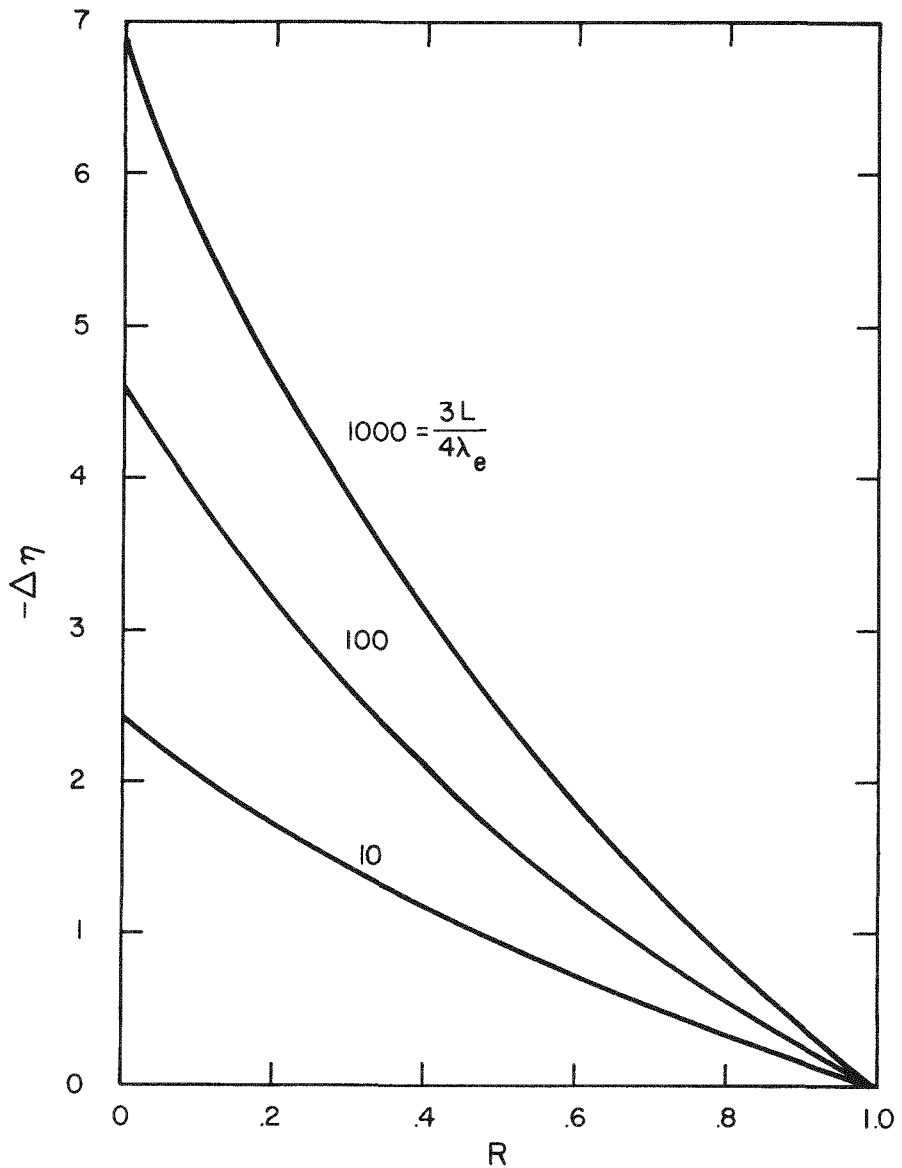

Figure 10. Potential Drop in the Plasma Vs. the Current Ratio Coefficient, R

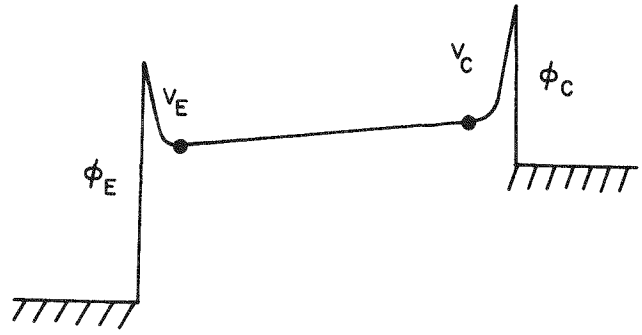

Figure 11. Potential Distribution for Ion-Rich Emission and a Retarding Collector Sheath

e. Solution of Equation for $\eta_E>0$, $\eta_C>0$

Algebraic manipulation of Equations 10, 11, 12, 17 and 18 yields

$$1 - \frac{\Gamma_e}{\nu_e} = \frac{1}{\beta}\left(\frac{3L}{4\lambda_e}\right)^2\left(\frac{1+R}{2}\right)^2\left(\frac{\Gamma_e}{\nu_e}\right)^2 \left[1 + \frac{R\frac{\lambda_p}{\lambda_e}}{\frac{3L}{4\lambda_e}\left(\frac{1+R}{2}\right)}\right]\left[1 + \frac{R\frac{\lambda_p}{\lambda_e} - 1}{\frac{3L}{4\lambda_e}(1+R)}\right] \quad \ldots (19)$$

$$e^{-\eta_E} = 2\,\frac{\frac{\nu_e}{\Gamma_e} - 1}{R\frac{\lambda_p}{\lambda_e} - 1 + \frac{3L}{4\lambda_e}(1+R)} \quad \ldots (20)$$

$$e^{\eta_C} = \frac{R\frac{\lambda_p}{\lambda_e} + 1}{2} \quad \ldots (21)$$

$$\Gamma_r = \frac{1}{2}\Gamma_e\left[R\frac{\lambda_p}{\lambda_e} + \frac{3L}{4\lambda_e}(1+R)\right] \quad \ldots (22)$$

$$\Delta\eta = -\frac{1-R}{1+R}\,\ell n\,\frac{\Gamma_r}{\frac{\Gamma_e}{2}R\frac{\lambda_p}{\lambda_e}} \quad \ldots (23)$$

Equations 19 to 23 are identical with Equations 11 to 16 for $\eta_C=0$. The saturation ion current for $\eta_C = \infty$ ($R=\infty$) can be calculated from Equations 19 and 20

$$\left.\frac{\Gamma_p}{\nu_p}\right|_{R=\infty} = \frac{2}{\sqrt{\beta}} \frac{1}{\frac{\lambda_e}{\lambda_p}\frac{3L}{4\lambda_e} = 1} \qquad \ldots (24)$$

For $\frac{3L}{4\lambda_e} >> 1$, the ratio of the ion to electron saturation currents becomes

$$\frac{\Gamma_p[R=\infty]}{\Gamma_e[R=0]} = \frac{1}{500}\frac{\lambda_p}{\lambda_e}\frac{\sqrt{\gamma}}{\sqrt{\gamma+1}-1} \qquad \ldots (25)$$

$$= \frac{1}{500}\frac{\lambda_p}{\lambda_e} \quad \gamma >> 1$$

$$= \frac{1}{250}\frac{\lambda_p}{\lambda_e}\frac{1}{\sqrt{\gamma}} \quad \gamma << 1$$

f. Check on Approximate Neutrality

According to Equation 7

$$\frac{n_p - n_e}{n} = -\frac{\epsilon_o kT}{e^2 n}\frac{1}{\lambda_e^2}\left(\frac{3\Gamma_e}{2n\ v_e}\right)^2 (1-R^2) \qquad \ldots (26)$$

The factor, $\epsilon_o kT/e^2 n$, is the square of the Debye length, h^2. For $\eta_C > 0$, Equation 18 is used to evaluate n:

$$\frac{n_p - n_e}{n} = -\left(\frac{\epsilon_o kT}{e^2 n_{eC}}\right)\frac{1}{\lambda_p^2}\left(\frac{3}{4}\right)^2\left(1 - \frac{1}{R^2}\right)\left(\frac{n_{eC}}{n}\right)^3 \quad ; \eta_C > 0 \qquad \ldots (27)$$

$$\leq \left(\frac{3h_c}{4\lambda_p}\right)^2 \quad ; \frac{n_{eC}\ v_p}{2} = \Gamma_p \qquad \ldots (27a)$$

For $\eta_C < 0$, Equation 8 is used to evaluate n:

$$\frac{n_p - n_e}{n} = -\left(\frac{3h_c}{4\lambda_e}\right)^2 (1-R^2)\left(\frac{n_{eC}}{n}\right)^3 \qquad \ldots (28)$$

$$\leq \left(\frac{3h_c}{4\lambda_c}\right)^2 \quad ; \frac{n_{eC}\ v_e}{2} = \Gamma_e \qquad \eta_C < 0 \qquad \ldots (28a)$$

The check on approximate neutrality is completed by evaluating Γ_p or Γ_e with Equation 24 or 12, and introducing the corresponding density n_c into Equation 27a or 27b.

g. Diffusion and Conduction Currents

The total currents Γ_e and Γ_p consist of diffusion currents Γ_{diff} and conduction currents Γ_{cond}

$$\Gamma^{(e,p)}_{diff} = - D_{e,p} \nabla n$$

$$\Gamma^{(e,p)}_{cond} = \mp \mu_{e,p} n \mathcal{E}$$

These currents are related to the parameter R by the following equations:

$$\Gamma^{(e)}_{diff} = \frac{1}{2} (1+R) \quad ; \quad \frac{\Gamma^{(e)}_{cond}}{\Gamma_e} = \frac{1}{2} (1-R) \qquad \ldots (29)$$

for electrons, and

$$\frac{\Gamma^{(p)}_{diff}}{\Gamma_p} = \frac{1}{2} (\frac{1}{R} + 1) \quad ; \quad \frac{\Gamma^{(p)}_{cond}}{\Gamma_p} = - \frac{1}{2} (\frac{1}{R} - 1) \qquad \ldots (30)$$

for ions.

Thus, for the ion-rich case with an accelerating potential $\eta_c<0$, the R varies between $R=0(\eta_c=-\infty)$ and $R=1$ $(\mathcal{E}=0)$. The electron diffusion current is seen to contribute from 50% at R=0 to 100% of the current at R=1. The ion diffusion current exceeds the total ion current and is opposed by the conduction current, and exactly canceled for $\eta_c=-\infty$.

h. An Ion-Rich Example

An example of an ion-rich plasma mode is given in the following discussion. For this example the following parameters are chosen:

$$\beta = 10, \ \lambda_e/\lambda_p = 2, \ 3L/4\lambda_e = 100$$

Equations 12 to 16 and 19 to 23 yield the results shown in Table I.

TABLE I. DIODE PARAMETERS FOR

$\beta = 10$, $\lambda_e/\lambda_p = 2$, $3L/4\lambda_e = 100$

Γ_e/υ_e	R	η_E	η_C	$\Gamma_r/(\Gamma_e/2)$	$\Delta\eta$	$\eta=\eta_E-\Delta\eta-\eta_C$
≥0.060	0	1.20	$-\infty$	101	-4.61	∞
0.058	0.06	1.20	-2.84	106	-4.12	8.16
0.050	0.19	1.20	-1.73	120	-3.25	6.18
0.040	0.52	1.20	-0.90	153	-1.56	3.66
0.032	0.91	1.20	-0.47	182	-0.25	1.92
0.025	1.43	1.20	-0.18	244	0.98	0.40
0.020	2.00	1.20	0.00	301	1.90	-0.70
0.020	2.10	1.20	0.025	311	2.02	-0.85
0.016	2.94	1.20	0.22	396	2.76	-1.78
0.013	3.95	1.20	0.40	497	3.30	-2.50
0.010	5.31	1.20	0.61	640	3.74	-3.15
0.004	14.64	1.20	1.43	1570	4.69	-4.92
0.002	38.9	1.20	2.33	4010	5.10	-6.23
0	∞	1.20	∞	∞	5.31	$-\infty$

The value of η_E is assumed to be 1.20 although it actually varies slowly from 1.20 at R=0 to 1.16 at R=∞. The ratio of the density n_{eE} to n_{eC} is is given by the argument at the logarithms in Equations 16 and 23 for $R \lesssim \lambda_e/\lambda_p$. The density is thus decreased by a factor ranging between 101 and 301. This factor is of the order of $3L/4\lambda_e$ for many mean-free-path cases. In order to proceed further, it is assumed that the emitter is molybdenum and its temperature is 1530°K.

Then according to Figures 2 and 3,

$$\lambda_e = 5 \text{ mils}$$

$$\phi_E = 2.92 \text{ ev}$$

$$\nu_e = 8 \times 10^{-2} \text{ amps/cm}^3$$

The resulting volt-ampere curve is shown in Figure 12. An important feature in Table I and Figure 12 is the saturation of the diode current well below the emitted current.

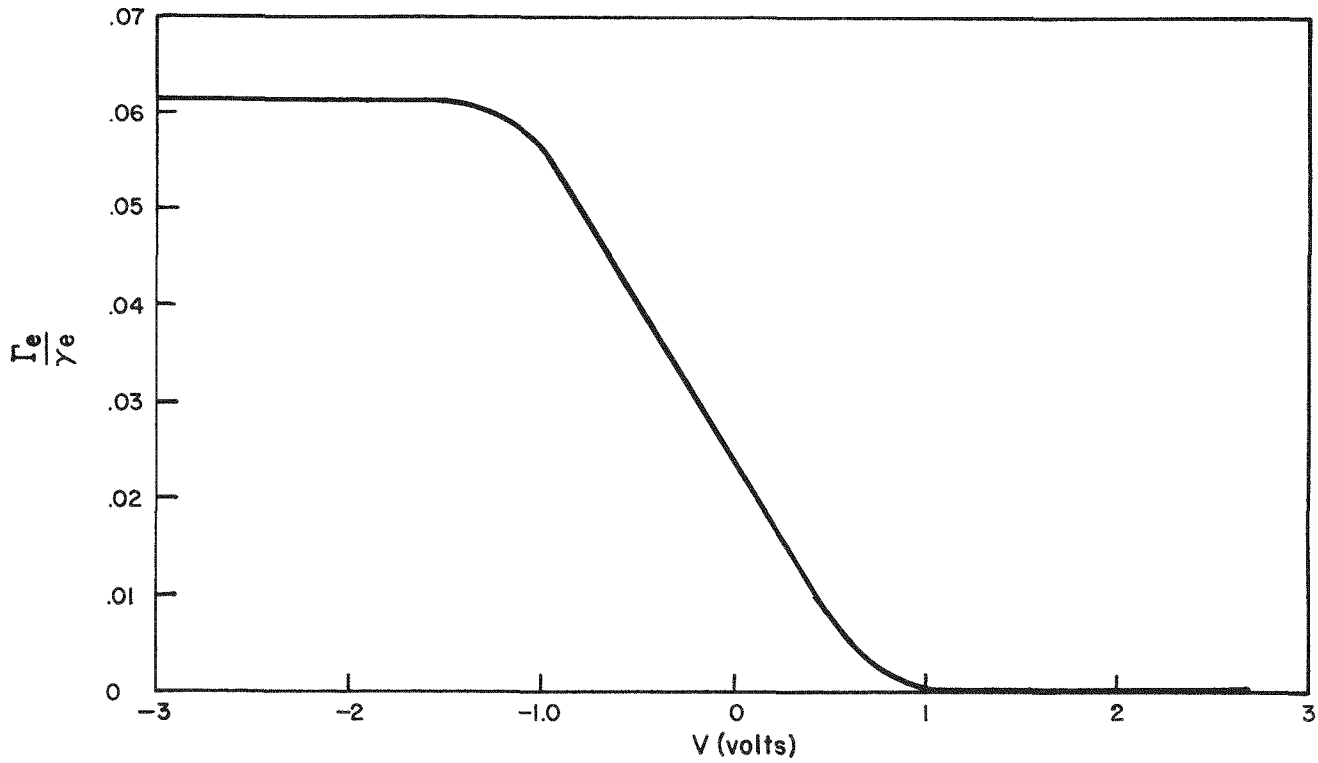

Figure 12. Volt-Ampere Characteristic
for Ion-Rich Emission
According to Plasma Model

For $\eta_c<0$, the Debye length assumes its largest value for R=2 and according to Equation 28b and Figure 2:

$$h_c = h_c \left[\nu = \frac{(.02)8(10^{-2})}{2}, \; T = 1530°K\right]$$

$$= 10^{-2}\text{cm}$$

and

$$\frac{n_p - n_e}{n} \leq \frac{3h_c}{4\lambda_e}^2 = .35$$

For $\eta_c>0$, the Debye length assumes its largest value for R=2 and the same inequality holds as for $\eta_c<0$. It is difficult to determine the extent which

the above breakdown of charge neutrality affects the volt-ampere curve of Figure 12.

i. Patch Effect for an Ion-Rich Case

The importance of patches has recently been emphasized.[19] The patch effect can be included in an approximate manner by altering the expressions for ν_e and ν_p in the boundary conditions. For example, two patches are shown in Figure 13 and the plasma potential is assumed to lie below the surface potentials of both patches as indicated.

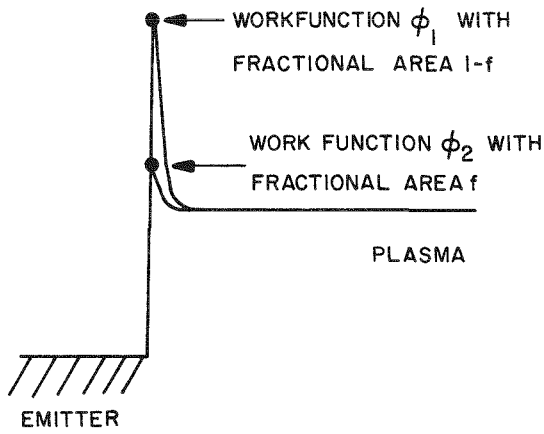

Figure 13. Potential Distribution for Ion-Rich Emission at a Patchy Emitter

This case is interesting if the electron current is predominantly that of patch 2, in which

$$\nu_e \rightarrow f\nu_{e2}$$

The ion current is here supplied to the plasma by both types of patches in proportion to their area

$$\nu_p e^{-\eta_E} \rightarrow (1-f)\ \nu_{p1} e^{-\eta_E} + f\nu_{p2} e^{-\eta_E + \frac{(\phi_1+\phi_2)}{kT}}$$

$$= \nu_{p1} e^{-\eta_E} \quad ; \quad \phi_1 - I - V_E > 4kT$$

The equations 12 to 16 can now be used with the interpretation for ν_e and ν_p just derived. It must be remembered that $\beta = \frac{500\nu_p}{\nu_e} \rightarrow \frac{500\nu_{p1}}{f\nu_{e2}}$, and similarly $\gamma \rightarrow \frac{f\upsilon_{e2}}{500\nu_{p1}}\left(\frac{3L}{4\lambda_e}\right)^2$

j. Boundary Conditions for $\eta_E<0$, $\eta_C<0$

Equations 8 and 9 are valid at the collector. At the emitter, the boundary conditions are

$$\nu_e e^{\eta_E} - \frac{n_e E v_e}{4} - \frac{\Gamma_e}{2} = \Gamma_e \qquad \ldots (31)$$

$$\nu_p - \left(\frac{n_e E v_p}{4} - \frac{\Gamma_p}{2}\right) e^{\eta_E} = \Gamma_p \qquad \ldots (32)$$

k. Solution of Equations for $\eta_E<0$, $\eta_C<0$

Algebraic manipulation of Equations 8, 9, 31 and 32 with 33 yields

$$\frac{\Gamma_p}{\nu_p} = \frac{\lambda_p}{\lambda_e}\frac{R\Gamma_e}{\beta\nu_e} = 2\,\frac{\sqrt{\beta\left(\frac{3L}{4\lambda_p}\right)^2\left(1+\frac{1}{R}\right)^2 F + 1} - 1}{\beta\left(\frac{3L}{4\lambda_p}\right)^2\left(1+\frac{1}{R}\right)^2 F} \qquad \ldots (33)$$

with $$F \equiv \left[1 + \frac{1-R\,\frac{\lambda_p}{\lambda_e}}{\frac{3L}{4\lambda_e}(1+R)}\right]\left[1 + \frac{2}{\frac{3L}{4\lambda_e}(1+R)}\right] \simeq 1 \text{ for } \frac{3L}{4\lambda_e} \gg 1$$

$$e^{\eta_E} = \frac{\Gamma_e}{\nu_e}\left[1 + \left(\frac{1+R}{2}\right)\frac{3L}{4\lambda_e}\right] \qquad \ldots. (34)$$

The quantities η_C, Γ_r, and $\Delta\eta$ are given by Equations 14, 15 and 16. The saturation current, Γ_e/ν_e, is given by evaluating Equation 33 for R = 0 according to Equation 14:

$$\left.\frac{\Gamma_e}{\nu_e}\right|_{\eta_C = -\infty} = \left.\frac{\Gamma_e}{\nu_e}\right|_{R=0} = \frac{2}{\sqrt{\gamma F}} \qquad \ldots (35)$$

For $0<R<\frac{\lambda_e}{\lambda_p} = 2$, the ion current Γ_p contributes negligibly to the total current $\Gamma = \Gamma_e - \Gamma_p$.

1. Boundary Conditions for $\eta_E<0$, $\eta_C>0$

For $\eta_E<0$ and $\eta_C>0$, the boundary conditions are given by Equations 17, 18, 31 and 32.

m. Solution of Equations for $\eta_E<0$, $\eta_C>0$

Algebraic manipulation of Equations 17, 18, 31 and 32 with 38 yields

$$\frac{\Gamma_p}{\nu_p} = \frac{\lambda_p R \Gamma_e}{\lambda_e \beta \nu_e} = 2\,\frac{\sqrt{\beta\left(\frac{3L}{4\lambda_p}\right)^2\left(1+\frac{1}{R}\right)^2 F' + 1} - 1}{\left(\frac{3L}{4\lambda_p}\right)^2\left(1+\frac{1}{R}\right)^2 F'} \qquad \ldots (36)$$

with $$F' \equiv 1 + \frac{1+\frac{\lambda_p R}{\lambda_e}}{\frac{3L}{4\lambda_e}(1+R)}$$

$$e^{\eta_E} = \frac{1}{2}\,\frac{\Gamma_e}{\nu_e}\left[\frac{\lambda_p}{\lambda_e} R + 1 + \frac{3L}{4\lambda_e}(1+R)\right] \qquad \ldots (37)$$

The quantities η_C, Γ_r and $\Delta\eta$ are given by Equations 21, 22 and 23.

n. An Electron-Rich Example

An example of an electron-rich example is given in the following discussion. For this example the following parameters are chosen:

$$\beta = \frac{1}{100} \quad ; \quad \frac{3L}{4\lambda_e} = 100 \quad ; \quad \frac{\lambda_e}{\lambda_p} = 2$$

Equations 14, 15, 16, 33 and 34 for $\eta_C>0$ and Equations 21, 22, 23, 36 and 37 for $\eta_C<0$ yield the results shown in Table II.

TABLE II. DIODE PARAMETERS FOR

$$\beta = \frac{1}{100}, \frac{3L}{4\lambda_e} = 100, \lambda_e/\lambda_p = 2$$

Γ_e/ν_e	R	η_E	η_C	$\Delta\eta$	$\eta = n_E - \Delta\eta - \eta_C$
0.00200	0	-2.28	$-\infty$	-4.61	∞
0.00186	0.06	-2.28	-2.85	-4.16	4.73
0.00170	0.19	-2.28	-1.73	-3.25	2.70
0.00132	0.52	-2.28	-0.90	-1.56	0.18
0.00105	0.91	-2.28	-0.47	-0.25	-1.56
0.00083	1.43	-2.28	-0.18	0.98	-3.08
0.00068	2.00	-2.28	0.00	1.90	-4.18
0.00065	2.10	-2.28	0.03	2.02	-4.33
0.00050	2.94	-2.28	0.22	2.76	-5.26
0.00040	3.95	-2.28	0.40	3.30	-5.98
0.00032	5.37	-2.28	0.61	3.74	-6.63
0.00013	14.65	-2.28	1.43	4.69	-8.40
0.00005	38.9	-2.28	2.33	5.10	-9.71
0	∞	-2.28	∞	5.31	$-\infty$

The volt-ampere curve is plotted in Figure 14 for an emitter temperature

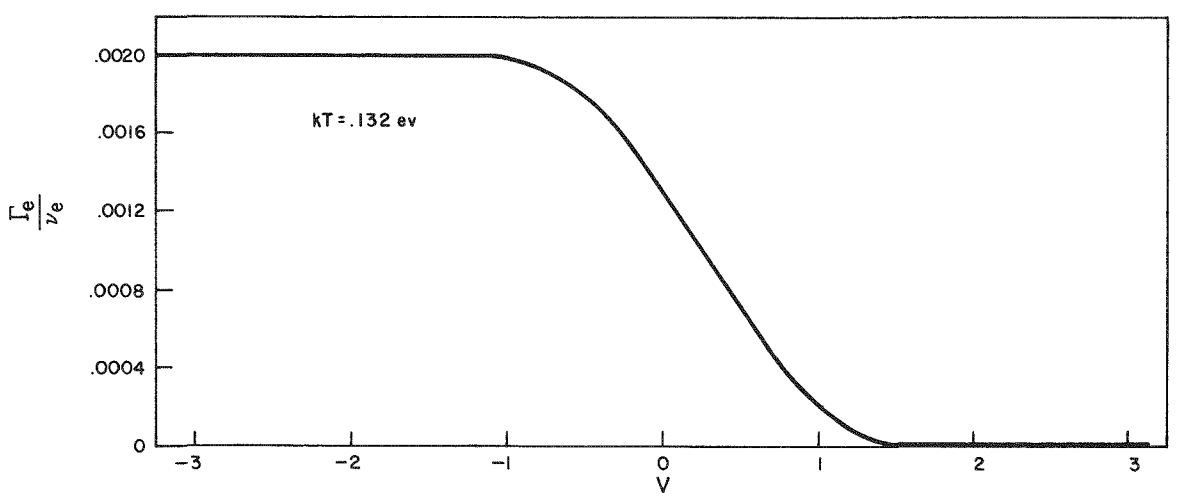

Figure 14. Volt-Ampere Characteristic for Electron-Rich Emission According to Plasma Model

of 1530°K. An important feature of Table II and Figure 14 is the saturation of the diode current at a value well below the emitted current. The magnitude of this saturation current is not determined primarily by space charge limitation but rather the back scattering of electrons[20,21] by the gas. The check on neutrality with Equation 28a yields

$$\frac{n_e - n_p}{n} \leq 16$$

This breakdown of the key assumption on charge neutrality means that the results must be interpreted only qualitatively.

o. Comparison of the Theory with Some Experimental Saturation Currents

Equation 35 for the saturation current in electron-rich cases was checked for $T_R = 573°K$, $T_E = 1293°K$ (position 1F, plotted in Figure 15) and for $T_R = 573°K$, $T_E = 1422°K$ (that is, position 1E). In Figure 16, the experimental saturation currents are plotted versus the inverse spacing (1/L). When T_R and T_E (and therefore also β) are given, the points lie on a straight line in accordance with Equation 35. The saturation current predicted by Equation 33 is actually a factor of four too small, if β, λ and ν are taken from Figures 2 and 3. The dependence of the saturation current on spacing is not found in theories with uniform plasmas.[17,22]

For the very ion-rich case $T_R = 423°K$, $T_E = 1552°K$ (that is, position 7D in Figures 2 and 3) the saturation current is relatively constant. Equation 12 predicts that the saturation current is the emitted current ν_e for $\gamma \leq 10^{-5}$ in the many mean-free-path case. For the case at hand, $L/\lambda_e \leq 1$ and the emitted current ν_e would still be expected. The observed current $\nu_e \simeq 50$ ma is actually about seventy times the predicted emission current by Figure 2. High work function patches may be the reason for this anomaly.

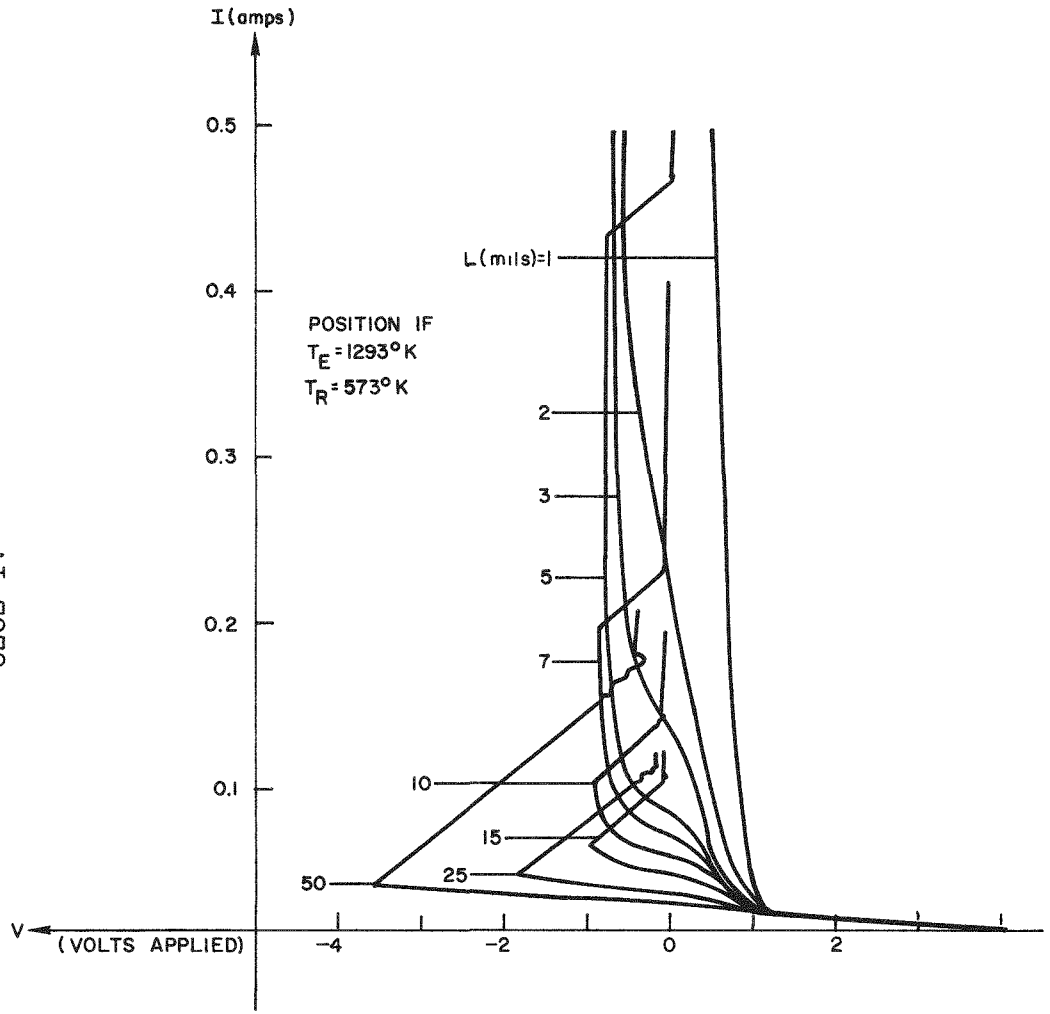

Figure 15. Volt-Ampere Characteristics for Position 1F of Figure 2

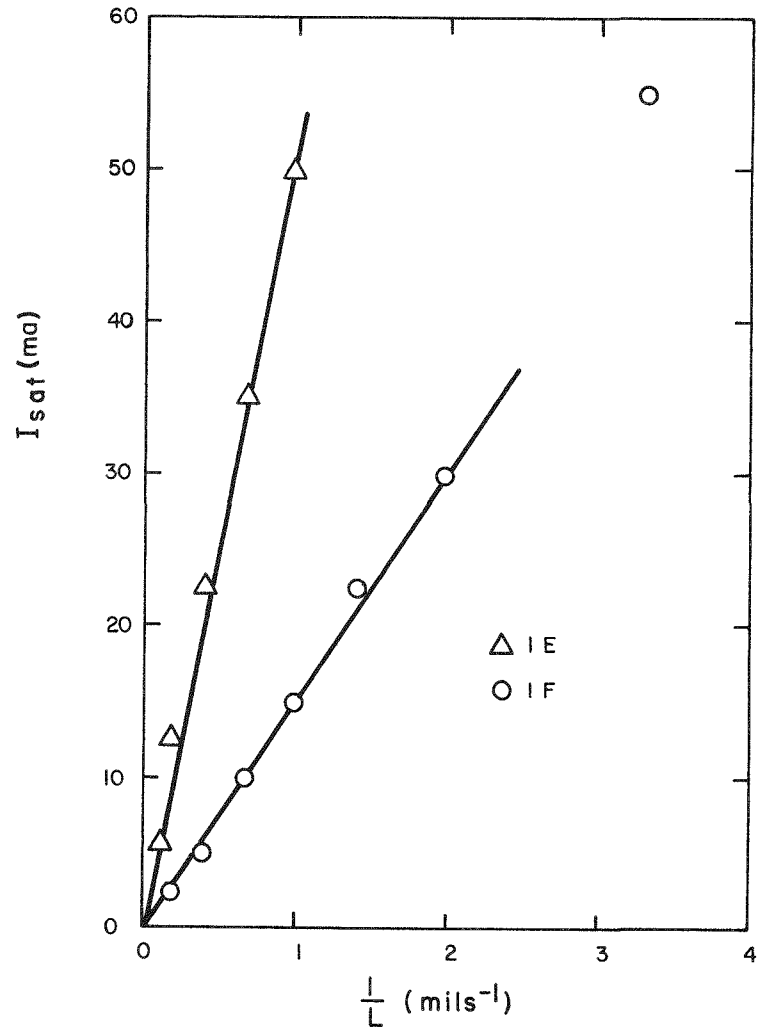

Figure 16. Saturation Current, I_{sat}, Vs. the Reciprocal Spacing, L^{-1}

Sheath Ionization Mode

As the collector voltage is made increasingly negative in the diffusion-limited surface ionization mode, the collector sheath voltage finally exceeds the cesium ionization potential. Cesium ions produced in the collector sheath are able to neutralize more electrons and the current increases above the plateau of the saturation current. This mode has been studied by W.M. Webster, E.O. Johnson and L. Malter[4,6] but not for the planar, close-spaced geometry. The theory already presented for the diffusion-limited surface ionization mode is easily altered to include sheath ionization by use of Webster, Johnson and Malter's ion production term in the boundary conditions. For example, Equation 7 would be modified to

$$\frac{N_e C v_p}{4} - \frac{\Gamma_e}{2} = \frac{3}{8} a\, p \sqrt{C\Gamma_e} \frac{(\Delta V_c)^2}{V_i^{1/4}} \qquad \ldots (38)$$

where C is defined by the Child-Langmuir law

$$\Gamma_e = C\, V^{3/2}/s^2$$

and a by $N = a\, p\, (V - V_i)$

where N is the number of ions produced by centimeter of path lengths per electron in a gas at pressure p and with ionization potential V. The additional electron current due to electrons produced in the sheath is neglected here, but could be included.

In some cases, the initial departure of the electron current from the plateau may be due to the increase in thickness of the collector sheath with accelerating voltage. The corresponding decrease in the plasma thickness results in less back-scattering and increased current. An example of the sheath ionization mode is found in volt-ampere curve 4F for 92 mils spacing. The collector glow is observed at those points where the current has broken away from the plateau just prior to ignition.

In some cases the ignition contact potential difference in the sheath ionization mode is less than the ionization potential of cesium. A possible explanation is that the diode emitter has some high work function paths in some unexplained way. Calculations indicate that the electric field of the collector sheath is not sufficiently strong to lower the ionization potential appreciably and this possibility was discarded. More likely, a two-step ionization process is important, according to some simple calculations, but the density of excited states is difficult to estimate.

A systematic study of the volt-ampere curves of Section IV has not yet been completed; but the following points may be noted. In the sequence 1F, 2F, 3F, 4F, 5F, 6F and 7F at 50 mils the saturation current increases from 2 ma to 30 ma, whereas the emitter current decreases from 40 amperes to 3 ma. These saturation currents are interpreted as diffusion-limited according to the plasma model for 1F through 6F. For these electron-rich cases the emitter sheath also limits the current. For 7F, which is ion-rich, the magnitude of the current indicates that the full emitted current is being passed. The factor of 10 between the observed 30 ma and the expected ma is probably associated with a low work function patch. The additional current due to sheath ionization first appears in 3F. For 1F and 2F, the current at the emitter (the saturation current) is too small to generate appreciable ions. The additional current due to sheath ionization increases in 3F through 6F. This increase is probably due to increased effectiveness of the sheath-produced ion in the larger mean free path case. The number of ions produced in the sheath is very likely decreasing in the sequence 3F to 6F since the density of cesium atoms is decreasing more rapidly than the saturation current is increasing. For 7F, the increase in current due to sheath ionization is again small. The reason is very likely

that all the electrons are traversing the diode and thus additional neutralization does not increase diode current.

Volt-ampere curve 4F for the sequence 92, 50, 25, 15, 10 and 5 mils shows the effect of spacing. The saturation current varies inversely with spacing in accordance with Equation 33 for all spacings except at 5 mils. At 5 mils, the close spacing removes the space charge barrier and there is no saturation of the unignited current.

Finally, as mentioned earlier in ion-rich cases in position, 7D for example, the saturation current is almost two orders of magnitude greater than the expected current. This large factor is a strong indication of low work function patches due perhaps to cesium on an oxide layer.

IGNITED MODE

This study has emphasized the unignited mode, but a few points can be made about ignition and the ignited mode. For small mean free paths, the ignition voltage depends on spacing. For example, the ignition voltage for 1F increases from 1 volt at 10 mil spacing to 3.7 volts at 50 mils. This effect can be attributed to the smaller number of ions being generated since there is less current; and to the decreasing effectiveness of such ions as the spacing is increased.

At small mean free paths, such as 7G in Figure 5, the ignition voltage is independent of spacing. A simple explanation is that the ignition takes place outside the interelectrode space.

At high temperatures, such as for position 4A, there is a continuous transition to the high current mode because neutralizing ions exist in great abundance.

The initial currents have not been studied because the lack of guard rings makes the interpretation difficult.

REFERENCES

1. K. T. Compton and C. Eckart, Phys. Rev. 25, 139 (1925)
2. M. J. Druyvesteyn, Z. Physik 64, 782 (1930)
3. E. O. Johnson, R. C. A. Review 16, 498 (1955)
4. L. Malter, E. O. Johnson and W. M. Webster, R. C. A. Review 12, 415 (1951)
5. W. M. Webster, E. O. Johnson and L. Malter, R. C. A. Review 13, 163 (1952)
6. E. O. Johnson and W. M. Webster, R. C. A. Review 16, 82 (1955)
7. N. R. Daly and K. G. Emeleus, Brit. J. Appl. Phys. 6, 370 (1955)
8. R. B. Cairns and G. C. McCullagh, J. Elect. and Control, 6, 65 (1959)
9. A. E. Pengelly and D. A. Wright, Brit. J. Appl. Phys. 5, 391 (1954)
10. O. S. Duffendack, Phys. Rev. 20, 665 (1922)
11. J. M. Houston and M. D. Gibbons, "Cesium Ion Neutralization of Thermionic Converters," Report of 21st Conference on Physical Electronics, M. I. T. 1961, p. 106
12. J. M. Houston, "Thermionic Emission of Refractory Metals in Cesium Vapor," Proceedings of the Round Table Discussion, June 1 and 2, 1961, Power Information Center Report PIC-ELE-TI 3/3, University of Pennsylvania, Philadelphia, Appendix F-1
13. R. L. Aamodt, L. J. Brown and B. D. Nichols, "Thermionic Emission from Molybdenum with Adsorbed Cesium and Cesium Fluoride," Proceedings of the Third Government-Industry Thermionic Roundtable Discussions, Vol. I, December 6 and 7, 1961, Power Information Center Report PIC-ELE-TI 209/1, University of Pennsylvania, Philadelphia, Section 10
14. W. B. Nottingham, "Analysis of Typical Voltage-Current Curves,"

PIC-ELE-TI 209/1, ibid. Section 1

15. W. B. Nottingham, "The Thermionic Energy Converter," Technical Report 373, M. I. T. Research Laboratory of Electronics (1960), p. 11

16. See references of Section VI

17. C. Warner III, "Analysis of the Plasma Mode in the Cesium Thermionic Converter," First Summary Report of Basic Research in Thermionic Energy Conversion Processes, Atomics International Report AI-6799, Section C2 (1961)

18. R. Vernon, "Plasma Mode in a Thermionic Diode with Detailed Energy Balance," AI-6799, ibid. Section C3

19. S. S. Kitrilakis, M. E. Meeker and N. S. Rasor, Annual Technical Summary Report for the Thermionic Emitter Materials Research Program, Thermo Electron Engineering Corp., Report TEE 4015-3, Waltham, Massachusetts, June 1962

20. J. E. Gingrich, C. Warner and C. C. Weeks, "Experimental Measurement and Interpretation of Volt-Ampere Curves," Symposium on Thermionic Power Conversion, Colorado Springs, May 1962

21. E. Blue, J. H. Ingold and W. J. Ozeroff, "Diffusion of Electrons and Ions in a Neutral Gas," Symposium on Thermionic Power Conversion, Colorado Springs, May 1962

22. E. N. Carabateas, J. Appl. Phys. 33, 1445 (1962)

VIII. VAPORIZATION AND DEPOSITION AT CESIUM COVERED SURFACES

L. K. Hansen

INTRODUCTION

The effect of adsorbed cesium on electrode work functions has been a subject of study for many years. In recent years interest has increased due to the application of these effects to thermionic energy conversion. The use of adsorbed cesium for controlling emitter and collector work functions and consequently for increasing converter efficiencies is well understood. The effect of adsorbed cesium on the processes involved in converter lifetime, however, has not received such extensive study. The purpose of this investigation was to examine the effect of adsorbed cesium on the material transport processes in thermionic converters, in particular, the vaporization and deposition processes. In order to accomplish this, the experiment was performed in a cesium atmosphere with cesium pressures low enough so that the experimental results were not affected by scattering and diffusion in the space between the vaporizing and collecting surfaces.

At one time it was thought that adsorbed cesium would lower the free energy of vaporization and therefore increase the rate of vaporization of a substrate material.[1] On the other hand, Richardson et al.[2] have assumed that adsorbed cesium would reduce the rate of vaporization, producing a $(1-\Theta)$ dependence where Θ is the percentage cesium coverage of the surface. Unfortunately the results of their experiment were not sensitive to this effect and therefore the hypothesis could not be tested. Some measurements were made, however, of the diffusion effect in the cesium gas, an effect purposely eliminated in the present study. A $(1-\Theta)$ dependence has

previously been postulated for adsorbed oxygen on molybdenum[3] in order to explain observed effects of an electric field on vaporization rates.[4,5]

KINETICS OF VAPORIZATION AND DEPOSITION[6,7]

The process of vaporization is closely related to the process of crystal growth. The present concept of both processes began with Volmer's[8] suggestion that these phase changes proceed stepwise through an intermediate, self adsorption state. This hypothesis was suggested by the earlier work of Kossel[9] and Stranski[10] who showed that there is a variation of binding energies among the surface atoms of a crystalline solid. Also, the existence of the self adsorbed layer has been indicated by the experiments of Langmuir,[11] Knudsen,[12] and Volmer.[13] Kossel's idealized model of a low-index plane is shown in Figure 1. In this figure atoms in the self adsorbed state are marked C.

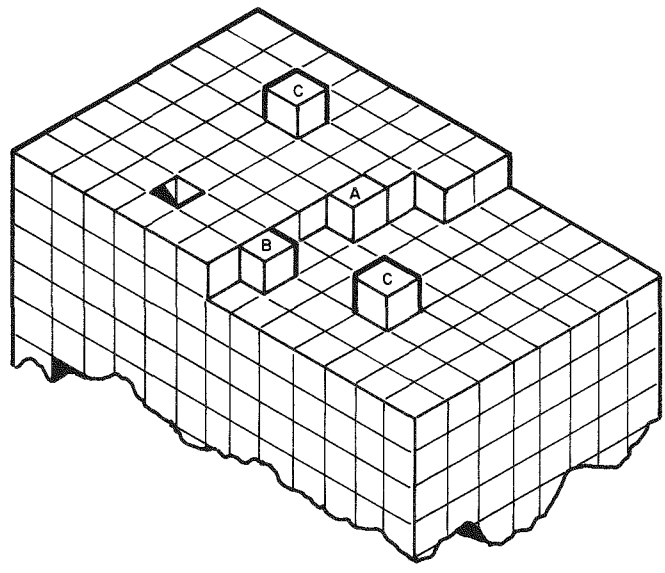

Figure 1. Kossel's Idealized Model of a Low-Index Plane

The vaporization process is thought to consist first of dissociation from monatomic ledges (positions A to B and then to C). Supposedly, the self adsorbed atoms then diffuse in areas between ledges and finally leave the surface. This model for the kinetics of the phase change has since become highly developed by Burton, Cabrera and Frank[14,15] and others for the process of crystal growth. Knacke, Stranski and Wolff[16] have developed the model for the process of vaporization. More recently Hirth and Pound[17,18] have also advanced the model for the vaporization process.

Adsorbed cesium can be expected to affect the dissociation from ledges and the surface diffusion of the self adsorbed atoms, but an analysis of the effect of adsorbed cesium on these vaporization processes has not yet been made. However, in the theory of Hirth and Pound,[17] even though the effects of adsorbed impurities are not considered, one may consider the effect that adsorbed cesium will have on the parameters of the theory and thereby obtain an insight into the effect of cesium on the vaporization rate. Most of the parameters of their theory which could be affected by adsorbed cesium occur in a common factor $\mathcal{Q}$,

$$\mathcal{Q} = \left(\frac{D_s}{\nu} \exp \frac{\Delta F}{kT}\right)^{1/2}$$

where D_s is the surface coefficient, ν is the vibrational frequency of atoms at the surface and ΔF is the free energy change in the desorption process. Under the basic assumptions of their theory, and under the assumption that ledges reach equilibrium velocity in a distance small compared to crystal dimensions, the rate of vaporization is independent of $\mathcal{Q}$, and therefore independent of the effect of adsorbed cesium through the above parameters. This conclusion must not be considered a final answer,

however, for some of the assumptions of Hirth and Pound will have to be reconsidered if adsorbed impurities are involved.

The effect of adsorbed cesium on the deposition of atomic beams has also not been reported. Information is available, however, concerning the effect of surface oxides and some adsorbed gases other than cesium.[19,20] Rapp, Hirth and Pound[21] suggest four ways in which the condensation coefficient may be affected by adsorbed impurities: 1) adsorbed impurities may diminish thermal accommodation of incident atoms so that these atoms are reflected instead of adsorbed; 2) because of reduced chemical activity of the surface, the desorption energy will be reduced and therefore the mean time of adsorption will be less. This in turn decreases the probability that the adsorbed atom can diffuse to a position where it can be incorporated into the crystal lattice; 3) impurities will preferentially adsorb at ledges. This may hinder the incorporation of self adsorbed atoms into lattice sites and may make deposition dependent on surface nuclei formation; 4) impurities will affect the energetics of surface nuclei formation. This in turn will change the point of critical supersaturation.

Although the above effects seem certain to modify the condensation coefficient Rapp, Hirth and Pound[21] found that a background gas pressure of 10^{-4} mm Hg did not affect the condensation coefficient of cadmium. However, they used a very high supersaturation and a very low substrate temperature. As an example of the effect of adsorbed impurities on deposition, one may cite the work of Sears[22] who has analyzed the effect of adsorbed films on crystal growth kinetics and has applied this analysis to chemisorbed oxygen on potassium. Potassium was expected to grow by a screw dislocation and therefore was not expected to display a critical supersaturation. Hock and Neumann[23] however found a critical supersaturation.

Sears was able to explain this unexpected result in terms of impurity poisoning of the dislocation ledge. Presumably rotation of the dislocation could proceed only when supersaturation was great enought to allow nucleation of new ledges at the poisoned ledges. These results are true in general;[19] that is, only on clean, chemically active surfaces with low disregistry between lattice constants can one expect to have a condensation coefficient close to unity at elevated temperatures and low incident fluxes. On the other hand, surfaces with oxide layers and/or adsorbed gases display a critical supersaturation and therefore have a condensation coefficient of unity only at very low substrate temperatures and high incident fluxes.

EXPERIMENT

In order that the effect of adsorbed cesium on vaporization and deposition could be studied the experiment was performed in a cesium atmosphere. Preventing this atmosphere from introducing diffusion effects into the results of the experiment placed severe requirements on the experimental approach. Cesium pressure was limited so that the vaporizing surface (ribbon filament) and the collecting surface were within a mean free path of each other. Because of this low pressure the ribbon filament was limited in temperature in order to retain a significant cesium coverage. For the same reason filament materials with low work functions were excluded from the study. It was also necessary that the ribbon filament be hot enough and its vapor pressure high enough so the vaporized flux would be great enough to do the experiment within a reasonable time. In addition, the material for vaporization and an operating temperature had to be chosen so that cesium would neither react nor amalgamate with the filament. The material chosen for the experiment was nickel. Because of

nickel's relatively high melting point (1453°C), high work function (4.6 ev), and relatively high vapor pressure (about 10^{-6} mm Hg at 1100°C) as well as compatibility with cesium, it seemed to be the best available material for the experiment. The temperature for operation was chosen as 1025°C where the vaporization rate is about 6 μg/min for the area of the collector. At this temperature the filament would become a third to a half covered before diffusion and back-scatter from the cesium became a problem.

The filament and collector separation was chosen to be .05 inch. To allow accurate positioning even with thermal expansion of the filament, the nickel was applied to a tungsten ribbon by chemical vapor deposition and spring loaded in the apparatus as shown in Figure 2. The filament was mounted in a stainless steel chamber sealed with copper shear gaskets. Collector plates were mounted on a wheel which could be rotated by a magnetic coupling through the chamber walls. An ion pump was mounted to the chamber for final evacuation; initial evacuation was through a copper pinch-off tabulation. Cesium ampules were inserted into another pinch-off tubulation and cesium pressure was controlled by temperature control of a stainless steel extension from the chamber. Filament temperatures were read through a sapphire window. The amount of material deposited on the collector plates was determined by colorimetric techniques.

For a first series of runs the chamber was baked at about 10^{-6} mm Hg at 350°C. The cesium ampule was then broken and the temperature of the chamber lowered to 250°C for the experiment. Later runs involved baking in hydrogen at atmospheric pressure. A residual hydrogen pressure of about 10^{-3} mm Hg was left in the chamber for these runs. It is expected that cesium provided some gettering action during the experiment.

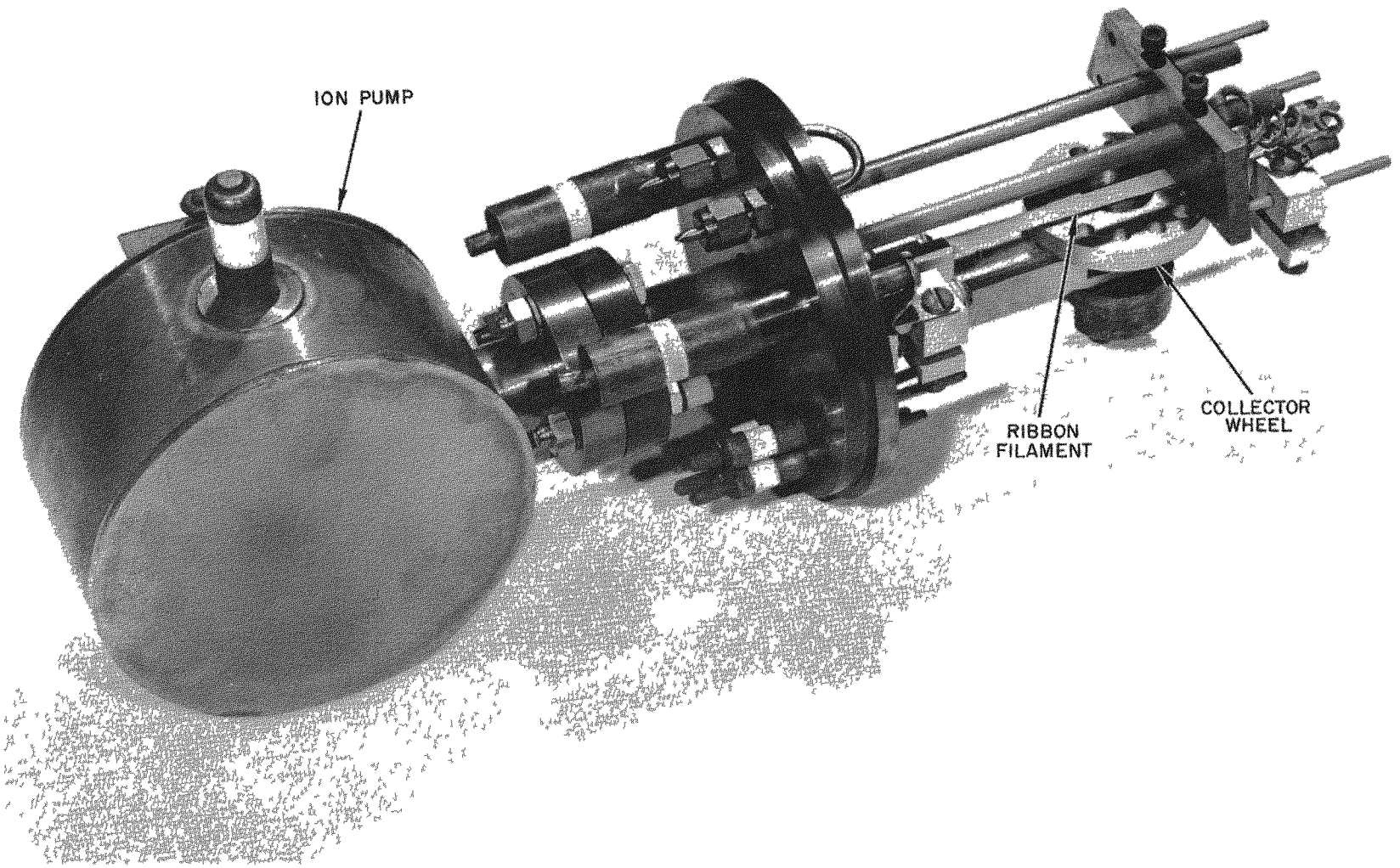

Figure 2. Vacuum Chamber Cover Assembly

Collector plates of sapphire, platinum, carbon, stainless steel and copper were used. In every case, using the various collector plates and the cesium or the cesium and hydrogen atmosphere, the condensation coefficients were less than 1.0-2.0 x 10^{-2} and independent of cesium pressure (reservoir temperature was varied between 20°C and 200°C). In these runs the wheel temperature was 300-400°C. The temperature at the surfaces of the collector plates was not determined. A series of copper collectors were also used which were in the shape of hollow cavities. These gave the same low value for the condensation coefficient. The exact value of the condensation coefficient was not determined in any of the above cases since the amount of material measured was approximately equal to the resolution of the colorimetric analysis, 1 μg. Two measurements were made, however, which estimate the actual magnitude of the condensation coefficient. One run, with the hydrogen gas background and a filament temperature of 1175°C, deposited 5 μg on a copper collector. This indicates a condensation coefficient of about 1.3 x 10^{-3}.

In order that the application of these results to materials and conditions found in thermionic converters could be tested, a converter was examined to determine the emitter material transported under normal operating conditions. This device had operated for 200 hours with a molybdenum emitter at 1800°C, a cesium reservoir temperature of 350 to 400°C, a spacing of 10 mil and a collector of stainless steel at 650 to 750°C. The amount of emitter material deposited was 30 μg. If back-scatter and diffusion effects due to the cesium atmosphere and change in the vaporization rate due to adsorbed cesium on the emitter are neglected, this indicates a condensation coefficient of 0.5 x 10^{-3}.

CONCLUSION

The material transport measurements obtained here are the composite results of effects occurring at both the vaporizing and collecting surfaces. Since no dependence on cesium pressure was observed with the nickel measurements, one may assume that as far as material transport in thermionic converters is concerned the effect of adsorbed cesium upon the vaporization rate of the emitter is not significant compared to the effect of the low condensation coefficient at the collector. A low condensation coefficient can be expected when the depositing surface has a high temperature and when oxides and/or adsorbed impurities are present. Because of the dominating effect of the low condensation coefficient no information could be obtained concerning the effect of adsorbed cesium on vaporization rates. The correlation between the results with nickel and with molybdenum in an operating converter seem to indicate that not only is the effect of adsorbed cesium on the vaporization rate not a controlling factor for material transport, but also, back-scatter and diffusion processes in the cesium atmosphere are not of primary importance.

The transport of emitter material and therefore the lifetime of a thermionic converter will be affected primarily by the low condensation coefficient for the emitter material at the collector surface. Because of the low value of this coefficient an equilibrium partial pressure of the vaporized emitter material will build up in a converter interelectrode space and will greatly reduce the net vaporization of the emitter material.

REFERENCES

1. N.S. Rasor, PIC-ELE-TI 3/3 Appendix B June 1961
2. L.S. Richardson, et al., Symposium on Thermionic Power Conversion, Colorado Springs, May 1962
3. W.P. Reid, Phys. Rev. 63, 359 (1943)
4. G.B. Estabrook, Phys. Rev. 63, 352 (1943)
5. N.A. Garbatyi & G.N. Shuppe, Soviet Physics, Technical Physics, 3, 587 (1958)
6. O. Knacke & I.N. Stranski, "The Mechanism of Evaporation," Progress in Metal Physics (Vol. 6, Pergamon Press, 1956) p 181
7. A. Van Hook, Crystallization (Reinhold Publ. Corp., 1961)
8. M. Volmer, Kinetic der Phasenbildung, Dresden & Leipzig, 1939
9. W. Kossel, Naturwissenschaften 18, 901 (1930)
   W. Kossel, Am. Phys. 33, 651 (1938)
10. I.N. Stranski, Z. Phys. Chem. 136, 259 (1928); (B)11, 421 (1931)
    I.N. Stranski & R. Kaischew, Z. Krist. 78, 373 (1931)
11. I. Langmuir, Phys. Rev. 8, 149 (1916)
12. M. Knudsen, Am. Phys. (Leipzig) 28, 75 (1908); 35, 389 (1911)
13. M. Volmer & I. Estermann, Z. Phys. 7, 13 (1921)
14. Burton, Cabrera & Frank, Trans. Roy. Soc. 243A 299 (1951)
15. F.C. Frank, Advances in Physics 1, 91 (1952)
16. Knache, Stranski & Wolff, Z. Elektrochem 56, 476 (1952)
    Z. Physik Chem. 198, 157 (1951)
17. J.P. Hirth & G.M. Pound, J. Chem. Physics 26, 1216 (1957)
18. J.P. Hirth, Acta Met. 5, 649 (1957)
19. S. Wexler, Rev. Mod. Phys. 30, 402 (1958)

20. F.S. Baker & G.O. Brink, UCRL-6722

21. R.A. Rapp, J.P. Hirth & G.M. Pound, J. Chem. Phys. 34, 184 (1961)

22. G.W. Sears, J. Chem. Phys. 25, 154 (1956)

23. F. Hock & K. Neumann, Zt. Phys. Chem. 2, 241 (1954)

IX. CESIUM PURIFICATION

R. L. McKisson

INTRODUCTION

Since it has been shown experimentally that impurities or additives to cesium vapor have a profound effect on converter performance, a program was instituted to examine the purity of the commercially available cesium. The goal of the program was to obtain cesium metal of sufficiently high purity so that the effects of impurities on converter operation could be properly identified. At the outset, the cesium analyses quoted by the commercial suppliers indicated substantial amounts of impurities in the metal. Whether the metal actually was so impure, or whether the early analyses were so uncertain, still remains an unknown. In any event, a program for obtaining purer cesium was initiated.

CESIUM ANALYSIS

The first step in this program was to contact the commercial producers of cesium and to enlist their aid in improving their products. Immediate interest was evidenced, particularly by the Dow Chemical Company and American Potash and Chemical Corporation. Both companies provided preparative and analytical procedures, and were cooperative in providing analyses of their products.

It was intended that first the purest source of cesium metal would be determined and them, if required, an attempt would be made to purify the metal further at Atomics International. To this end, inquiries for carrying out analyses of cesium metal (or of a cesium halide to be prepared by AI from cesium metal) were made at several analytical laboratories. It was found, however, that the cost of the requested analyses was quite high and it was decided to carry out the analyses at AI. There were, however, no

pure cesium salts available commercially from which analytical standards could be made. Here, again, assistance was obtained from American Potash and Chemical Corporation in the form of about 25 grams of very highly purified cesium chloride prepared by their research laboratory staff. This material proved to be excellent, and was used as a standard in the AI analyses. The analyses provided by the suppliers of recently purchased cesium indicated that significant improvements in quality were being made.

In Table I the results are shown of the analyses of cesium metal made by the supplier. These analyses show the continuing improvement in the quality of cesium produced by Dow Chemical Company. The Dow people have been working on cesium purity for several years and their product is now quite pure.

The AI analytical results for four cesium samples are shown in Table II. The results for cesium from Dow Chemical Company agree with the results shown in Table I. Cesium from Mine Safety Appliance also shows a high purity, and the analysis of the cesium from American Potash and Chemical is quite good except for a high Rb content.

TABLE I - TYPICAL CESIUM METAL ANALYSES

Element	Supplier				
	Dow 9-60	Dow 6-61	Kawecki 6-61	Am. Potash & Chemical	Dow 9-6-61*
Cs	99.9+%	99.9+%	99.9%	99.11%	
Al	0.0006	0.0005			0.0003
B	<0.0080	<0.0016			<0.0016
Ba	<0.0008				<0.0008
Ca	0.0033	0.0010	0.01		0.0030
Cr	<0.0002				0.0005
Cu	0.0002	<0.0002			0.0011
Fe	0.0021	0.0006			0.0030
K	0.0018	<0.0016	0.01	0.03	0.0035
Li	<0.0016		ND	0.00	<0.0016
Mg	0.0003				0.0003
Mn	<0.0002				0.0002
Na	0.0051	<0.0016	0.01	0.02	0.0073
Ni	0.0002				0.0003
O	0.0080	0.0036			
Pb	<0.0008	<0.0002			<0.0002
Rb	0.029	0.016	0.01	0.39	0.0047
Si	0.0042				0.0008
SiO2			0.005		
Sn	<0.0008				
Sr	<0.0002				<0.0002
Fe+Al			0.001		

*Certified Analysis of Cesium purchased
P.O. N 151TX - 50906 H

TABLE II - ATOMICS INTERNATIONAL CESIUM ANALYSES

July, 1962

Element	American Potash & Chemical	Mine Safety Appliance	Dow	(Kawecki) Penn Rare Metals
Ag	<0.0001	<0.0001	<0.0001	<0.0001
Al	<0.0005	<0.0005	<0.0005	0.0020
B*	0.0010	0.0010	0.0090	0.0150
Ba	<0.0001	<0.0001	<0.0001	<0.0001
Be	<0.0001	<0.0001	<0.0001	<0.0001
Ca	<0.0005	<0.0005	0.0005	0.0035
Cd	<0.0001	0.0004	<0.0001	<0.0001
Cr	<0.0001	<0.0001	<0.0001	<0.0001
Cu	<0.0005	<0.0005	<0.0005	<0.0005
Fe	<0.0005	<0.0005	<0.0005	0.0020
Mg	<0.0005	0.0010	0.0007	<0.0005
Mn	<0.0001	<0.0001	<0.0001	<0.0001
Ni	<0.0010	<0.0010	<0.0010	<0.0010
Pb	<0.0001	<0.0001	<0.0001	<0.0001
Si*	0.0070	0.0050	0.0140	0.0280
Sn	<0.0001	<0.0001	<0.0001	<0.0001
Ti	<0.0005	<0.0005	<0.0005	<0.0005
Sr	<0.0001	<0.0001	<0.0001	<0.0001
Na	0.0020	0.0020	<0.0010	0.0070
Rb	0.0700	<0.0100	<0.0100	0.0300
K	0.0040	<0.0040	<0.0040	0.0130
Li	ND	ND	ND	ND

*High Band Si values are thought to be due to spurious pickup from glassware.

NOMENCLATURE

$A_{i,a}$	a Langmuir "entropy" factor, defined on page 15 , Section III
a	differential ionization constant discussed in J.D. Cobine, Gaseous Conductors (1st ed., New York, McGraw-Hill Publishing Co., 1941), pp 79-80
$B_{i,a}$	a Langmuir "entropy" factor, defined on page 15 , Section III
b	exclusion area, πr^{*2}
C	constant defined by Equation 52, Section III
D_e	electron diffusion coefficient
D_p	ion diffusion coefficient
D_s	self adsorbed atom, surface diffusion coefficient
E	energy difference between adatom and adion (Equation 29, Section III)
E_o	energy difference between adatom and adion at zero coverage
E_s	average energy of adions due to dipole-dipole interactions (Equation 20 in Section III)
$\mathcal{E}$	electric intensity
e	electronic charge
F	defined by Equation 34, Section VII
F'	defined by Equation 37, Section VII
ΔF	free energy of vaporization
f	ion penetration factor (Equation 26, Section III)
f	fractional patch area, Section VII
f_a	normal vibrational frequency of adatoms
f_i	normal vibrational frequency of adions
$G(\eta)$	defined by Equation 15, Section V

$G'(\eta)$	first derivation of $G(\eta)$
g_a	atom pair correlation function
g_{ai}	atom-ion pair correlation function
$g_i, g_i(\vec{x}_1, \vec{x}_2)$	ion pair correlation function
H	Hamiltonian
H_a	atom-atom interaction energy
H_{ai}	atom-ion interaction energy
$H_i, H_i(\vec{x}_1, \vec{x}_2)$	ion-ion interaction energy
H_s	Hamiltonian for adsorbed particles
h	Debye length or sheath thickness
h_c	Debye length at the collector
I	diode current
I	ionization energy
i	diode current
$i_-(\xi=0)$	emitted electron current
J_s	saturation (Richardson) current density
J_+	emitted ion current density
J_-	emitted electron current density
k	Boltzmann constant
L	diode interelectrode spacing
M	dipole moment of ion-image pair
M_o	Dipole moment of ion-image pair at zero coverage
m, m_-	electronic mass
M, m_+	mass of cesium ion
N_a	total number of atoms in the gas
N_e	total number of electrons in the gas
N_i	total number of ions in the gas

N_{sa}	total number of adatoms on the surface
N_{si}, N'_{si}	total number of adions on the surface
$n, n(x)$	density of ions or electrons in the plasma
n_e	density of electrons in the plasma
n_{eE}, n_{eC}	density of electrons in the plasma and near the emitter/collector
n_p	density of ions in the plasma
n_+	density of ions emitted at the emitter
n_{+o}	twice the emitted ion density
n_-	density of electrons emitted at the emitter
n_{-o}	twice the emitted electron density
P, p	pressure
p_i	momentum
Q	canonical ensemble partition function in Section III
Q	vaporization coefficient defined on page 112, Section VIII
q_a	classical partition function for a one-dimensional harmonic oscillator for the adatoms
q_i	classical partition function for a one-dimensional harmonic oscillator for the adions
R	current ratio coefficient defined on page 91, Section III
r_{ij}	distance between particles i and j
r^*	hard core distance of adatoms and adions
$\mathcal{S}$	surface area
$\mathcal{S}_f$	free area defined by Equation 19, Section III
T	temperature
$T_E, T(E)$	emitter temperature
$T_R, T(R)$	cesium reservoir temperature
$T(C)$	collector temperature

$u(ij)$	hard core potential
V	voltage
V	volume
V_i	ionization potential
V_L	voltage across diode
v_e	electron velocity
v_p	ion velocity
x, x_i	space coordinate
x_m	distance from the emitter at which the field first vanishes
$\bar{\alpha}$	defined by Equation 42, Section III
α	ion polarizability
β	in Section IV, density ratio at the emitter surface of electrons to ions coming from the emitter surface
β	in Sections V and VII, density ratio at the emitter surface of ions to electrons coming from the emitter surface
Γ_r	random electron flux in the plasma near the emitter
Γ_e, Γ_p	net electron flux/ion flux
$\Gamma^{(e,p)}_{diff}$	diffusion current defined on page 96, Section VII
$\Gamma^{(e,p)}_{cond}$	conduction current defined on page 96, Section VII
γ	defined on page 91, Section VII
ϵ_o	permitivity of free space
η	dimensionless potential defined on page 31, Section IV
η_L	dimensionless potential across the diode
η_A	dimensionless potential difference between the potential minimum and the collector
η_B	dimensionless potential difference between the potential minimum and the collector

η_m	dimensionless potential at which the electric field first vanishes
η_{min}	dimensionless potential of the collector
η_E	dimensionless potential of the emitter sheath
η_C	dimensionless potential of the collector sheath
η_{max}	dimensionless potential where the electric field vanishes a second time
$\Delta\eta$	dimensionless plasma potential drop
η_m^*	defined by Equation 20, Section IV
$\bar{\eta}_m$	negative of the dimensionless collector potential
η_m'	defined by Equation 21 in Section IV
η_{max}'	defined by Equation 22 in Section IV
θ	percent cesium coverage of a surface
Λ	thermal deBroglie wave length defined on page 12, Section III
λ_e	electron mean free path in cesium
λ_p	cesium ion mean free path in cesium
μ	cesium arrival rate
μ_e	electron chemical potential in a gas
μ_{em}	electron chemical potential in a metal
μ_a	atom chemical potential in a gas
μ_i	ion chemical potential in a gas
μ_{sa}	adatom chemical potential
μ_{si}	adion chemical potential
ν	frequency of normal surface vibration of self adsorbed atoms
ν_a	atom departure rate
ν_e	electron departure rate
ν_p	ion departure rate

ξ	dimensionless distance (proportional to the square root of the diode current and therefore also a current coordinate) defined by Equation 2 of Section IV and Equation 1 of Section V
ξ_L	dimensionless distance corresponding to diode spacing L (proportional to the square root of the diode current and therefore also a current coordinate)
ξ_m	dimensionless distance corresponding to η_m
σ_1	monolayer density for C_s-[W]
ϕ	electron work function
φ	energy defined by Equation 18, Section III
$\bar{\varphi}$	energy defined by Equation 33, Section III
ϕ_a^*	energy required to convert adsorbed ion to free atom
ϕ_{ao}	energy of cesium evaporation
ϕ_C	collector work function
ϕ_E	emitter work function
ϕ_{io}	energy of ionic evaporation at zero coverage
$\bar{\nu}$	defined on page 22, Section III
erf(x)	error function
erfc(x)	complementary error function [1-erf(x)]

DISTRIBUTION LIST

No. of Copies	Recipient
4	Office of Naval Research Power Branch (Code 429) Department of the Navy Washington 25, D.C.
1	Pasadena ONR Area Branch Office Pasadena, California
6	U.S. Naval Research Laboratory Technical Information Division Washington 25, D.C.
1	U.S. Naval Research Laboratory Washington 25, D.C.
	Attn: Code 6430
2	Commanding Officer Office of Naval Research Branch Office Box 39 Navy #100 Fleet Post Office New York, New York
1	Office of Technical Services Department of Commerce Washington 25, D.C.
10	Armed Services Technical Information Agency Arlington Hall Station Arlington 12, Virginia
1	National Aeronautics & Space Administration 1520 H. Street, N.W. Washington 25, D.C.
	Attn: James J. Lynch
	National Aeronautics & Space Administration Lewis Research Center 2100 Brookpark Road Cleveland 35, Ohio
1	Attn: Frank Rom
1	Roland Breitwieser
1	Bernard Lubarsky

No. of Copies	Recipient
1	Chief of Naval Operations (OP-07G) Department of the Navy Washington 25, D.C.
1	Commandant, U.S. Marine Corps Code CSY-3 Headquarters, Marine Corps Washington 25, D.C.
	Chief, Bureau of Ships Department of the Navy Washington 25, D.C.
1	Attn: Code 342B
1	Code 1500, LCDR J.H. Weber
1	Code 359, LCDR F. Anders
	Division of Reactor Development U.S. Atomic Energy Commission Washington 25, D.C.
1	Attn: Auxiliary Power Branch
1	Direct Conversion Branch
1	Army Reaction & Water Systems Branch
1	Aeronautical Systems Division ASRMFP-2 Wright Patterson Air Force Base Ohio
1	Air Force Cambridge Research Center (CRZAP) L.G. Hanscom Field Bedford, Massachusetts
1	Power Information Center University of Pennsylvania Moore School Building 200 South 33rd Street Philadelphia 4, Pennsylvania

No. of Copies	Recipient
10	Director of Special Projects (SP-001) Department of the Navy Washington 25, D.C.
1	Los Alamos Scientific Laboratory P.O. Box 1663 Los Alamos, New Mexico Attn: Dr. George M. Grover
1	Argonne National Laboratory 9700 South Cass Avenue Argonne, Illinois Attn: Aaron J. Ulrich
2	Director, Advanced Research Projects Agency The Pentagon Washington 25, D.C. Attn: Dr. John Huth
1	U.S. Army Signal R&D Laboratory Fort Monmouth, New Jersen Attn: Dr. Emil Kittl
1	Mr. A.F. Underwood, Manager General Motors Research Labs. 12 Mile and Mound Road Warren, Michigan Attn: Dr. F. Jamerson
1	General Atomic P.O. Box 608 San Diego 12, California Attn: Dr. R.W. Pidd
1	Republic Aviation Framingdale Long Island, New York Attn: A. Schock
1	Allied Research Associates, Inc. 43 Leon Street Boston 15, Massachusetts Attn: Dr. P. Goodman
1	Ford Instrument Company 3110 Thomas Avenue Long Island City, New York Attn: T. Jarvis
1	Armour Research Foundation 10 W. 35th Street Chicago 16, Illinois Attn: Dr. D.W. Levinson
1	Jet Propulsion Laboratory California Institute of Technoloty 4800 Oak Grove Drive Pasadena, California
1	RCA Laboratories David Sarnoff Research Center Princeton, New Jersey Attn: Dr. P. Rappaport
1	The Martin Corporation Baltimore 3, Maryland Attn: Dr. M. Talatt
1	Thermo Electron Engineering Corporation 85 First Avenue Waltham 54, Massachusetts Attn: Dr. G. Hatsopoulos
1	Hughes Research Laboratories 3011 Malibu Canyon Road Malibu, California Attn: Dr. R.C. Knechtli
1	Thomson Ramo Wooldridge, Inc. 7209 Platt Avenue Cleveland 4, Ohio Attn: Wm. J. Leovic
1	General Electric Research Laboratory Schenectady, New York Attn: Dr. V.C. Wilson

No. of Copies	Recipient
1	Westinghouse Electric Company Research Laboratories Beulak Road, Churchilboro Pittsburgh, Pennsylvania Attn: Dr. Max Garbuny
1	Massachusetts Insitute of Technology 77 Massachusetts Avenue Cambridge, Massachusetts Attn: D. White
1	The Marquardt Corporation ASTRO Division 16555 Saticoy Street Van Nuys, California Attn: A.N. Thomas
1	Texas Instruments, Inc. P.O. Box 5474 Dallas 22, Texas Attn: Dr. R.A. Chapman
1	University of Denver Colorado Seminary Denver Research Institute Denver 10, Colorado Attn: Dr. C.B. Magee
1	Radio Corp. of America Electron Tube Division Lancaster, Pennsylvania Attn: F.G. Block
1	Electro-Optical Systems, Inc. 125 N. Kinedo Avenue Pasadena, California Attn: A. Jensen
1	General Electric Company P.O. Box 546 Atomic Product Division Vallecitos Laboratory Pleasenton, California Attn: Robert Scott
1	General Electric Company Power Tube Division 1 River Road Schenectady 5, New York Attn: Mr. Wm. Miller